Mussel-Inspired Metallo-Supramolecular Polymeric Hydrogels

Mostafa Rammal

A thesis submitted to McGill University

in partial fulfillment of the requirements of the degree of

Doctor of Philosophy

Department of Chemistry, McGill University

Montreal, Quebec, Canada

December 2023

Abstract

Natural biopolymeric systems serve as a significant source of inspiration for scientists and engineers seeking to create innovative high-performance materials for various applications. For example, mussels can adhere strongly to diverse types of surfaces via the byssus, a collection of tough and flexible collagenous fibers. Previous studies highlighted the role of metal coordination in the reinforcement of their protein-based byssal threads. This reinforcement is pivotal for mussels to securely attach to rocky seashores and withstand the challenges of high intertidal zones owing to the exceptional toughness and self-healing capabilities of these fibers. Taking inspiration from this system, metal coordination-based crosslinks have garnered significant attention due to their remarkable binding affinities and rapid formation kinetics. These studies leverage diverse chemistries, such as histidine-metal coordination, DOPA-metal coordination, alongside material design principles used by mussels to create materials with desirable properties. Adopting these crosslinks has been instrumental in conferring advantageous properties to synthetic materials including mechanical toughness, stimuli responsiveness, and self-healing. While these chemical approaches have been applied to various polymeric systems, there exists a significant untapped potential for their utilization in advanced materials applications (e.g., injectable tissue scaffolds, optical materials, etc.…) as explored in this thesis. Furthermore, most synthetic mussel-inspired materials take the DOPA or histidine metal-binding moiety out of context of the native protein sequence; however, recent studies highlight the functional importance of the other amino acids (Lysine-cysteine) in the native sequences. Thus, a better fundamental understanding of metal coordination of mussel protein sequences holds the potential to advance the development of superior mussel-inspired materials.

This thesis is composed of three studies that seek to adapt and utilize design principles found in the byssus to create novel synthetic materials with complex hierarchical structure and advanced material characteristics, such as self-healing, stimuli responsiveness, and injectability. In the first study, we designed an injectable granular hydrogel composed of interconnected microgels. Microgels were annealed using histidine-zinc coordination, taking inspiration from the protein sequence employed by marine mussels in the assembly of tough and self-healing collagenous fibers from liquid crystal precursors. This injectable scaffold demonstrated excellent cell viability, cell adhesion, and cell spreading, rendering it highly promising for tissue repair applications. In the second study, drawing inspiration from the adhesive chemistry of the byssus, we took advantage of the strong yet reversible vanadium-catechol coordination to create pliable and self-healing thermochromic films. The interactions between VO_2 nanoparticles and catechol-modified polymers serve as the cornerstone, endowing the films with both flexibility and self-healing capability when subjected to damage while simultaneously preserving the thermochromic response of the nanoparticles. In the third study, our aim was to elucidate the factors contributing to the superior performance of the native DOPA-rich byssus proteins in comparison to synthetic DOPA-functionalized polymers, in which the DOPA catechol moiety is utilized outside the context of the native protein sequence. We conducted a comparative analysis of the metal-binding capabilities between catechol-functionalized polymers and those functionalized with short peptides with sequences directly derived from the DOPA-rich mussel foot protein (mfp-1) (i.e., catechols are in their native context). This study highlighted the role of the native sequence in modulating metal-binding (e.g., metal affinity, optimal pH of metal binding) and gave an insight into how to design better mussel-inspired polymers.

Résumé

Les systèmes biopolymériques naturels constituent une source d'inspiration significative pour les scientifiques et les ingénieurs cherchant à créer des matériaux innovants à haute performance pour diverses applications. Par exemple, les moules peuvent fortement adhérer à différents types de surfaces grâce au byssus, un ensemble de fibres collagènes robustes et flexibles. Des études antérieures ont souligné le rôle de la coordination métallique pour renforcer leurs fils de byssus à base de protéines. Ce renforcement est essentiel pour que les moules s'attachent solidement aux rivages rocheux et résistent aux défis des zones intertidales élevées, en raison de la robustesse exceptionnelle et des capacités d'auto-réparation de ces fibres. Inspirés par ce système, les liens croisés basés sur la coordination métallique ont suscité une attention considérable en raison de leurs affinités de liaison remarquables et de leur cinétique de formation rapide. Ces études exploitent diverses chimies, telles que la coordination histidine-métal, DOPA-métal, ainsi que les principes de conception de matériaux utilisés par les moules pour créer des matériaux aux propriétés souhaitables. L'adoption de ces liens croisés a été essentielle pour conférer des propriétés avantageuses aux matériaux synthétiques, y compris la robustesse mécanique, la réactivité aux stimuli et l'auto-réparation. Bien que ces approches chimiques aient été appliquées à divers systèmes polymères, il existe un potentiel considérable non exploité pour leur utilisation dans des applications de matériaux avancés (par exemple, échafaudages de tissus injectables, matériaux optiques, etc.) comme exploré dans cette thèse. En outre, la plupart des matériaux synthétiques inspirés des moules prennent le motif de liaison métallique DOPA ou histidine hors du contexte de la séquence protéique native; cependant, des études récentes soulignent l'importance fonctionnelle des autres acides aminés (lysine-cystéine)

dans la séquence. Ainsi, une meilleure compréhension fondamentale de la coordination métallique des séquences de protéines de moule détient le potentiel d'avancer le développement de matériaux inspirés des moules supérieurs. Cette thèse est composée de trois études qui cherchent à adapter et à utiliser les principes de conception trouvés dans le byssus pour créer de nouveaux matériaux synthétiques avec une structure hiérarchique complexe et des caractéristiques de matériaux avancées, telles que l'auto-réparation, la réactivité aux stimuli et l'injectabilité. Dans la première étude, nous avons conçu un hydrogel granulaire injectable composé de microgels interconnectés. Les microgels ont été recuits en utilisant la coordination histidine-zinc, s'inspirant de la séquence protéique utilisée par les moules marines dans l'assemblage de fibres collagènes robustes et auto-réparatrices à partir de précurseurs de cristaux liquides. Ce cadre injectable démontre une excellente viabilité cellulaire, adhérence cellulaire et étalement cellulaire, le rendant très prometteur pour les applications de réparation de tissus. Dans la deuxième étude, s'inspirant de la chimie adhésive du byssus, nous avons profité de la coordination vanadium-catéchol forte mais réversible pour créer des films thermochromiques pliables et auto-réparateurs. Les interactions entre les nanoparticules de VO_2 et les polymères modifiés par catéchol servent de pierre angulaire, conférant aux films à la fois flexibilité et capacité d'auto-réparation lorsqu'ils sont soumis à des dommages, tout en préservant la réponse thermochromique des nanoparticules. Dans la troisième étude, notre objectif était d'élucider les facteurs contribuant à la performance supérieure des protéines byssales riches en DOPA natives par rapport aux polymères fonctionnalisés synthétiques DOPA, dans lesquels le motif catéchol DOPA est utilisé hors du contexte de la séquence protéique native. Nous avons mené une analyse comparative des capacités de liaison métallique entre les

polymères fonctionnalisés par catéchol et ceux fonctionnalisés par de fragments de peptides avec des séquences directement dérivées de la protéine de moule riche en DOPA (mfp-1) (c'est-à-dire, les catéchols sont dans leur contexte natif). Cette étude a mis en évidence le rôle de la séquence native dans la modulation de la liaison aux métaux (par exemple, l'affinité pour les métaux, le pH optimal de liaison aux métaux) et a donné un aperçu de la manière de concevoir de meilleurs polymères inspirés des moules.

Acknowledgments

My journey through graduate school, like many others, has been a mosaic of successes and setbacks, marked by a spectrum of emotions. This journey has imparted valuable lessons in resilience and problem-solving skills that extend into essential life lessons. Each challenge I encountered and every obstacle I overcame has contributed to shaping my academic abilities and refining my capacity to navigate life's complexities with a more balanced and informed perspective.

The support and guidance I received throughout this period have been instrumental. I have been fortunate to be surrounded by mentors, peers, and family who have provided unlimited support and invaluable insights, contributing profoundly to my personal and professional development.

I extend my deepest gratitude to my advisor and mentor, Prof. Matthew Harrington. His unwavering support and inspiration have been pivotal throughout my six-year doctoral pursuit. Joining his lab as a novice in biomaterials and soft materials research, Prof. Harrington's guidance was instrumental in nurturing my growth in this fascinating field. He provided me with abundant freedom and resources for my experiments, fostering an environment where new ideas flourished without pressure, even when outcomes were unforeseeable. His willingness to share his own doctoral experiences and his encouragement during times of frustration were invaluable. I think everyone in the department can agree with me that Matt is the nicest person you can meet, and without his mentorship I would not be where I am today.

I am profoundly thankful to my parents, Mohammad and Noura Rammal, for their immeasurable sacrifices that have enabled me to reach this stage. To my siblings, Hadi and Sanaa Rammal, your constant support and cheer have been a source of strength during moments of research frustration.

My heartfelt thanks go to the entire Harrington lab family - Tobias Priemel, Max Renner-Rao, Lucia Youssef, Hamideh Rezvani Alanagh, Jenaes Siva, Stephen George, Sam Jee, Guido Merino, Mathieu Rivard, Nathalie Singh, Mihai Mesko, Mimi Simmons, and Gagan Daliaho - for making these past six years truly memorable. A special note of gratitude to Tobias Priemel for his initiative in organizing departmental sports events, which significantly contributed to my physical and mental well-being. Special thanks to Stephanie Bazylevych for the unwavering support and encouragement. I am deeply grateful!

I want to express my gratitude to my undergraduate supervisor, Prof. Mazen Al Ghoul, who introduced me to the world of research and guided me through it. Thank you for the countless coffee-fueled scientific conversations at Myriade! Without you, this wouldn't have been possible. Thank you.

I am grateful to my friend and roommate Daniel Saliba who was always there for me when I needed help and support. His companionship and reliability have been a source of comfort and strength, for which I will remain forever thankful.

Professors Hanadi Sleiman and Theo van de Ven have been integral to my journey, offering invaluable advice and insights during my yearly reviews. Their wisdom has been a guiding

light. I also extend my thanks to my thesis committee members for their involvement and contributions.

I must acknowledge the collaborative spirit of other groups within the Chemistry Department, particularly Moraes's lab, Tomislav's lab, and van de Ven's lab, for generously sharing resources during our lab's nascent stages. Special thanks to Nadim Saade and Alex Wahba for their expertise in mass spectrometry, and to Robin Stein for assistance with NMR measurements. Special thanks to Dr. Hatem Titi who helped me run and design multiple measurements. He is truly a jack of all trades, master of all.

Lastly, I am grateful to the funding bodies, particularly the Natural Sciences and Engineering Research Council (NSERC) and the Department of Chemistry at McGill University, for their financial support of my research.

Table of Contents

Table of Figures

Contribution to Original Knowledge

The first chapter offers a comprehensive literature review centered on the design and synthesis of metallosupramolecular self-healing hydrogels. This review critically examines the current challenges in existing systems, explores how nature utilizes metal coordination to construct materials with superior performance, and discusses how these natural strategies can inspire chemists and materials scientists in the development of more advanced materials. Chapter 2 provides a theoretical background for techniques not commonly used by chemists to characterize soft materials (rheological testing). It also highlights the common vibrational spectroscopy and bioconjugation techniques used in our studies.

In the third chapter, we present an injectable granular hydrogel scaffold, drawing inspiration from the histidine-zinc coordination chemistry used by marine mussels to form tough and self-healing collagenous fibers. Crucially, these annealed scaffolds, solidified through reversible but robust metal coordination bonds, offering a cytocompatible microenvironment that fosters excellent cell viability and proliferation. This development significantly contributes to the field and provides a versatile platform for advanced biomedical applications.

In the fourth chapter, inspired by vanadium-catechol coordination in the mussel byssus cuticle, we pioneered a room-temperature method for the development of flexible, self-healing, and efficient thermochromic soft materials. The presence of vanadium nanoparticles results in the formation of sacrificial metal coordination bonds, establishing a reversible network capable of bearing loads without compromising extensibility for stiffness.

The last study aimed to elucidate the factors contributing to the superior performance of native DOPA-rich byssus proteins in comparison to synthetic DOPA-functionalized polymers, where the DOPA catechol moiety is utilized outside the context of the native protein sequence. We conducted a comparative examination of the metal-binding properties of catechol-functionalized polymers versus those functionalized with short peptides directly derived from DOPA-rich mussel foot protein (mfp-1), thus maintaining catechols in their native context. This investigation revealed the significant influence of other amino acids in the protein sequence on metal-binding characteristics, such as metal affinity and optimal pH for metal binding. These insights are crucial to guide the development of mussel-inspired polymers with biological relevance and superior mechanics.

Contribution of Authors

All the research presented in this thesis was conducted under the expert supervision of Professor **Matthew J. Harrington (MJH)**. Not only did he supervise the intellectual aspects of every project detailed in this thesis, but also offered invaluable guidance throughout their development and provided critical revisions for all manuscripts.

Chapters 1 and 2. These chapters were written by Mostafa Rammal and edited by Prof. Matthew Harrington. All figures in these two chapters were adapted from previously published images. Some figures have been subjected to minor modifications. Acknowledgments and necessary permission for these figures are noted in their respective descriptions.

Chapter 3: This chapter was written by Mostafa Rammal and edited by Prof. Matthew Harrington. Unless otherwise stated, the experimental work was designed and executed by

Mostafa Rammal. James Reeves and Chen Li carried out the cytotoxicity studies in the lab of Prof. Christopher Moraes. Prof. Moraes also helped edit the manuscript and assisted with the revisions.

Chapter 4: This chapter was written by Mostafa Rammal and edited by Prof. Matthew Harrington. Unless otherwise stated, the experimental work was designed and executed by Mostafa Rammal. Dr. Antranik Jonderian acquired the SEM images of the VO_2 nanoparticles. Dr. Hatem Titti assisted with the TGA, DSC, and PXRD measurements.

Chapter 5: This chapter was written by Mostafa Rammal and edited by Prof. Matthew Harrington. Prof. Steve Bourgault (UQAM) helped design and plan the experiments, and all peptides used were synthesized by his PhD student Margaryta Babych. UV-Vis measurements were done using the equipment of Prof. Amy Blum. The cytocompatibility study was conducted by Dr.Sabra Rostami in Prof.Chris Moraes's lab.

List of Abbreviations

2D	Two dimensional
3D	Three dimensional
UV	Ultraviolet
UV-Vis	Ultraviolet-Visible
SEM	Scanning electron microscopy
MAP	Microporous annealed particles
IR	Infrared
TEA	Triethylamine
TFA	Trifluoroacetic acid
PBS	Phosphate-buffered saline
HPLC	High-pressure liquid chromatography
LC	Liquid chromatography
MS	Mass spectrometry
TOF	Time of flight
HRD	Histidine-rich domains
NMR	Nuclear magnetic resonance
Mfp1	Mussel-foot protein
DOPA	Dihydroxyphenylalanine
NA	Numerical aperture

NG	Non-gradient
PXRD	Powder X-ray diffraction
TGA	Thermogravimetric analysis
DSC	Differential scanning calorimetry
EDC	1-Ethyl-3-(3-dimethylaminopropyl) carbodiimide
NHS	N-Hydroxysuccinimide
Sulfo-NHS	N-hydroxysulfosuccinimide
PEG	Polyethylene glycol
RT	Room temperature
DMF	N,N-Dimethylmethanamide
CCD	Charge coupled device
MAL	Maleimide
DMSO	Dimethyl sulfoxide
PreCol	Prepepsinized collagen
STEM	Scanning transmission electron microscopy
EDS	Energy dispersive X-ray spectroscopy
PDMS	Polydimethylsiloxane
EDTA	Ethylenediaminetetraacetic acid
FBS	Fetal bovine serum
DMEM	Dulbecco's Modified Eagle Media

EthD	Ethidium homodimer-1
PEG-dopa$_4$	4-arm polyethylene glycol terminated with 4 DOPA groups
µ-CT	Micro-computed tomography
XAS	X-ray absorption spectroscopy
NP	Nanoparticle

Chapter 1 : Introduction

1.1 Supramolecular Polymeric Hydrogels: Design and Preparation

Hydrogels are three-dimensional networks composed of hydrophilic polymers swelled in water. Owing to their biocompatibility, mechanical tunability, and low permeability, synthetic hydrogels have attracted considerable attention mainly on account of their wide range of applications, including as cell culture media[1], drug delivery systems[2], and superabsorbent materials[3]. Over the past few decades, there has been an exponential growth in the number of publications in this field, especially in the fabrication of novel biomedical materials.[4] This growth has been fueled by the ability to design hydrogels that mimic the viscoelastic properties of the extracellular matrix and control the release of growth factors, cells, and drugs as well as support cell proliferation and migration.[5, 6] Polymeric hydrogels can be classified into two main categories based on the type of crosslinks connecting the polymer network together, which can be either chemical or physical in nature. Chemical crosslinking of polymer chains using irreversible covalent bonds has traditionally been used to form hydrogels for various applications. This technique has been frequently used when stable hydrogels are needed because it leads to stiff gels that can be mechanically tuned using different types of covalent bonds. Numerous covalent reactions have been employed to fabricate chemical hydrogels, such as Schiff base[7], Michael-type addition reactions[8], free radical chain polymerization[9], and Click chemistry[10]. Although this process results in a 3D network that can both trap water and support their own weight, these hydrogels usually suffer from brittleness and lack dynamic and self-healing properties. Moreover, the static nature of covalent hydrogels prohibits injectability and generally precludes imparting responsiveness to

the material.[11, 12] To address these limitations, physical hydrogels based on supramolecular reversible bonds have received a great deal of interest in recent years due to the dynamic nature of these crosslinks.[13] Molecular self-assembly, wherein molecules spontaneously organize themselves into ordered aggregates, serves as the primary mechanism for gelation in aqueous environments. This process eliminates the need for additional crosslinking agents and facilitates a smooth sol-gel transition.

As shown in Figure 1.1, supramolecular hydrogels are formed when macromolecules self-assemble spontaneously into a three-dimensional network via a broad range of dynamic non-covalent interactions, including electrostatic interactions[14], hydrogen bonding[15], host-guest interactions[16], metal coordination bonds[17], π-π interactions[18], and hydrophobic effect[19].

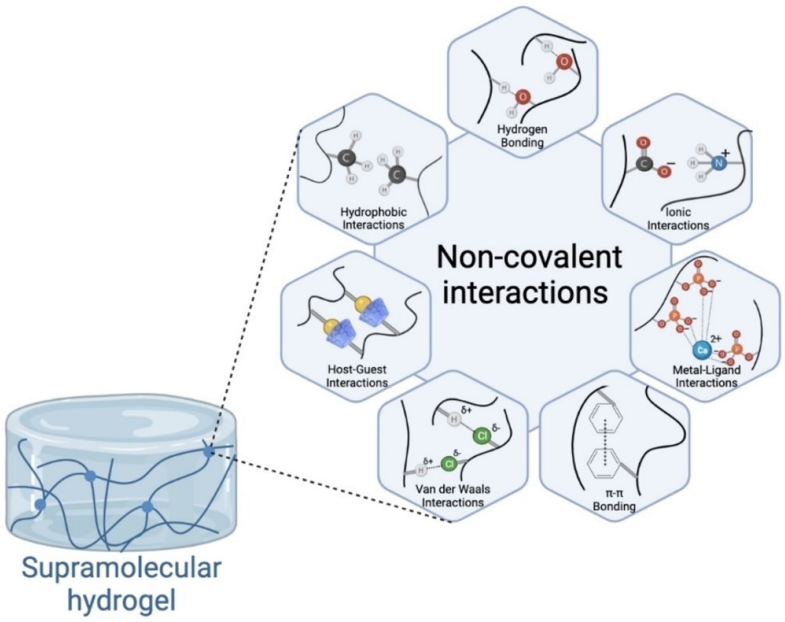

Figure 1.1: Common noncovalent interactions used to fabricate supramolecular hydrogels. Adapted from ref.[20]

Due to the lower bond energies of noncovalent interactions, physical crosslinking usually leads to weaker gels that are more susceptible to breaking under applied force compared to

covalent gels. However, the dynamic nature of physical crosslinks is favorable as it is the foundation of the thixotropic (drop in viscosity under shear) and self-healing behavior of supramolecular hydrogels.[4]

Design Parameters for Adaptable Hydrogels:

When it comes to engineering supramolecular hydrogels with specific properties, the main design considerations for the noncovalent interactions are the binding mode, equilibrium binding constant (K_{eq}), and the binding kinetics, defined by the rate of association (k_a) and dissociation (k_d). Each factor is described in more detail below.

Binding Modes:

The combination of side-chain functional polymers with supramolecular moieties capable of dynamically crosslinking the polymer chains via complementary or self-complementary binding motifs is a standard method for creating supramolecular polymeric hydrogels.[21] As shown in Figure 3, supramolecular motifs can interact in a self-complementary fashion through A:A motif (interaction between two identical moieties) and this is quite common in molecules capable of hydrogen bonding.[22] Furthermore, self-complementary designs can exhibit an A:B motif, where two identical molecules engage through distinct active groups. This is exemplified in the case of 'double-sided' discotic molecules, which utilize diverse interaction sites for association. (Fig. 1.2a). On the other hand, complementary binding appears commonly in A:B or A_2B (Fig.1.2b) or three components A:B:C (Fig.1.2.c) motifs. Understanding the process by which

supramolecular crosslinks are assembled has a significant influence on the formulation of supramolecular hydrogels and their resulting mechanical properties.

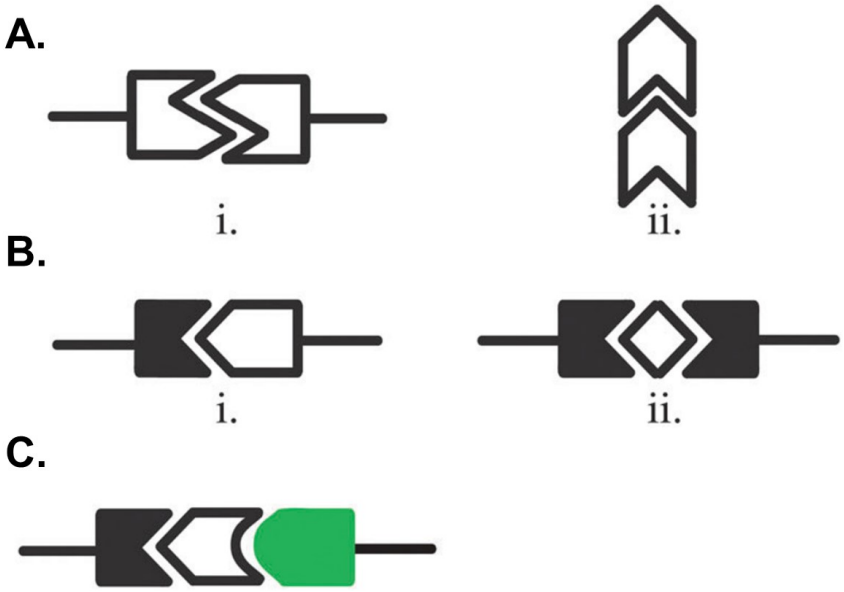

Figure 1.2: Supramolecular moieties are specific, directional, and can have different binding modes. (A) Self-complementary motifs with (i) complementary A:A or (ii) A:B interactions. (B) complementary motifs linked by (i) A:B or (ii) A:B:A interactions. (C) Three component binding using three complementary interactions A:B:C Adapted with permission from ref.[21]

Equilibrium constant:

The Equilibrium constant (K_{eq}) is a critical factor to consider when designing supramolecular hydrogels. This is due to the fact that the degree of association of supramolecular moieties is proportional to $(K_{eq}C)^{1/2}$, where C is the concentration.[23] Since the degree of association/polymerization has a significant influence on polymer length or the polymer network

structure, control over K_{eq} through changing the chemical structure of the moieties, for example, can affect the resulting properties of the hydrogels produced from the supramolecular polymers.

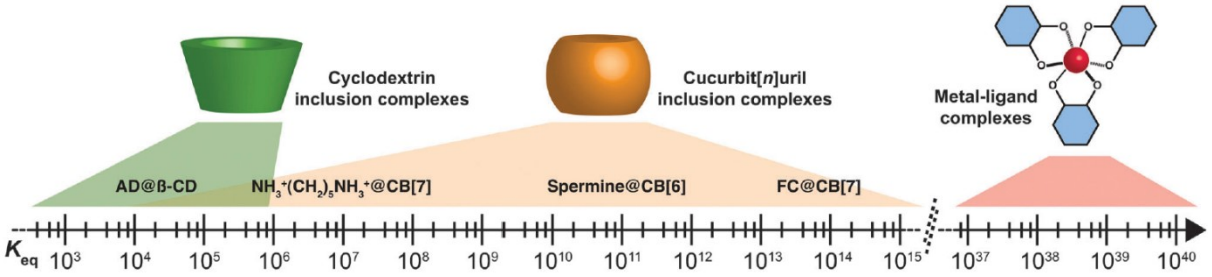

Figure 1.3: Schematic representation of common supramolecular binding motifs to prepare supramolecular polymeric hydrogels, showing the wide range of equilibrium constants. Cyclodextrin inclusion complexes (Green), cucurbit[n]uril inclusion complexes (orange), Metal-ligand complexes (pink). Adapted with permission from ref.[21]

In a given system, hydrogel formation takes place at a particular "gelation transition" when a contiguous network evolves from a percolated structure (connected network) at a critical concentration. This means that crosslinks with higher equilibrium constants will reach this percolation limit at lower concentrations.[21] Various supramolecular interactions have been exploited to prepare polymeric hydrogels with a wide range of equilibrium binding constants (Fig. 1.3). Unlike covalently crosslinked networks where the crosslink density can only be measured after the crosslinking reaction takes place, crosslink densities can be measured at any point given the equilibrium constant K_{eq} and the concentration of the bonding moieties. A complete understanding of the thermodynamics of the supramolecular interaction is also crucial when trying to connect the hydrogel mechanics to the binding dynamic.

Binding dynamics:

Several studies have shown that the dynamics, rather than the thermodynamic stability of reversible crosslinks, has a greater impact on the mechanical relaxation properties of supramolecular hydrogels.[24] The time scale of supramolecular association along with the association and dissociation rates of the crosslink, are crucial parameters when it comes to engineering the relaxation times and viscoelastic mechanics of supramolecular materials.[25] Figure 1.4 shows an example of a reversible association reaction between two complementary motifs. In this case, the associated complex represents an active crosslink, and the broken complex represents an inactive crosslink. Knowledge of the timescales of the association (k_a) and dissociation (k_d) is crucial to understand the mechanical behavior of hydrogels.

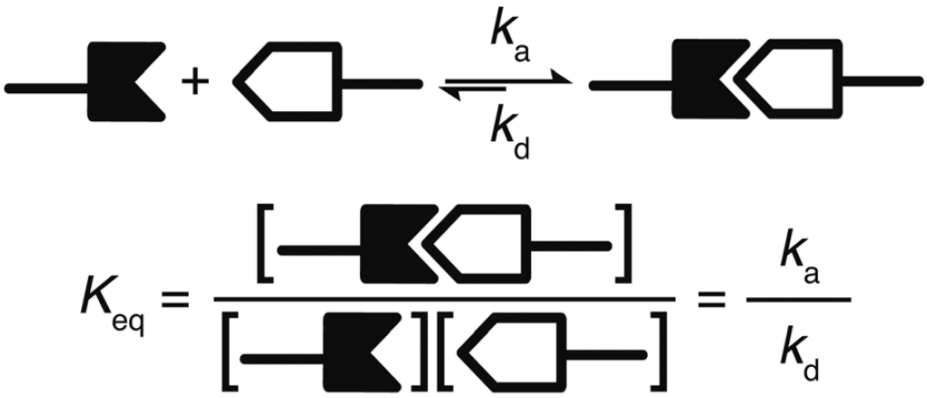

Figure 1.4: Schematic representation of reversible complementary association. The equation above shows the relationship between the thermodynamics and kinetics of supramolecular interactions. Adapted with permission from ref.[21]

The relationship between the bond kinetics and the mechanical properties of the network is still not fully understood. However, two seminal studies in the field of supramolecular materials performed by Annable et al.[26] and Yount et al.[24] demonstrated that the bond kinetics exert a stronger effect than bond thermodynamics over the dynamic mechanical behavior of supramolecular networks. In the first study, hydrogels were made using a telechelic block copolymer system with the configuration A-B-A, where A represents a hydrophobic block, and B represents a hydrophilic block.[26] Above the critical micelle concentration, the hydrophobic chains assemble into micelles that crosslink together to form a hydrogel. These hydrophobic chains are transient because they can move from one micelle to another. Annable et al. found that the relaxation time of the hydrogel can be tuned through changing the length of the hydrophobic block, where longer blocks led to slower relaxation of the network .[26]

Yount et al. arrived at the same conclusion using poly(4-vinyl pyridine) crosslinked with either platinum or palladium pincer complexes.[24] In this study, the authors were able to alter the pyridine-metal exchange kinetics without affecting the thermodynamics by sterically hindering the pincer complex near the complexing metal center. This produced a collection of complexes with nearly equivalent equilibrium binding constants but with dissociation constants (k_d) that differed by orders of magnitude. This showed that dissociation dynamics, rather than thermodynamics, control the relaxation modulus of these supramolecular hydrogels with slower dissociation linked to slower mechanical relaxation behavior and higher strength.

1.2 **Metallosupramolecular Self-Healing Hydrogels**

Metal coordination has been extensively studied due to its many crucial biological roles that encompass vital processes in different natural organisms, including catalysis in enzymes, gas transport, electron transfer processes, and signalling.[27, 28] For example, oxygen binding and transport is regulated by hemoglobin, which contains iron bound to the heme groups.[29] In addition to these more physiological roles, metal coordination with histidine, catechol, and aspartate residues as ligands has been discovered as a crosslinking mechanism in a number of different organisms, including various marine organisms (mussels, marine worms), as well as insect and spider biting parts.[30] In these materials, it has been demonstrated that metal coordination bonds act as load-bearing bonds that contribute to material hardness, stiffness, toughness, and even self-healing capacity.[31, 32] Inspired by these natural systems, metal coordination chemistry has been exploited by humans to make high-performance soft materials taking advantage of the desirable properties of these interactions.[20] Metallosupramolecular hydrogels have been created using polymer backbones with dangling chelating ligands with high affinity to metals. Upon the addition of the metal ions, coordinate bonds are formed through the donation of two electrons from the ligand to the empty orbitals of the metal ion. Metal crosslinks have binding strength values that can range from the strength typically associated with noncovalent interaction (H-bond, host-guest interactions) up to the strength of a covalent bond; however, unlike covalent bonds that function as permanent crosslinkers due to their high strength and thermodynamic stability, some metal coordination bonds exhibit high kinetic lability (transient bonds) at the cost of lower thermodynamic stability.[31] Hydrogels crosslinked using metal-ligand coordination present unique and intriguing features due to the distinctive

properties of metal coordination bonds. For example, the strong yet inherently reversible nature of coordination bonds offers notable advantages compared to traditional covalent crosslinking techniques, facilitating the advancement of hydrogels that possess complete self-healing capabilities.[17] Hence, the notable advantage of metal coordination resides in the ability to form strong connections without sacrificing reversibility and kinetic lability.

1.2.1 Design Parameters: Engineering Metal-Coordinated Hydrogels

Metallosupramolecular hydrogels, formed using long polymer chains terminated with ligands bound to a metal center, attracted a lot of attention due to their desirable mechanical properties. Metal coordination bonds, in contrast to conventional covalent bonds, have the ability to reform after breakage, allowing dynamic, tunable, and self-healing mechanical properties. Moreover, the introduction of metal coordination crosslinks in the hydrogel network brings additional physical and chemical characteristics to the material, like magnetic[33], photochemical [34], and catalytic capabilities [35]. When designing metallosupramolecular hydrogels, several design levers can be manipulated to achieve desired properties and functionalities.

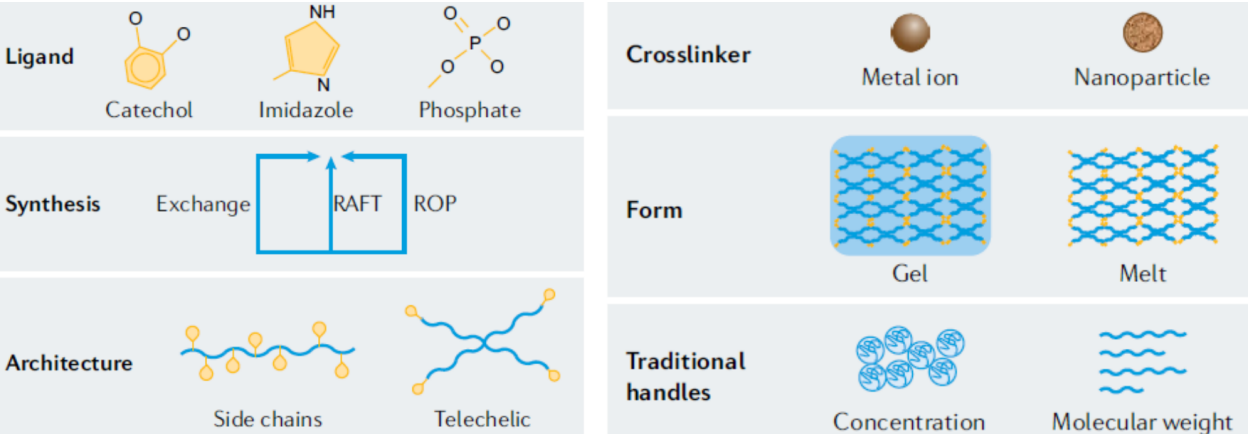

Figure 1.5: Design parameters for engineering metal-crosslinked polymers. Adapted with permission from ref.[31]

1) **Polymer architecture**: The choice of the polymer can have a large impact on the mechanical properties of the hydrogel. Different polymers have different flexibility, hydrophilicity, and interactions with metal ions, leading to a different mechanical performance. Moreover, the arrangement of the ligands on the polymer chains can affect the crosslinking density, which dictates the stiffness of the hydrogel.[36] For instance, polymers with pendant ligands allow a higher number of crosslinks compared to telechelic polymers (polymers terminated with ligands), which yield higher stiffness values and slower prolonged relaxation times.

2) **Polymer synthesis method**: The method used to synthesize the polymer functionalized with coordinating ligands can yield varying degrees of control over molecular weight, branching, and polydispersity. These factors, in turn, affect the overall mechanical

behavior of the hydrogel. Several polymerization techniques have been employed to design metal coordination hydrogels, including solution polymerization[37], reversible addition-fragmentation transfer (RAFT)[38], and grafting.[39]

3) **Ligand type**: Chelating ligands can be added to the polymer chain through copolymerization with the hydrogel precursor or by conjugation to the prepolymerized backbone. The choice of a ligand with a high binding affinity to the metal ion is crucial to designing hydrogels with desirable mechanical properties.[40] Ligands can also be tailored to exhibit responsiveness to external stimuli and biological recognition, allowing interaction with biomolecules, such as enzymes and cells. Various ligands such as catechol, histidine, phosphate, pyridine, terpyridine, etc., have been conjugated to biocompatible polymers such as alginate, hyaluronic acid, and PEG used to make high-performance metallosupramolecular hydrogels.[31, 41-43]

4) **Crosslinker type**: The metal crosslinker is crucial in the formation and stabilization of the hydrogel network. It functions as a nodal point connecting the polymer chains together by binding to the coordinating ligands. Each metal has a preferred geometry, oxidation states, and coordination number. The thermodynamics and the kinetics of the coordinate bond can control the mechanical performance and can be tuned by changing the metal ion to suit the application in mind. For example, Fullenkamp et al. showed that the relaxation time of PEG-histidine gels changes drastically by changing the metal crosslinker.[40] Recent studies showed that replacing metal ions with nanoparticles can

impart magnetic and thermal actuation in the materials and affect the relaxation behavior of the material. For example, Li et al. reported a hydrogel based on PEG-catechol polymer crosslinked with iron oxide nanoparticles exhibits magnetic properties and relaxes much slower than the gel crosslinked with metal ions.[41]

1.2.2 Thermodynamics and Kinetic Aspects of Metal-Coordination

As discussed earlier, the formation of the hydrogel network depends on the equilibrium constant (K_{eq}) between the chelating ligands and the metal ion (thermodynamic properties). Metal crosslinks exhibit a wide range of K_{eq} values that can vary between 10^3 to 10^{40} (Fig. 1.6).

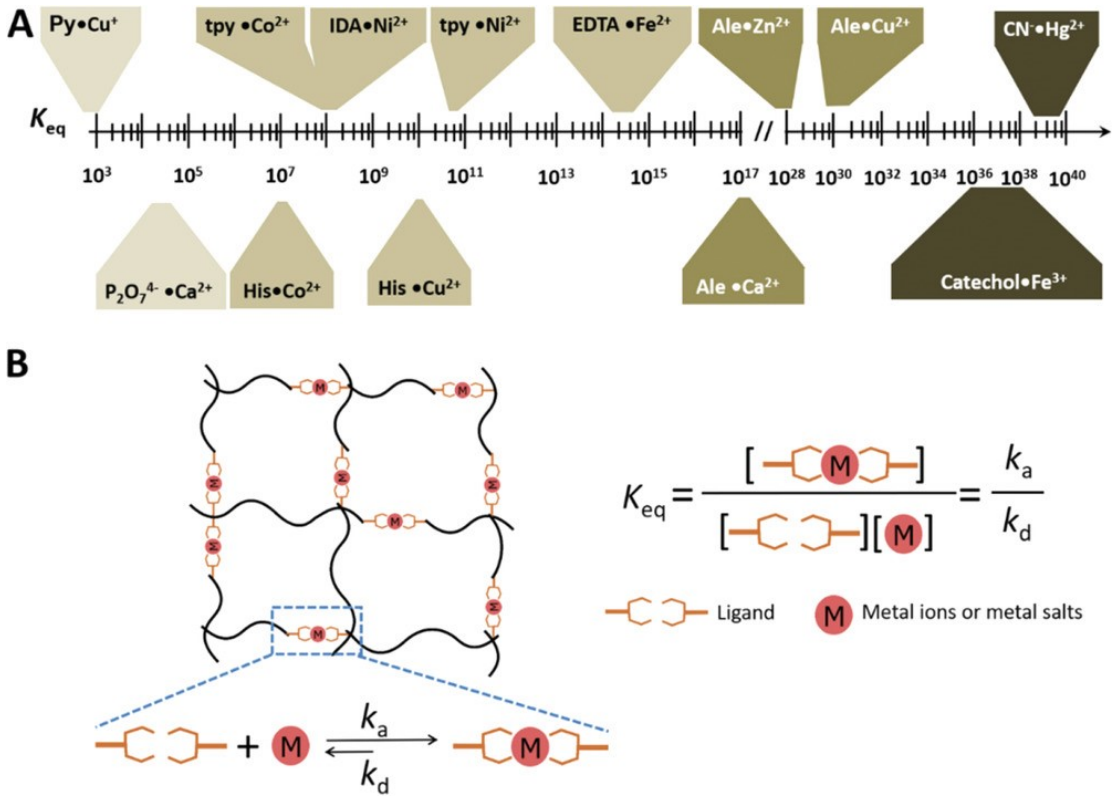

Figure 1.6: Thermodynamics and bonding dynamics of metal-coordinated hydrogels. (A) Survey of equilibrium constants (K_{eq}) common coordination bonds. Values can range between 10^3 (pyridine-Cu) and 10^{40} (cyanide-Hg). (B) Bonding dynamics of metal-coordinate bonds in self-healing hydrogels and expression of the binding constant K_{eq} for the metal coordination bonds

as a ratio of the association (k_a) and disassociation (k_d) rate constants. Adapted with permission from ref.[20]

This value determines the thermodynamic feasibility of network formation, as the degree of association between the metal and ligand depends on both concentration and K_{eq}. Hydrogels form above a critical crosslinking density, referred to as the 'gelation point,' indicating the presence of sufficient crosslinks to sustain the network structure. In metal-ligand systems with low K_{eq} values, hydrogel formation requires high concentrations, sometimes exceeding solubility limits. Conversely, excessively high binding constants can result in networks lacking dynamic behavior resembling covalent bonds. While thermodynamic properties play a pivotal role in determining hydrogel formation, the viscoelastic characteristics and relaxation times of hydrogel networks are governed by the kinetics of metal-ligand bonds, specifically the association and dissociation rate constants (k_a and k_d). In these networks, the metal-ligand complex serves as an active cross-linkage, while the dissociated complex is referred to as an inactive cross-linkage (Fig. 1.6).[20] Careful adjustment of the rate constants for association (k_a) and dissociation (k_d) is essential to align with the desired timescale of the intended application.[25, 44] This is crucial because slow dissociation kinetics (k_d), rather than bond strength, especially influence the material's mechanical properties, including viscosity and stiffness, whereas rapid reformation (k_a) is associated with quick gelation and rapid recovery after breakage. Hence, it is imperative to consider both the equilibrium constant (K_{eq}) and the rate constants (k_a and k_d) when engineering dynamic hydrogels. These factors play a significant role in determining the macroscopic mechanical properties and self-healing characteristics of the network. Hydrogels that utilize metal coordination as their supramolecular motif have the power to dramatically change the

thermodynamics and kinetics of their systems simply by changing the metal ion crosslinking the network together.[45, 46]

1.3 Metal Coordination in Marine Mussel Byssal Threads

Numerous organisms such as spiders, insects, marine worms, and mussels have been discovered to utilize metal coordination as load-bearing crosslinks in materials through the implementation of different amino acid residues like histidine and catechol as ligands in order to generate durable, non-mineralized, tough, and even self-healing materials.[47-49] Out of all these organisms, the marine mussel (in the genus Mytilus) has been extensively explored as a source of inspiration to develop high- performance metallosupramolecular materials and underwater adhesives. [17, 50, 51] Mussels are marine sessile bivalve species belonging to the family Mytilidae, which typically inhabit high intertidal zones on rocky seashores. These areas are characterized by permanent exposure to tidal fluctuations and crashing waves.[52] To endure the physical challenges of this habitat, mussels have evolved the ability to anchor themselves to different substrates through the utilization of self-assembled fibers known as byssal threads. Using a specialized organ called the foot, byssal threads are fabricated individually as a secretion of more than ten different protein building blocks that crosslink and organize into hierarchical structures (Fig. 1.7) .[53]

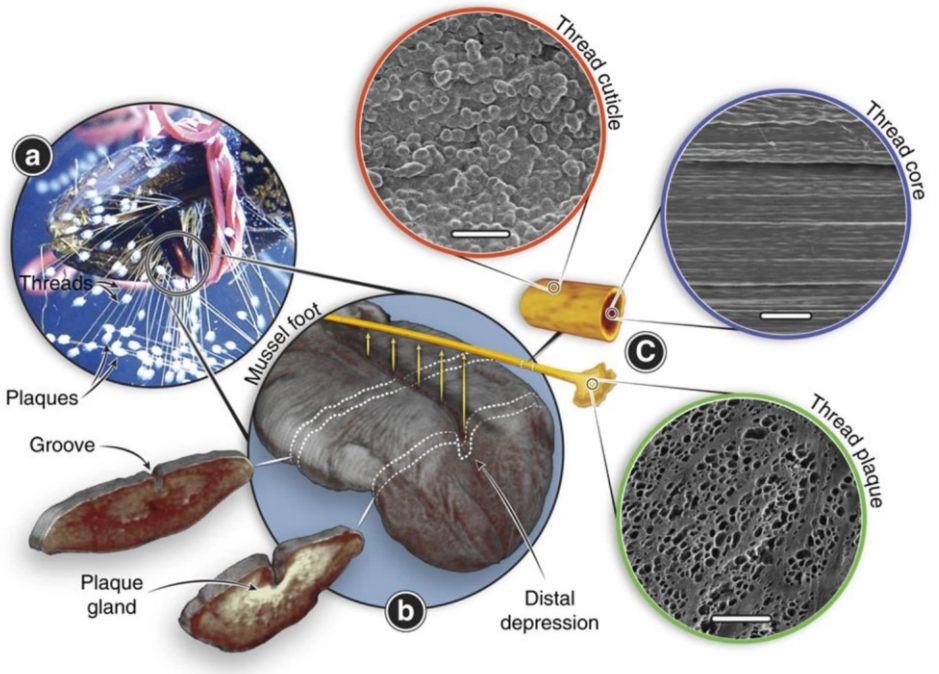

Figure 1.7: Anatomy and fabrication of the mussel byssus. (A) Marine mussels (*Mytilus edulis*) anchored to a surface using tough byssal threads. (B) Micro-computed tomography (μ-CT) scan depicting the underside of a mussel foot stained with iodine, showing two dissected segments to show the groove structure. (C) Scanning electron microscopy (SEM) pictures of a byssal thread that emphasize the intricate micron-sized structures of the shielding cuticle, fibrous central region, and adhesive plaque. Adapted from ref.[53], under Creative Commons license.

Along the foot, there is a trench-like channel called the ventral groove, which extends from the base to the tip and terminates with a small indentation known as the distal depression. This groove acts as a mold to form the byssal thread. A byssal thread is comprised of three distinct parts, namely the core, cuticle, and plaque, which are intricately combined to form a cohesive macrofiber, yet each part exhibits entirely different compositions, structural arrangements, and functions.[54] The compliant core of byssal threads is predominantly comprised of collagen-like proteins known as preCol proteins. These proteins can be described as “natural block

copolymers" due to their structure, consisting of a central collagen core block surrounded by two variable non-polar flanking domains and with two blocks that are rich in histidine residues at both termini. The byssal thread core exhibits an initial stiffness similar to that of vertebrate tendons, reaching approximately 900 MPa in some species.[55] However, in comparison to tendon, byssal threads possess greater toughness and extensibility, as well as self-healing capacity when subjected to cyclic loading.[56] Surrounding the stretchy core is a thin protective layer called the cuticle. This layer exhibits an exceptional combination of high hardness reaching 100 MPa in some species along with high extensibility (ε_{ult}=70-100 %).[53] A key to this unusual combination of properties is a cuticle protein known as mussel foot protein 1 (mfp-1), which is enriched in the amino acid 3,4-dihydroxyphenylalanine (DOPA), which will be discussed at length further on in the introduction.[57] Finally, the byssus is able to adhere to wet surfaces using a foamy adhesive structure called the plaque, which is composed of a number of DOPA-rich proteins (mfp-2,3,4,5 and 6).[58] Among the various notable properties of the mussel byssus, the main property that makes it attractive for bioinspiration is its self-healing capability under stress.[59] Several studies have shown that histidine-metal coordination (core) and DOPA-metal coordination (cuticle/plaque) contribute to the mechanical properties of the byssus, especially self-healing, inspiring the design of high-performance materials-based metal coordination bonds.[49, 50, 60, 61] The following sections will focus on each type of coordination separately, highlighting how the chemistry of the byssus can help inspire the development of materials that exhibit tunable mechanics, self-healing behavior and more.

1.3.1 Role of Sacrificial Histidine-Metal Coordination in the Core

The core of the byssal thread consists of collagen-like proteins, known as PreCols, arranged in a hierarchical semicrystalline manner. PreCols assemble in a 6+1 hexagonal bundles that are further arranged in semicrystalline arrays.[62] Each PreCol protein possesses two histidine-rich domains (~20 mol%) at the N- and C-termini of the proteins.[63] Several studies have provided evidence for the crucial role of these histidine-rich domains (HRDs) in both regulating the mechanical behavior of the byssal threads (e.g., toughness and self-healing) and guiding their assembly in a pH-dependent manner.[59] By employing spectroscopic techniques like Raman spectroscopy (Fig 1.8B) and X-ray absorption spectroscopy (XAS), it has been shown that the aforementioned mechanism is accomplished via precise interactions between histidine residues with transition metal ions, such as Zn^{2+} and Cu^{2+}.[50] The network's toughness is attributed to the coordination bonds, which are able to rupture sacrificially under high stress conditions, effectively preventing irreversible breakage of the covalent bonds and dissipating mechanical energy. In addition, the inherent mechanical properties of the threads can be recovered by means of the time-dependent reformation of the metal coordination bonding network in the HRDs, thus facilitating a robust self-healing response.

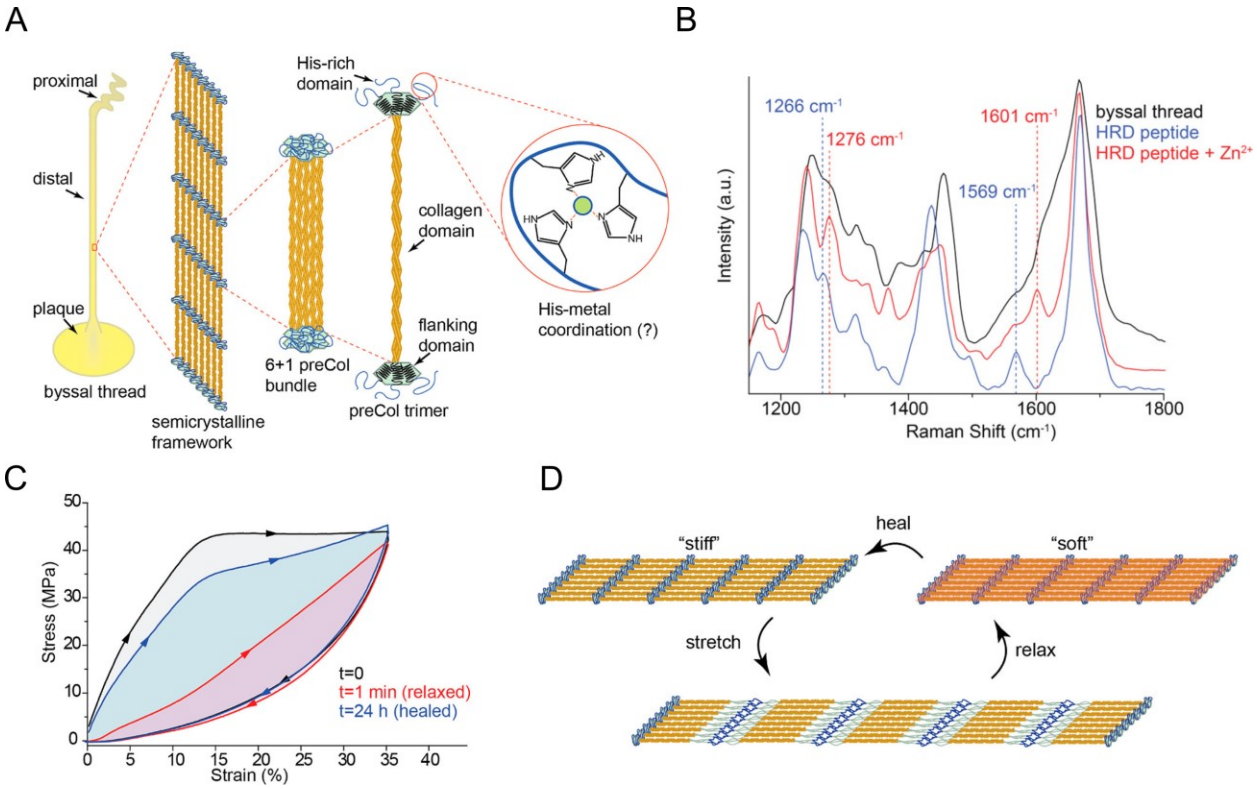

Figure 1.8: Sacrificial role of histidine metal coordination in the byssus core. (A) The byssus core, consisting of hierarchical semicrystalline domains of collagenous proteins (PreCols), grants the ability to withstand the impact of crashing waves. These semicrystalline domains are terminated by two histidine-rich domains (HRDs) that are known to coordinate metals like Zn^{2+} that play a crucial role in the mechanical toughness and self-healing properties of the mussel byssus. (B) Raman spectrum showing the signature peaks of histidine-zinc coordination in a synthetic HRD peptide. (C) During cyclic tensile testing, threads exhibit notable mechanical hysteresis but can undergo structural damage upon exposure to loads surpassing the yield point. (D) Self-healing is observed as a gradual process of restoration toward the initial properties over time. Upon the expansion of the flanking and histidine-rich domains, the structure and length of the semicrystalline preCol framework quickly return to their initial configuration. Nonetheless, the recovery of preCol stiffness occurs at a relatively gradual rate. Adapted with permission from ref.[50]

1.3.2 Role of Dopa-Metal Coordination in the Cuticle

The compliant core of the byssal thread is protected against wear and abrasion by a 5 µm thick proteinaceous outer cuticle (Fig. 1.9).[49] This layer possesses a unique combination of high hardness (five-fold harder than the core) and high extensibility.[64] TEM studies revealed that the cuticle has biphasic morphology consisting of granules embedded within a matrix.[65] Moreover, compositional analysis showed that the cuticle predominantly consists of mussel foot protein (mfp-1), a protein containing approximately 15 mol % 3,4 dihydroxyphenyl-L-alanine (DOPA), which is a post-translational modification of the amino acid tyrosine.[66] Besides DOPA, inorganic ions such as iron and vanadium have been identified in the matrix and granules, respectively (Fig. 1.9C) .

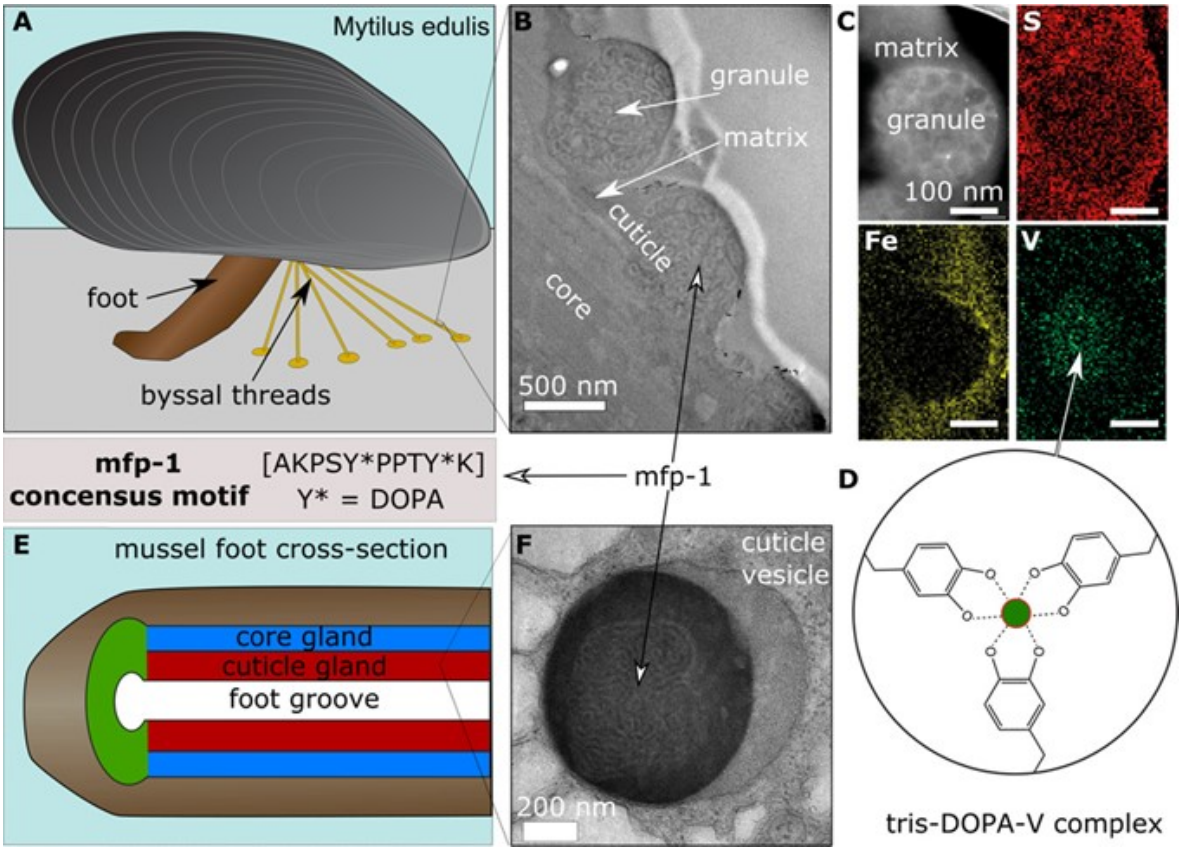

Figure 1.9: Structure and composition of the cuticle. (A) Using the foot, the mussel can produce tough fibers to attach to surface in high intertidal zones. (B) TEM image of the core and the cuticle highlighting the granules and matrix of the cuticle. (C) EDS analysis of various metals found in the cuticle, showing vanadium colocalized with mfp1 in the granules, while iron is found in the matrix. (D) DOPA-V tris coordination in the granules. (E) Before their formation, the proteins constituting byssal threads are stored within specialized glands in the mussel foot. They are subsequently secreted into the foot groove to form the thread. (F) TEM image displaying a secretory vesicle containing precursor proteins for the cuticle. Adapted with permission from ref.[67]

Raman spectroscopic measurements performed on the cuticle show that DOPA-rich mfp-1 proteins form strong coordination bonds with metal ions, indicated by resonant Raman peaks centered around 600 cm^{-1}.[49] Furthermore, 2D Raman mapping shows that the crosslink density of metal-DOPA is higher in the granules than the matrix. These crosslinks harden the granules, which contribute to the excellent mechanical performance of the mussel byssus. In addition to its ability to make strong and reversible metal-coordinate bonds, DOPA exhibits notable adhesive properties that allow it to stick to almost all kinds of surfaces.[68] DOPA can interact in many ways with ions or surfaces. For example, depending on the pH and stoichiometry, DOPA can bind iron for example in a mono (1.1), bis (1:2), or tris (1:3) fashion. It can also hydrogen bond to surfaces using the two hydroxyl groups on the benzene ring.[17] Furthermore, these DOPA-catechol moieties can oxidize to DOPA-quinone, which can form covalent diDOPA interactions or react with neighboring amino acids.[69] Previous investigations into catechol-based cross-linking within the mussel byssus cuticle predominantly assumed that Fe (iron) was the primary metal binding partner for DOPA (3,4-dihydroxyphenylalanine). However, recent spectroscopic evidence

suggests that vanadium may be more frequently employed as the cross-linking metal, particularly in cohesive cross-links found within the adhesive plaques and within the DOPA-rich cuticle granules.[70] In the cuticle, both Fe and V were previously detected in the coating. However, recent high-resolution spectroscopic imaging have enabled the specific localization of V within the DOPA-rich granules, while Fe has been identified in proximity to the sulfur-rich matrix situated between these granules (Fig. 1.9C).[65] Mesko and co-workers later showed that DOPA-vanadium provides increased cohesive forces than DOPA-Fe with studies using recombinant mfp-1 which further supports these observations.[67]

1.3.3 Mussel-Inspired Metallosupramolecular Materials

The remarkable mechanical properties displayed by the mussel byssal thread, cuticle and plaque have generated considerable interest among researchers who aim to create synthetic materials inspired by the chemistry and structure of the mussel byssus.[71] In the last decade, there has been an exponential rise in peer-reviewed articles that center on the creation of materials inspired by mussels. These studies exploit different chemistries, such as histidine-metal coordination and DOPA-metal coordination, and material design concepts used by marine mussels to create materials with strong cohesive and adhesive properties. Niels Holten-Andersen and colleagues kickstarted this field by introducing catechol groups on a telechelic four-arm PEG polymer, which could be crosslinked with iron slightly above physiological pH conditions to make a mussel- inspired hydrogel.[17] This hydrogel exhibited an interesting viscoelastic behavior with a relaxation time that depends strongly on pH with longer relaxation times observed at higher pH.

This material is also self-healing due to the ability of metal-DOPA crosslinks to reform after breakage. Inspired by the adhesive DOPA-rich proteins in the plaque, Messersmith and co-workers later developed an injectable surgical sealant that was approved for fetal membrane repair.[72] In general, DOPA-metal coordination chemistry has been employed in a variety of applications including conductive soft materials[73], drug delivery[74], cancer therapy[75], adhesives[76], and bioimaging[77].

There has been a smaller body of research dedicated to exploring materials based on histidine-metal coordination. Fullenkamp and co-workers pioneered this field by making self-healing hydrogel by crosslinking four-arm poly(ethylene glycol) terminated by histidine with divalent ions like Ni^{2+}, Co^{2+}, Cu^{2+}, and Zn^{2+}.[40] This study showed that the relaxation time of the hydrogel can be tuned by changing the metal crosslinker in a pattern depending on the ligand exchange rates, which were determined as follows: $Ni^{2+} > Co^{2+} > Cu^{2+} > Zn^{2+}$. Following this seminal work, Grindy and co-workers showed that by using two metals and by careful adjustment of their relative concentration, it is possible to manipulate the mechanical hierarchy of energy dissipating modes in the material when subjected to mechanical loading.[78] This allows engineering the desired viscoelastic properties of the materials in advance, without the need to change the polymer matrix. Recently, metal-histidine chemistry has been applied to different architectures such as resilin[79], mussel protein films[80], and synthetic peptide materials.[56]

1.4 Annealable Granular Hydrogels as Injectable Scaffolds

Due to their biocompatibility, high water content, and the ability to replicate the natural tissue environment, hydrogels present a viable platform for tissue repair applicatations.[81]

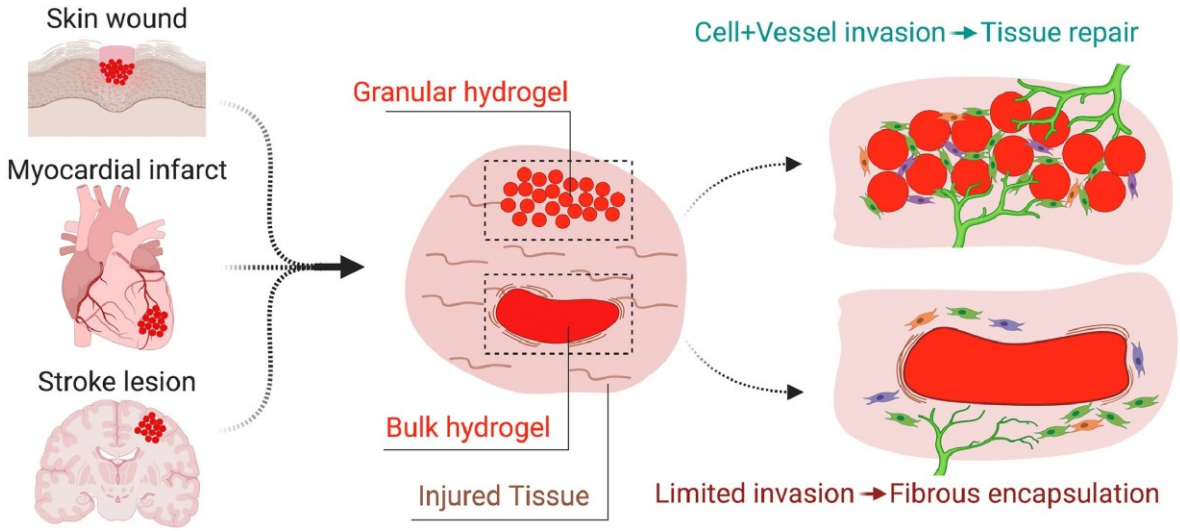

Figure 1.10: Examples of accelerated endogenous tissue repair using granular hydrogels. where their inherent porosity allows vascularization and cell infiltration which is usually limited in bulk hydrogels. Adapted with permission from ref.[82]

However, due to the high complexity of the native extracellular matrix (ECM), further developments are needed to optimize the hydrogel properties to enhance their efficacy in tissue repair and regeneration. Traditional hydrogels are formed by crosslinking a hydrophilic polymer in water to form a bulk material with a mesh size at the nanoscale, which allows molecular diffusion; however, the order of magnitude of cells is typically in the range of micrometers which prevents cell infiltration and vascularization in their structure when they are used in tissue repair applications.[82] Several methods have been used to introduce microporosity to bulk gels, such as

electrospinning[83], porogen leaching[84], and gas foaming[85]. However, these techniques are usually labor-intensive, and it is challenging to achieve a precise control over the pore size and distribution. Granular hydrogels, formed from jammed hydrogel microparticles (1-100 μm), offer an easy solution to the microporosity issue in bulk hydrogels in addition to several properties that made them attractive for several tissue repair applications (Fig. 1.10).

1.4.1 Hydrogel Microparticles Fabrication Methods

Hydrogel microparticles (HMPs) can be prepared using the same library of polymers used to make bulk gels, just processed at the microscale using different fabrication methods (Fig. 1.11). These methods differ in cost, scalability, polydispersity, and size range. Microgels are typically made using six different techniques: (1) Batch emulsion polymerization, (2) droplet microfluidics, (3) colloidal suspension method, (4) electrohydrodynamic spraying (5) lithography, (6) mechanical fragmentation. A summary of three techniques which are relevant to this thesis can be found below:

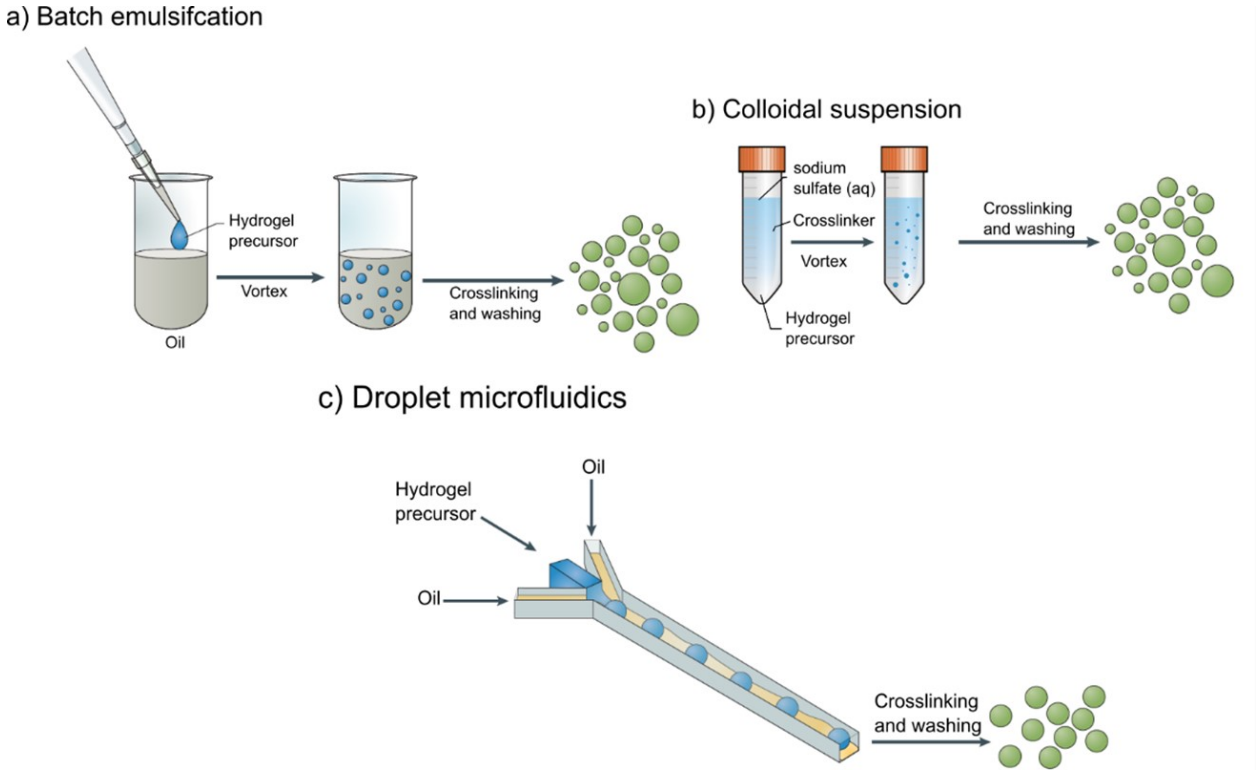

Figure 1.11: Common fabrication techniques of hydrogel microparticles (HMPs). Adapted with permission from ref.[86]

1. **Batch emulsion polymerization**: this method usually involves the combination of a hydrogel precursor (polymer) with another immiscible solvent (typically oil), followed by sonication or vigorous agitation to form microdroplets containing the hydrogel precursor dispersed in the oil phase. These droplets are stabilized by a surfactant, which lowers the interfacial tension by breaking the cohesive forces between the two phases. The size and dispersity of the droplet depend on the extent and duration of mixing. The obtained droplets are then crosslinked into microgels, and the oil phase is removed. The main advantages of this method are that it is easy and scalable, but it suffers from high polydispersity and poor reproducibility. [12]

2. **Colloidal suspension method**[87]: This method does not involve the use of two immiscible phases but rather takes advantage of phase separation of the hydrogel precursor (polymer) in an aqueous solution. At high salt concentration, polymer-polymer interactions become more favorable than solvent-polymer interactions which lead to the phase separation of the polymer, which can be later crosslinked into hydrogel microparticles. The main advantage of this method is that it does not require a surfactant, and it can be easily scaled up to produce industrial volumes of microgels. However, like the batch emulsion method, it suffers from poor size control and dispersity.
3. **Droplet Microfluidics**: The poor size control of microgels using the traditional batch emulsification method and colloidal suspension method prompted seminal research, which led to the use of flow-focusing microfluidic devices to achieve better control in the production of hydrogel microparticles. It involves the use of a chip that contains microsized channels connected in a well-defined way. As shown in Fig. 1.11, the hydrogel precursor and an immiscible oil phase are injected in the flow focusing device using syringe pumps. At the intersection, monodispersed microemulsions are formed, and the size can be controlled by fine-tuning the ratio between the two immiscible phases. This method can generate microgels with a diameter that ranges between 5 and 500 μm with a uniform size distribution.[12] The main limitations of this method include device complexity and low production volume. However, the use of parallel designs and millipede devices can help increase the production volume, while maintaining high monodispersity and size control.[88]

1.4.2 Functional Properties of Granular Hydrogels

Granular hydrogels exhibit a number of unique properties compared to bulk hydrogels that make them attractive for a wide range of biomedical applications.[86]

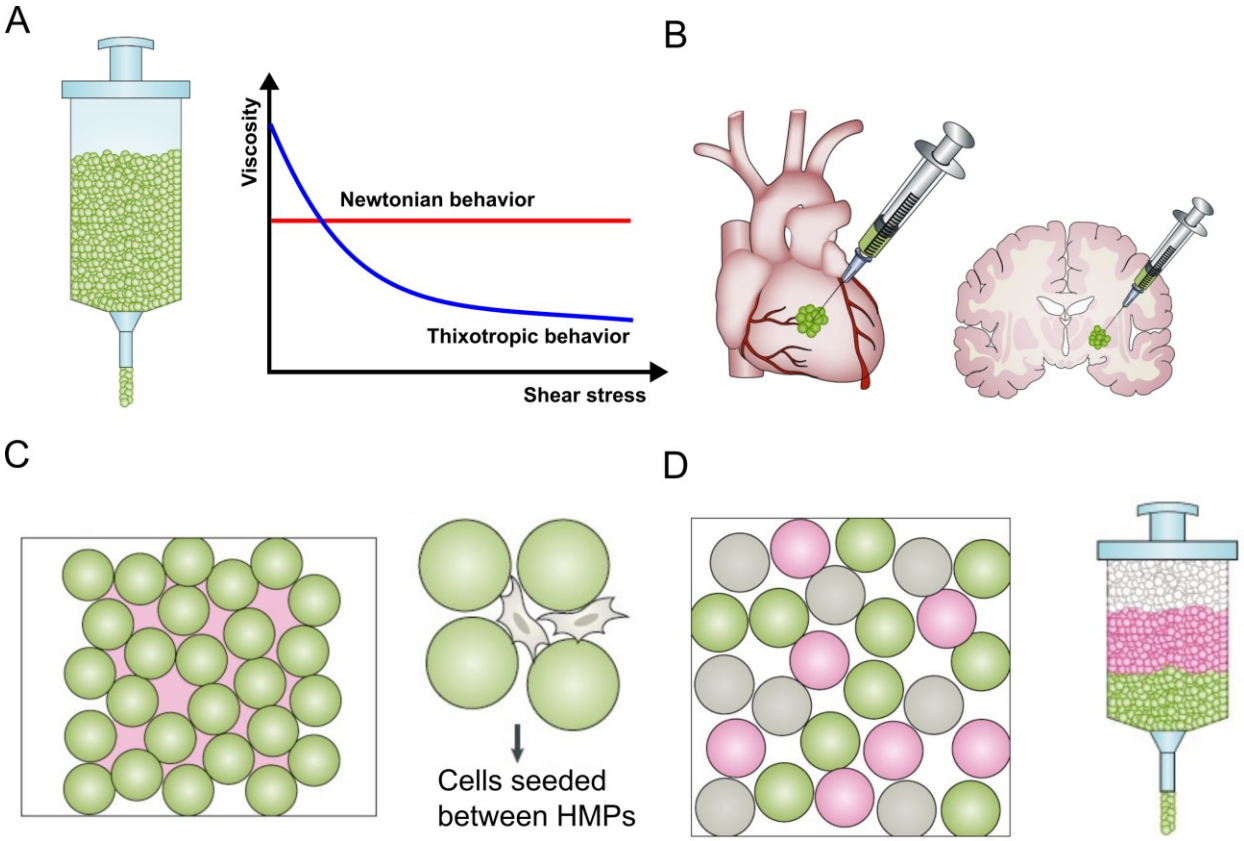

Figure 1.12: Functional properties of granular hydrogels. (A) Granular hydrogels exhibit a thixotropic behavior, which renders them injectable at high shear rates. (B) Due to their inherent shear-thinning properties, granular hydrogels are good candidates for intratissue delivery. (C) The inherent porosity of granular hydrogels can be controlled by the size of individual hydrogel particles, making them good candidates for cell culture applications. (D) Modularity through mixing different types of hydrogels microparticles allows the formation of multifunctional microporous annealed scaffolds. Adapted with permission from ref.[86]

1) **Microporosity** [82]:

Granular hydrogels possess an inherent porosity arising from the void spaces between the hydrogel microparticles. The size of the pores scales up with the size of the hydrogel microparticles, which can be easily controlled using microfluidics. Cells with diameter in this range can readily permeate, migrate, and proliferate within the granular hydrogel scaffold without the need for hydrogel degradation, which is necessary for bulk gels. This feature of granular hydrogel has been observed to augment mass transport of nutrients and oxygen, fluid flow, and cell infiltration rates compared to non-porous gels. The porosity of the scaffold can also be tuned by the shape, packing density, and the stiffness of the microgels.[16]

2) **Injectability** [12]:

Due to the small size of the HMPs, granular hydrogels can be easily injected into tissues using syringe needles or catheters. Granular hydrogels exhibit a shear-thinning behavior, which means they behave like bulk gels at rest, but flow like a liquid under shear. This ability has been utilized in various tissue repair applications such as wound healing because it allows minimally invasive procedures. For instance, in a minimally invasive way, modified hyaluronic acid HMPs were injected into the ischaemic sites within brain and cardiac tissues to promote wound healing. The thixotropic behavior of granular hydrogels depends on the frictional and electrostatic forces between the neighboring HMPs and becomes more influential at higher packing densities. The surface chemistry of the

microgels can be modified with noncovalent interactions to tune the shear-thinning behavior of granular hydrogels.

3) **Heterogeneity and Multifunctionality** [12]:

Heterogeneity, which arises from the ability to mix two or more different types of hydrogels microparticles introduces an additional complexity to the granular system leading to multifactorial effect at both the particle and system levels. For example, mixing or layering two types of microgels with different sizes can lead to varying porosity across the scaffold. Moreover, introducing HMPs with different mechanical properties can generate a scaffold with different mechanical properties at the microscale which can impact cellular behavior. Finally, microgels containing different biologics (cells and drugs) can be simultaneously injected in the tissue in a minimally invasive way.[73]

1.4.3 Limitations and Challenges in Dynamic Settings

There are several parameters that should be considered when engineering an injectable granular hydrogel for tissue repair applications. First, the choice and the concentration of the polymer to make the individual microgels is crucial for the mechanical properties of the granular hydrogel along with the packing density of the HMPs. Second, the porosity of the scaffold is usually tuned by controlling the size of microgels using microfluidics. Larger particles lead to granular hydrogels with larger pores, while smaller particles lead to smaller pores.

Designing injectable granular hydrogel for motile tissues repair applications, like cardiac tissues, is quite challenging because hydrogel microparticles will be dislodged from the injection site.[89] In order to enhance the mechanical characteristics of scaffolds and prevent particle detachment in dynamic tissue environments, hydrogel microparticles can be annealed together through diverse types of interactions (such as covalent, physical, hydrophobic, or electrostatic) to create microporous annealed particle (MAP) scaffolds.[90, 91] Currently, studies are primarily focused on utilizing annealing as a parameter to create MAP scaffolds that respond to stimuli under physiological conditions and exhibit controlled degradation behavior.[16]

Present annealing chemistries heavily rely on covalent crosslinking, which can be accomplished through click chemistry[92], carbodiimide chemistry[93], and light-mediated radical reactions[94]. These methods result in the production of mechanically robust and rigid scaffolds. However, the practical applications of these scaffolds are limited due to the absence of shear-thinning and self-healing properties, which can be attributed to the irreversible nature of covalent crosslinking. In contrast, granular systems that are crosslinked through physical means, such as electrostatic interactions[95] or host-guest interactions[16], demonstrate viscoelastic characteristics and thixotropic behavior upon injection. However, these systems are notably less mechanically durable than those crosslinked using covalent bonding. Clearly, there is plenty of room for improvement in order to achieve a robust annealable scaffold with long term stability at physiological conditions in dynamic tissue environments while preserving the porosity and injectability of the scaffold. Developed through millions of years of evolution, marine mussel byssus employs a combination of self-assembly and intricate metal coordination chemistry to make materials that outperform even the best synthetic materials. We believe that

understanding and replicating such natural systems can inspire the design of robust scaffolds that can revolutionize minimally invasive tissue repair applications.

1.5 Taking Inspiration from the Mussel Byssus for High Performance Soft Materials

Natural systems have evolved over hundreds of millions of years, developing complex and intricate structures with exceptional performance for a range of functions. This success largely stems from the tricks that have evolved involving materials chemistry and hierarchical self-assembly. To harness the potential of natural designs, bioinspiration has emerged as a powerful strategy. This approach aims for a thorough understanding of the physicochemical interactions at play within biological structures, seeking to translate these insights into innovative materials applications. For instance, numerous studies have demonstrated that biological systems have effectively utilized metal coordination cross-linking for ages to develop materials endowed with dynamic mechanical properties. While metal-coordination has been thoroughly investigated and exploited in the contexts of catalysis, biology and supramolecular chemistry, its application in the development of hydrogel materials has only begun to be explored in the last decade. Among the myriad examples in nature, marine mussels have captivated scientists with their remarkable adhesive, energy-dampening , and self-healing fibers.[71] Initial efforts have primarily focused on copying ligand moieties found in nature. However, a more detailed examination of the natural sequences involved in these processes could unveil novel insights and opportunities for innovation in materials science.

1.6 Aims and Scope of the Thesis

As mentioned earlier, the mussel's byssus serves as a crucial inspiration for a wide array of bioinspired materials, encompassing wet adhesives, self-repairing substances, and functionally graded materials. Inspired by the metal strategies in the byssus, this thesis endeavors to comprehend and apply metal coordination strategies to fabricate materials exhibiting improved mechanical properties. These advancements hold promise across a spectrum of material applications, spanning from injectable scaffolds designed for tissue repair to the development of thermochromic and self-healing hydrogels. In pursuit of this objective, I have adopted a multidisciplinary approach drawing upon expertise from polymer chemistry, bioconjugate chemistry, spectroscopy, and rheology. Herein, I present studies illustrating how strategies inspired by mussels contribute to the creation of polymeric systems that outperform conventional materials. These studies are detailed across three distinct chapters: 1) The first study aims at using histidine-zinc coordination as annealing strategy to make pH-Responsive reversible granular hydrogels based on metal-binding mussel-inspired peptides. 2) The second study attempts to develop a room-temperature process to fabricate thermochromic VO_2 hydrogels and elastomeric films inspired by the vanadium-catechol coordination chemistry. 3) The third study delves into examining dopamine's metal chelation behavior within the natural sequence. Leveraging this enhanced binding capability, I have developed the first annealable granular hydrogel system using iron-DOPA coordination. In chapter 6, we discuss potential applications, challenges, and future directions derived from these studies.

1.7 References

1. Caliari, S. R.; Burdick, J. A., A practical guide to hydrogels for cell culture. *Nature Methods* **2016,** *13* (5), 405-414.

2. Li, J.; Mooney, D. J., Designing hydrogels for controlled drug delivery. *Nature Reviews Materials* **2016,** *1* (12), 16071.

3. Cipriano, B. H.; Banik, S. J.; Sharma, R.; Rumore, D.; Hwang, W.; Briber, R. M.; Raghavan, S. R., Superabsorbent Hydrogels That Are Robust and Highly Stretchable. *Macromolecules* **2014,** *47* (13), 4445-4452.

4. Omar, J.; Ponsford, D.; Dreiss, C. A.; Lee, T.-C.; Loh, X. J., Supramolecular Hydrogels: Design Strategies and Contemporary Biomedical Applications. *Chemistry – An Asian Journal* **2022,** *17* (9), e202200081.

5. Chaudhuri, O.; Gu, L.; Klumpers, D.; Darnell, M.; Bencherif, S. A.; Weaver, J. C.; Huebsch, N.; Lee, H.-p.; Lippens, E.; Duda, G. N.; Mooney, D. J., Hydrogels with tunable stress relaxation regulate stem cell fate and activity. *Nature Materials* **2016,** *15* (3), 326-334.

6. Griffin, D. R.; Weaver, W. M.; Scumpia, P. O.; Di Carlo, D.; Segura, T., Accelerated wound healing by injectable microporous gel scaffolds assembled from annealed building blocks. *Nature Materials* **2015,** *14* (7), 737-744.

7. Yang, B.; Zhang, Y.; Zhang, X.; Tao, L.; Li, S.; Wei, Y., Facilely prepared inexpensive and biocompatible self-healing hydrogel: a new injectable cell therapy carrier. *Polymer Chemistry* **2012,** *3* (12), 3235-3238.

8. Tortora, M.; Cavalieri, F.; Chiessi, E.; Paradossi, G., Michael-Type Addition Reactions for the In Situ Formation of Poly(vinyl alcohol)-Based Hydrogels. *Biomacromolecules* **2007,** *8* (1), 209-214.

9. Nichol, J. W.; Koshy, S. T.; Bae, H.; Hwang, C. M.; Yamanlar, S.; Khademhosseini, A., Cell-laden microengineered gelatin methacrylate hydrogels. *Biomaterials* **2010,** *31* (21), 5536-5544.

10. Koschella, A.; Hartlieb, M.; Heinze, T., A “click-chemistry” approach to cellulose-based hydrogels. *Carbohydrate Polymers* **2011,** *86* (1), 154-161.

11. Ferreira, N. N.; Ferreira, L. M. B.; Cardoso, V. M. O.; Boni, F. I.; Souza, A. L. R.; Gremião, M. P. D., Recent advances in smart hydrogels for biomedical applications: From self-assembly to functional approaches. *European Polymer Journal* **2018,** *99*, 117-133.

12. Daly, A. C.; Riley, L.; Segura, T.; Burdick, J. A., Hydrogel microparticles for biomedical applications. *Nature Reviews Materials* **2020,** *5* (1), 20-43.

13. Lim, J. Y. C.; Lin, Q.; Xue, K.; Loh, X. J., Recent advances in supramolecular hydrogels for biomedical applications. *Materials Today Advances* **2019,** *3*, 100021.

14. Huebsch, N.; Arany, P. R.; Mao, A. S.; Shvartsman, D.; Ali, O. A.; Bencherif, S. A.; Rivera-Feliciano, J.; Mooney, D. J., Harnessing traction-mediated manipulation of the cell/matrix interface to control stem-cell fate. *Nature Materials* **2010,** *9* (6), 518-526.

15. Guo, M.; Pitet, L. M.; Wyss, H. M.; Vos, M.; Dankers, P. Y. W.; Meijer, E. W., Tough Stimuli-Responsive Supramolecular Hydrogels with Hydrogen-Bonding Network Junctions. *Journal of the American Chemical Society* **2014,** *136* (19), 6969-6977.

16. Mealy, J. E.; Chung, J. J.; Jeong, H.-H.; Issadore, D.; Lee, D.; Atluri, P.; Burdick, J. A., Injectable Granular Hydrogels with Multifunctional Properties for Biomedical Applications. *Advanced Materials* **2018,** *30* (20), 1705912.

17. Holten-Andersen, N.; Harrington, M. J.; Birkedal, H.; Lee, B. P.; Messersmith, P. B.; Lee, K. Y. C.; Waite, J. H., pH-induced metal-ligand cross-links inspired by mussel yield self-healing polymer networks with near-covalent elastic moduli. *Proceedings of the National Academy of Sciences* **2011,** *108* (7), 2651-2655.

18. Belali, S.; Karimi, A. R.; Hadizadeh, M., Cell-specific and pH-sensitive nanostructure hydrogel based on chitosan as a photosensitizer carrier for selective photodynamic therapy. *International Journal of Biological Macromolecules* **2018,** *110*, 437-448.

19. Park, D.; Wu, W.; Wang, Y., A functionalizable reverse thermal gel based on a polyurethane/PEG block copolymer. *Biomaterials* **2011,** *32* (3), 777-786.

20. Shi, L.; Ding, P.; Wang, Y.; Zhang, Y.; Ossipov, D.; Hilborn, J., Self-Healing Polymeric Hydrogel Formed by Metal–Ligand Coordination Assembly: Design, Fabrication, and Biomedical Applications. *Macromolecular Rapid Communications* **2019,** *40* (7), 1800837.

21. Appel, E. A.; del Barrio, J.; Loh, X. J.; Scherman, O. A., Supramolecular polymeric hydrogels. *Chemical Society Reviews* **2012,** *41* (18), 6195-6214.

22. Zimmerman, S. C.; Murray, T. J., Hydrogen bonded complexes with the AA·DD, AA·DDD, and AAA·DD motifs: The role of three centered (bifurcated) hydrogen bonding. *Tetrahedron Letters* **1994,** *35* (24), 4077-4080.

23. Brunsveld, L.; Folmer, B. J. B.; Meijer, E. W.; Sijbesma, R. P., Supramolecular Polymers. *Chemical Reviews* **2001,** *101* (12), 4071-4098.

24. Yount, W. C.; Loveless, D. M.; Craig, S. L., Strong Means Slow: Dynamic Contributions to the Bulk Mechanical Properties of Supramolecular Networks. *Angewandte Chemie International Edition* **2005,** *44* (18), 2746-2748.

25. Appel, E. A.; Biedermann, F.; Hoogland, D.; del Barrio, J.; Driscoll, M. D.; Hay, S.; Wales, D. J.; Scherman, O. A., Decoupled Associative and Dissociative Processes in Strong yet Highly Dynamic Host–Guest Complexes. *Journal of the American Chemical Society* **2017,** *139* (37), 12985-12993.

26. Annable, T.; Buscall, R.; Ettelaie, R.; Whittlestone, D., The rheology of solutions of associating polymers: Comparison of experimental behavior with transient network theory. *Journal of Rheology* **1993,** *37* (4), 695-726.

27. Haas, K. L.; Franz, K. J., Application of Metal Coordination Chemistry To Explore and Manipulate Cell Biology. *Chemical Reviews* **2009,** *109* (10), 4921-4960.

28. Degtyar, E.; Harrington, M. J.; Politi, Y.; Fratzl, P., The Mechanical Role of Metal Ions in Biogenic Protein-Based Materials. *Angewandte Chemie International Edition* **2014,** *53* (45), 12026-12044.

29. Dawson, J. H., Probing Structure-Function Relations in Heme-Containing Oxygenases and Peroxidases. *Science* **1988,** *240* (4851), 433-439.

30. Rising, A.; Harrington, M. J., Biological Materials Processing: Time-Tested Tricks for Sustainable Fiber Fabrication. *Chemical Reviews* **2023,** *123* (5), 2155-2199.

31. Khare, E.; Holten-Andersen, N.; Buehler, M. J., Transition-metal coordinate bonds for bioinspired macromolecules with tunable mechanical properties. *Nature Reviews Materials* **2021,** *6* (5), 421-436.

32. Degtyar, E.; Harrington, M. J.; Politi, Y.; Fratzl, P., The mechanical role of metal ions in biogenic protein-based materials. *Angew. Chem. Intl. Ed.* **2014,** *53* (45), 12026-12044.

33. Du, L.; Xu, Z.-Y.; Fan, C.-J.; Xiang, G.; Yang, K.-K.; Wang, Y.-Z., A Fascinating Metallo-Supramolecular Polymer Network with Thermal/Magnetic/Light-Responsive Shape-Memory Effects Anchored by Fe3O4 Nanoparticles. *Macromolecules* **2018,** *51* (3), 705-715.

34. Meyer, T. J., Photochemistry of metal coordination complexes: metal to ligand charge transfer excited states. *Pure and Applied Chemistry* **1986,** *58* (9), 1193-1206.

35. Dadashi, J.; Ghasemzadeh, M. A.; Salavati-Niasari, M., Recent developments in hydrogels containing copper and palladium for the catalytic reduction/degradation of organic pollutants. *RSC Advances* **2022,** *12* (36), 23481-23502.

36. Mozhdehi, D.; Neal, J. A.; Grindy, S. C.; Cordeau, Y.; Ayala, S.; Holten-Andersen, N.; Guan, Z., Tuning Dynamic Mechanical Response in Metallopolymer Networks through Simultaneous Control of Structural and Temporal Properties of the Networks. *Macromolecules* **2016,** *49* (17), 6310-6321.

37. Chen, J.; Zhao, Y., Relationship between water absorbency and reaction conditions in aqueous solution polymerization of polyacrylate superabsorbents. *Journal of Applied Polymer Science* **2000,** *75* (6), 808-814.

38. Srivastava, A.; Holten-Andersen, N.; Stucky, G. D.; Waite, J. H., Ragworm Jaw-Inspired Metal Ion Cross-Linking for Improved Mechanical Properties of Polymer Blends. *Biomacromolecules* **2008,** *9* (10), 2873-2880.

39. Guo, W.; Wang, X.; Lu, X.; Li, X.; Li, Y.; Sun, J., Plant oil and amino acid-derived elastomers with rapid room temperature self-healing ability. *Journal of Materials Chemistry A* **2019,** *7* (38), 21927-21933.

40. Fullenkamp, D. E.; He, L.; Barrett, D. G.; Burghardt, W. R.; Messersmith, P. B., Mussel-Inspired Histidine-Based Transient Network Metal Coordination Hydrogels. *Macromolecules* **2013,** *46* (3), 1167-1174.

41. Li, Q.; Barrett, D. G.; Messersmith, P. B.; Holten-Andersen, N., Controlling Hydrogel Mechanics via Bio-Inspired Polymer–Nanoparticle Bond Dynamics. *ACS Nano* **2016,** *10* (1), 1317-1324.

42. Chen, P.; Li, Q.; Grindy, S.; Holten-Andersen, N., White-Light-Emitting Lanthanide Metallogels with Tunable Luminescence and Reversible Stimuli-Responsive Properties. *Journal of the American Chemical Society* **2015,** *137* (36), 11590-11593.

43. Wang, X.; Jiang, Z.; Shi, J.; Zhang, C.; Zhang, W.; Wu, H., Dopamine-Modified Alginate Beads Reinforced by Cross-Linking via Titanium Coordination or Self-Polymerization and Its Application in Enzyme Immobilization. *Industrial & Engineering Chemistry Research* **2013,** *52* (42), 14828-14836.

44. Wang, H.; Heilshorn, S. C., Adaptable Hydrogel Networks with Reversible Linkages for Tissue Engineering. *Advanced Materials* **2015,** *27* (25), 3717-3736.

45. Holten-Andersen, N.; Jaishankar, A.; Harrington, M. J.; Fullenkamp, D. E.; DiMarco, G.; He, L.; McKinley, G. H.; Messersmith, P. B.; Lee, K. Y. C., Metal-coordination: using one of nature's tricks to control soft material mechanics. *Journal of Materials Chemistry B* **2014,** *2* (17), 2467-2472.

46. Tang, S.; Olsen, B. D., Relaxation Processes in Supramolecular Metallogels Based on Histidine–Nickel Coordination Bonds. *Macromolecules* **2016,** *49* (23), 9163-9175.

47. Lichtenegger, H. C.; Schöberl, T.; Ruokolainen, J. T.; Cross, J. O.; Heald, S. M.; Birkedal, H.; Waite, J. H.; Stucky, G. D., Zinc and mechanical prowess in the jaws of Nereis, a marine worm. *Proceedings of the National Academy of Sciences* **2003,** *100* (16), 9144-9149.

48. Birkedal , H.; Khan, R. K.; Slack , N.; Broomell, C.; Lichtenegger , H. C.; Zok, F.; Stucky , G. D.; Waite , J. H., Halogenated Veneers: Protein Cross-Linking and Halogenation in the Jaws of Nereis, a Marine Polychaete Worm. *ChemBioChem* **2006,** *7* (9), 1392-1399.

49. Harrington, M. J.; Masic, A.; Holten-Andersen, N.; Waite, J. H.; Fratzl, P., Iron-Clad Fibers: A Metal-Based Biological Strategy for Hard Flexible Coatings. *Science* **2010,** *328* (5975), 216-220.

50. Schmitt, C. N. Z.; Politi, Y.; Reinecke, A.; Harrington, M. J., Role of Sacrificial Protein–Metal Bond Exchange in Mussel Byssal Thread Self-Healing. *Biomacromolecules* **2015,** *16* (9), 2852-2861.

51. Barros, N. R.; Chen, Y.; Hosseini, V.; Wang, W.; Nasiri, R.; Mahmoodi, M.; Yalcintas, E. P.; Haghniaz, R.; Mecwan, M. M.; Karamikamkar, S.; Dai, W.; Sarabi, S. A.; Falcone, N.; Young, P.; Zhu, Y.; Sun, W.; Zhang, S.; Lee, J.; Lee, K.; Ahadian, S.; Dokmeci, M. R.; Khademhosseini,

A.; Kim, H.-J., Recent developments in mussel-inspired materials for biomedical applications. *Biomaterials Science* **2021,** *9* (20), 6653-6672.

52. Denny, M. W.; Gaylord, B., Marine Ecomechanics. *Annual Review of Marine Science* **2010,** *2* (1), 89-114.

53. Priemel, T.; Degtyar, E.; Dean, M. N.; Harrington, M. J., Rapid self-assembly of complex biomolecular architectures during mussel byssus biofabrication. *Nature Communications* **2017,** *8* (1), 14539.

54. Waite, J. H., The Formation of Mussel Byssus: Anatomy of a Natural Manufacturing Process. In *Structure, Cellular Synthesis and Assembly of Biopolymers*, Case, S. T., Ed. Springer Berlin Heidelberg: Berlin, Heidelberg, 1992; pp 27-54.

55. Bailey, A. J.; Macmillan, J.; Shrewry, P. R.; Tatham, A. S.; Gosline, J.; Lillie, M.; Carrington, E.; Guerette, P.; Ortlepp, C.; Savage, K., Elastic proteins: biological roles and mechanical properties. *Philosophical Transactions of the Royal Society of London. Series B: Biological Sciences* **2002,** *357* (1418), 121-132.

56. Schmidt, S.; Reinecke, A.; Wojcik, F.; Pussak, D.; Hartmann, L.; Harrington, M. J., Metal-Mediated Molecular Self-Healing in Histidine-Rich Mussel Peptides. *Biomacromolecules* **2014,** *15* (5), 1644-1652.

57. Lin, Q.; Gourdon, D.; Sun, C.; Holten-Andersen, N.; Anderson, T. H.; Waite, J. H.; Israelachvili, J. N., Adhesion mechanisms of the mussel foot proteins mfp-1 and mfp-3. *Proceedings of the National Academy of Sciences* **2007,** *104* (10), 3782-3786.

58. Filippidi, E.; DeMartini, D. G.; Malo de Molina, P.; Danner, E. W.; Kim, J.; Helgeson, M. E.; Waite, J. H.; Valentine, M. T., The microscopic network structure of mussel (Mytilus) adhesive plaques. *Journal of The Royal Society Interface* **2015,** *12* (113), 20150827.

59. Zechel, S.; Hager, M. D.; Priemel, T.; Harrington, M. J., Healing through Histidine: Bioinspired Pathways to Self-Healing Polymers via Imidazole–Metal Coordination. *Biomimetics* **2019,** *4* (1), 20.

60. Reinecke, A.; Brezesinski, G.; Harrington, M. J., pH-Responsive Self-Organization of Metal-Binding Protein Motifs from Biomolecular Junctions in Mussel Byssus. *Advanced Materials Interfaces* **2017,** *4* (1), 1600416.

61. Quan, W.-Y.; Hu, Z.; Liu, H.-Z.; Ouyang, Q.-Q.; Zhang, D.-Y.; Li, S.-D.; Li, P.-W.; Yang, Z.-M., Mussel-Inspired Catechol-Functionalized Hydrogels and Their Medical Applications. *Molecules* **2019,** *24* (14), 2586.

62. Krauss, S.; Metzger, T. H.; Fratzl, P.; Harrington, M. J., Self-Repair of a Biological Fiber Guided by an Ordered Elastic Framework. *Biomacromolecules* **2013,** *14* (5), 1520-1528.

63. Coyne, K. J.; Qin, X.-X.; Waite, J. H., Extensible Collagen in Mussel Byssus: A Natural Block Copolymer. *Science* **1997,** *277* (5333), 1830-1832.

64. Schmitt, C. N. Z.; Winter, A.; Bertinetti, L.; Masic, A.; Strauch, P.; Harrington, M. J., Mechanical homeostasis of a DOPA-enriched biological coating from mussels in response to metal variation. *Journal of The Royal Society Interface* **2015,** *12* (110), 20150466.

65. Jehle, F.; Macías-Sánchez, E.; Sviben, S.; Fratzl, P.; Bertinetti, L.; Harrington, M. J., Hierarchically-structured metalloprotein composite coatings biofabricated from co-existing condensed liquid phases. *Nature Communications* **2020,** *11* (1), 862.

66. Zhao, H.; Waite, J. H., Coating Proteins: Structure and Cross-Linking in fp-1 from the Green Shell Mussel Perna canaliculus. *Biochemistry* **2005,** *44* (48), 15915-15923.

67. Mesko, M.; Xiang, L.; Bohle, S.; Hwang, D. S.; Zeng, H.; Harrington, M. J., Catechol-Vanadium Binding Enhances Cross-Linking and Mechanics of a Mussel Byssus Coating Protein. *Chemistry of Materials* **2021,** *33* (16), 6530-6540.

68. Li, Y.; Cheng, J.; Delparastan, P.; Wang, H.; Sigg, S. J.; DeFrates, K. G.; Cao, Y.; Messersmith, P. B., Molecular design principles of Lysine-DOPA wet adhesion. *Nature Communications* **2020,** *11* (1), 3895.

69. Priemel, T.; Palia, R.; Babych, M.; Thibodeaux, C. J.; Bourgault, S.; Harrington, M. J., Compartmentalized processing of catechols during mussel byssus fabrication determines the destiny of DOPA. *Proceedings of the National Academy of Sciences* **2020,** *117* (14), 7613-7621.

70. Priemel, T.; Palia, G.; Förste, F.; Jehle, F.; Sviben, S.; Mantouvalou, I.; Zaslansky, P.; Bertinetti, L.; Harrington, M. J., Microfluidic-like fabrication of metal ion–cured bioadhesives by mussels. *Science* **2021,** *374* (6564), 206-211.

71. Wang, H.; Wang, L.; Zhang, S.; Zhang, W.; Li, J.; Han, Y., Mussel-inspired polymer materials derived from nonphytogenic and phytogenic catechol derivatives and their applications. *Polymer International* **2021,** *70* (9), 1209-1224.

72. Winkler, S. M.; Harrison, M. R.; Messersmith, P. B., Biomaterials in fetal surgery. *Biomaterials Science* **2019,** *7* (8), 3092-3109.

73. Shin, M.; Song, K. H.; Burrell, J. C.; Cullen, D. K.; Burdick, J. A., Injectable and Conductive Granular Hydrogels for 3D Printing and Electroactive Tissue Support. *Advanced Science* **2019,** *6* (20), 1901229.

74. Chen, Y.; Feng, X.; Zhao, Y.; Zhao, X.; Zhang, X., Mussel-Inspired Polydopamine Coating Enhances the Intracutaneous Drug Delivery from Nanostructured Lipid Carriers Dependently on a Follicular Pathway. *Molecular Pharmaceutics* **2020,** *17* (4), 1215-1225.

75. Wang, S.; Lin, J.; Wang, Z.; Zhou, Z.; Bai, R.; Lu, N.; Liu, Y.; Fu, X.; Jacobson, O.; Fan, W.; Qu, J.; Chen, S.; Wang, T.; Huang, P.; Chen, X., Core–Satellite Polydopamine–Gadolinium-Metallofullerene Nanotheranostics for Multimodal Imaging Guided Combination Cancer Therapy. *Advanced Materials* **2017,** *29* (35), 1701013.

76. Lee, H.; Lee, B. P.; Messersmith, P. B., A reversible wet/dry adhesive inspired by mussels and geckos. *Nature* **2007,** *448* (7151), 338-341.

77. Jung, H.-S.; Cho, K.-J.; Seol, Y.; Takagi, Y.; Dittmore, A.; Roche, P. A.; Neuman, K. C., Bioimaging: Polydopamine Encapsulation of Fluorescent Nanodiamonds for Biomedical Applications (Adv. Funct. Mater. 33/2018). *Advanced Functional Materials* **2018,** *28* (33), 1870234.

78. Grindy, S. C.; Learsch, R.; Mozhdehi, D.; Cheng, J.; Barrett, D. G.; Guan, Z.; Messersmith, P. B.; Holten-Andersen, N., Control of hierarchical polymer mechanics with bioinspired metal-coordination dynamics. *Nature Materials* **2015,** *14* (12), 1210-1216.

79. Degtyar, E.; Mlynarczyk, B.; Fratzl, P.; Harrington, M. J., Recombinant engineering of reversible cross-links into a resilient biopolymer. *Polymer* **2015,** *69*, 255-263.

80. Byette, F.; Laventure, A.; Marcotte, I.; Pellerin, C., Metal–Ligand Interactions and Salt Bridges as Sacrificial Bonds in Mussel Byssus-Derived Materials. *Biomacromolecules* **2016,** *17* (10), 3277-3286.

81. Mantha, S.; Pillai, S.; Khayambashi, P.; Upadhyay, A.; Zhang, Y.; Tao, O.; Pham, H. M.; Tran, S. D., Smart Hydrogels in Tissue Engineering and Regenerative Medicine. *Materials* **2019,** *12* (20), 3323.

82. Qazi, T. H.; Burdick, J. A., Granular hydrogels for endogenous tissue repair. *Biomaterials and Biosystems* **2021,** *1*, 100008.

83. Wade, R. J.; Bassin, E. J.; Rodell, C. B.; Burdick, J. A., Protease-degradable electrospun fibrous hydrogels. *Nature Communications* **2015,** *6* (1), 6639.

84. Controlling the Porosity and Microarchitecture of Hydrogels for Tissue Engineering. *Tissue Engineering Part B: Reviews* **2010,** *16* (4), 371-383.

85. Lips, P. A. M.; Velthoen, I. W.; Dijkstra, P. J.; Wessling, M.; Feijen, J., Gas foaming of segmented poly(ester amide) films. *Polymer* **2005,** *46* (22), 9396-9403.

86. Riley, L.; Schirmer, L.; Segura, T., Granular hydrogels: emergent properties of jammed hydrogel microparticles and their applications in tissue repair and regeneration. *Current Opinion in Biotechnology* **2019,** *60*, 1-8.

87. Pussak, D.; Behra, M.; Schmidt, S.; Hartmann, L., Synthesis and functionalization of poly(ethylene glycol) microparticles as soft colloidal probes for adhesion energy measurements. *Soft Matter* **2012,** *8* (5), 1664-1672.

88. Amstad, E.; Chemama, M.; Eggersdorfer, M.; Arriaga, L. R.; Brenner, M. P.; Weitz, D. A., Robust scalable high throughput production of monodisperse drops. *Lab on a Chip* **2016,** *16* (21), 4163-4172.

89. Hasan, A.; Khattab, A.; Islam, M. A.; Hweij, K. A.; Zeitouny, J.; Waters, R.; Sayegh, M.; Hossain, M. M.; Paul, A., Injectable Hydrogels for Cardiac Tissue Repair after Myocardial Infarction. *Advanced Science* **2015,** *2* (11), 1500122.

90. Nih, L. R.; Sideris, E.; Carmichael, S. T.; Segura, T., Injection of Microporous Annealing Particle (MAP) Hydrogels in the Stroke Cavity Reduces Gliosis and Inflammation and Promotes NPC Migration to the Lesion. *Advanced Materials* **2017,** *29* (32), 1606471.

91. Truong, N. F.; Kurt, E.; Tahmizyan, N.; Lesher-Pérez, S. C.; Chen, M.; Darling, N. J.; Xi, W.; Segura, T., Microporous annealed particle hydrogel stiffness, void space size, and adhesion

properties impact cell proliferation, cell spreading, and gene transfer. *Acta Biomaterialia* **2019,** *94*, 160-172.

92. Caldwell, A. S.; Campbell, G. T.; Shekiro, K. M. T.; Anseth, K. S., Clickable Microgel Scaffolds as Platforms for 3D Cell Encapsulation. *Advanced Healthcare Materials* **2017,** *6* (15), 1700254.

93. Sideris, E.; Griffin, D. R.; Ding, Y.; Li, S.; Weaver, W. M.; Di Carlo, D.; Hsiai, T.; Segura, T., Particle Hydrogels Based on Hyaluronic Acid Building Blocks. *ACS Biomaterials Science & Engineering* **2016,** *2* (11), 2034-2041.

94. Sheikhi, A.; de Rutte, J.; Haghniaz, R.; Akouissi, O.; Sohrabi, A.; Di Carlo, D.; Khademhosseini, A., Microfluidic-enabled bottom-up hydrogels from annealable naturally-derived protein microbeads. *Biomaterials* **2019,** *192*, 560-568.

95. Hsu, R.-S.; Chen, P.-Y.; Fang, J.-H.; Chen, Y.-Y.; Chang, C.-W.; Lu, Y.-J.; Hu, S.-H., Adaptable Microporous Hydrogels of Propagating NGF-Gradient by Injectable Building Blocks for Accelerated Axonal Outgrowth. *Advanced Science* **2019,** *6* (16), 1900520.

Chapter 2 : Background and Methods

2.1 Preface

In **Chapter 1**, we introduced metallosupramolecular polymeric hydrogels, delving into their design parameters, particularly focusing on how the thermodynamic and kinetic features of metal coordination influence their mechanical properties. Then, we showed how mussels employ metal coordination to impart toughness and self-healing properties to their byssi. We concluded **Chapter 1** by highlighting the potential of translating these metal coordination strategies to build high-performance soft materials such as injectable hydrogels, thermochromic films, and self-healing hydrogels.

Because certain methodologies play a pivotal role across the three data chapters in this thesis, I offer a more in-depth introduction to these techniques. **Chapter 2** introduces rheology, focusing on the theoretical basis and the main tests used in the thesis. This was followed by a brief introduction to Raman spectroscopy and the main bioconjugation techniques used in **Chapter 3** and **Chapter 5**.

2.2 Rheology: Probing Time-Dependent Properties of Soft Materials

Rheology is the study of dynamic materials' deformation and flow under shear force. By understanding how materials deform using dynamic loading, we can learn a lot about the mechanical performance of materials under various conditions. Materials typically exhibit an elastic or viscous behavior under an applied stress or strain. Viscous behavior is characterized by a fluid's tendency to flow under stress, dissipating mechanical energy (e.g. dropping a spoon into a jar of honey), while elastic behavior is characterized by a material's tendency to store mechanical energy and recover back to its original shape once a deforming force is removed (e.g., like a spring being reversibly deformed). Viscoelastic materials, such as most hydrogels and biological materials, exhibit characteristics typical of both viscous fluids and elastic solids. They can dissipate energy in viscous flow like liquids, but they are able to recover when the stress is removed like solids. However, unlike most elastic solids whose properties show minimal to no rate dependence, the mechanical response of viscoelastic materials depends strongly on the rate at which they are deformed. Hence, the mechanical properties of viscoelastic materials are measured using a machine called a rheometer, which is more sophisticated than a traditional mechanical tester.

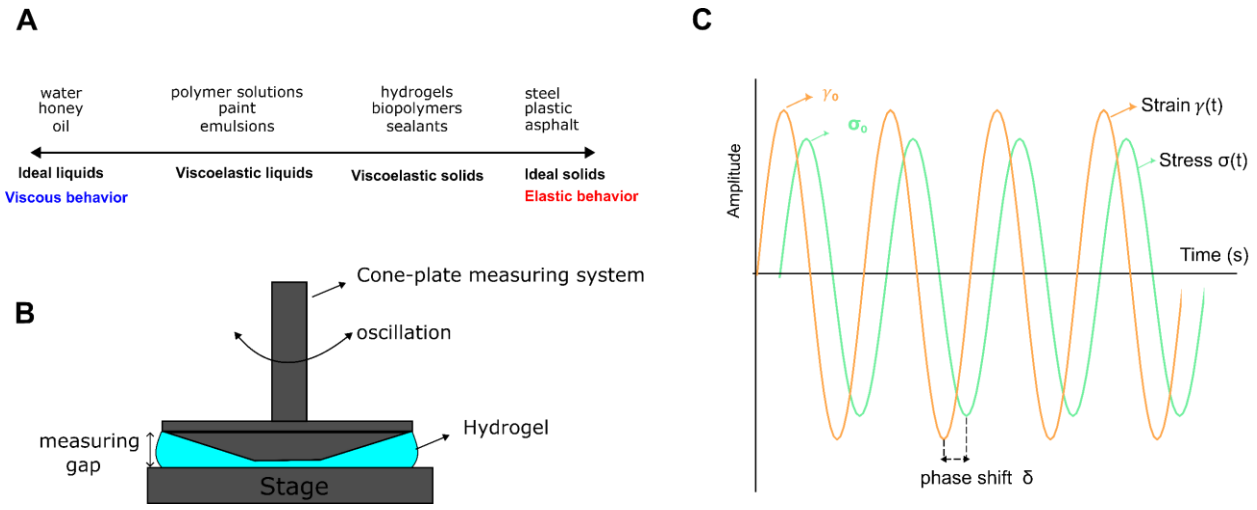

Figure 2.1: Rheological characterization of materials. (A) Rheology spectrum of materials ranging from ideal viscous fluids to ideal solids. (B) Schematic representation of a rheometer measuring a hydrogel sample in shear mode. (C) Schematic stress response to an oscillatory strain deformation to a viscoelastic material.

The viscoelastic properties of hydrogels are characterized using Rheometry, which works by applying a controlled strain (deformation of material under stress) or stress (force normalized by unit area) and measuring the resulting strain or stress over time. The gel is placed between a measuring plate which can have various geometries (Plate-plate, cone-plate, etc.) and a flat stage with a Peltier unit to control the temperature of the sample (Fig. 2.1B). Cone-plate measuring systems are more common because they typically require smaller sample sizes and allow a more uniform shear rate across the hydrogel which minimizes measurement errors.

If the rheometer is operated in strain-controlled mode, a controlled shear strain $\boldsymbol{\gamma}$ applied to the sample in a sinusoidal fashion, leads to a sinusoidal shear stress $\boldsymbol{\sigma}$ response phase shifted by the phase angle $\boldsymbol{\delta}$ (Fig. 2.1C).

$$\boldsymbol{\gamma(t) = \gamma_0 \sin(\omega t)} \quad (1)$$

$$\boldsymbol{\sigma(t) = \sigma_0 \sin(\omega t + \delta)} \quad (2)$$

The phase angle $\boldsymbol{\delta}$ decides where the material stands on the viscoelastic spectrum (Fig. 2.1A). For an ideal viscous liquid, $\boldsymbol{\delta} = 90°$, indicating that stress and the strain are completely out of phase. On the other hand, for an ideal elastic solid, the stress and strain are perfectly in phase with a phase angle $\boldsymbol{\delta} = 0°$. $\boldsymbol{\omega}$ (rad/s) is the angular frequency of the oscillation. Taking the maximum stress and strain values observed during a cycle, one can determine the complex shear modulus $G^* = \frac{\boldsymbol{\sigma(t)}}{\boldsymbol{\gamma(t)}}$. While this value effectively provides the stiffness of an elastic solid because the two maxima occur simultaneously, this value is less meaningful for viscoelastic materials in which the maxima occur out of phase. However, if we manipulate the two equations above, we can split the sinusoidal stress into two components—one in phase with the applied strain and the other fully out of phase with it. Then, one is able to define the two components of the complex modulus, G' for the in-phase part (also known as the storage modulus) and G'' for the out-of-phase part (also known as the loss modulus), such that $G^* = G' + iG''$

$$\boldsymbol{\sigma(t) = \sigma_0[\cos(\delta)\sin(\omega t) + \cos(\omega t)\sin(\omega t)]} \quad (3)$$

$$\boldsymbol{\sigma(t) = \gamma_0[G'\sin(\omega t) + G''\cos(\omega t)]} \quad (4)$$

With $\boldsymbol{G' = \frac{\sigma_0}{\gamma_0} cos\,(\delta)}$ (5) ; $\boldsymbol{G'' = \frac{\sigma_0}{\gamma_0} sin\,(\delta)}$ (6)

For a viscoelastic material, the storage modulus $\boldsymbol{G'}$ represents the more elastic solid-like aspect of a material's response to oscillatory deformation by which mechanical energy is being stored. While the loss modulus $\boldsymbol{G''}$ represents the more viscous fluid-like aspect of a material's response to oscillatory deformation by which mechanical energy is being dissipated.

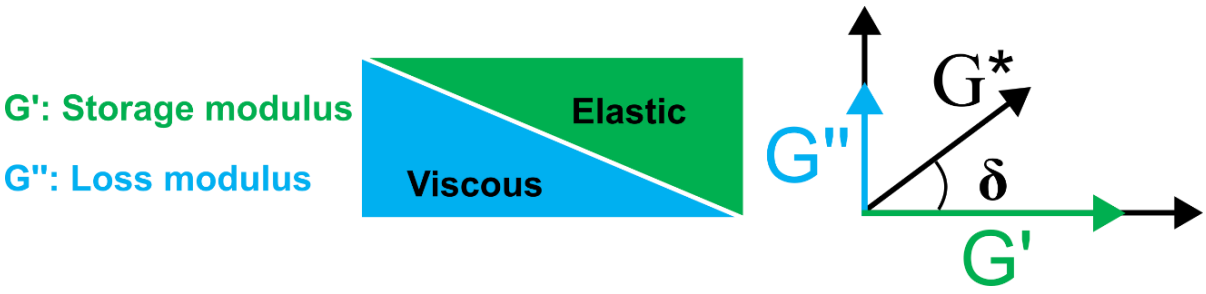

Figure 2.2: Schematic and graphical representation of the complex modulus G^*, storage modulus $\boldsymbol{G'}$, loss modulus $\boldsymbol{G''}$, and phase shift $\boldsymbol{\delta}$.

The relative magnitudes of G' and G" provide information about the relative solid-like vs. viscous-like response of a viscoelastic material. This relationship is conveniently represented by the term tan δ, which is the ratio of G" to G'. For example, if G''> G' (i.e., $\tan \boldsymbol{\delta} = \frac{G''}{G'} > 1$), the material is considered a viscoelastic liquid since the viscous portion dominates. However, If G''< G' (i.e., $\tan \boldsymbol{\delta} = \frac{G''}{G'} < 1$), the material is considered a viscoelastic solid because the elastic portion dominates in this case. Usually, the behavior of intact hydrogel networks resembles that of viscoelastic solids where $\mathbf{G'}$ is greater than $\mathbf{G''}$; however, this will be dependent on the

deformation rate at which the materials is deformed. In a crosslinked hydrogel, the storage modulus $\mathbf{G}'$ is proportional to the cross-link density d_c and can be estimated with the equation below. R is the gas constant and T is the temperature.[1]

$$\boldsymbol{G}' \approx d_c \,.R.T \qquad (7)$$

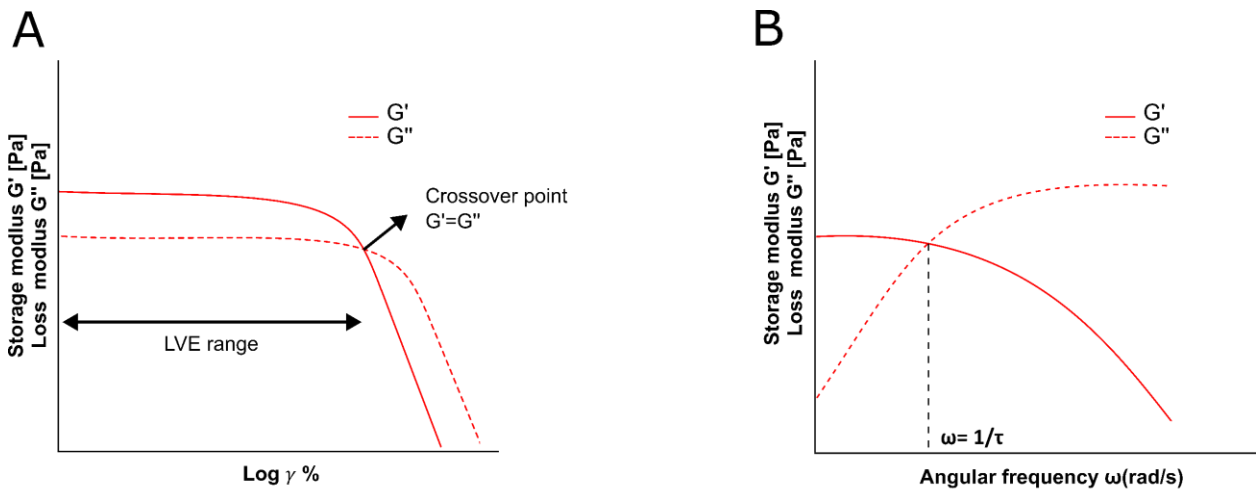

Figure 2.3: Shear rheology characterization of viscoelastic materials. (A) Amplitude sweep test to determine the linear viscoelastic regime (LVE) of the material. (B) Frequency sweep using a constant strain from the linear viscoelastic range (LVE).

To characterize the time-dependent behavior of a viscoelastic sample, we measure G' and G'' at different frequencies in the nondestructive deformation regime. Measurements at low frequencies will simulate slow motion on long time scales, while high frequencies simulate fast deformation on short timescales. It is crucial that the deformations are not destructive and done in the linear viscoelastic range (LVE range), to ensure that the measured properties are independent of the strain or stress applied during the test. As a result, prior to a frequency sweep test, the LVE range is determined using an amplitude sweep test. In this test, the storage modulus

and loss modulus are measured at a constant frequency while increasing the strain in a linear fashion as shown in Figure 2.3A. At small deformations, both moduli are constant regardless of the amount of applied strain (LVE range), but at a certain strain, the material begins to yield and reaches a crossover point, which denotes that the material's structure is breaking. After identifying the LVE range, a strain value is picked to perform the frequency sweep measurements. In the regime where G' > G'', this indicates that the material is more elastic, while at the regime where G' < G'' this shows a viscous behavior at this time scale. Physically crosslinked hydrogels, like metal crosslinked hydrogels, usually show a crossover point at which G' = G'' which can be used to calculate the approximate bond lifetime of the metal coordination bond using $\tau = \frac{1}{\omega}$ as shown in figure 2.3B.[2]

Stress Relaxation and Bond Lifetime

One very common way of characterizing viscoelastic materials is looking at their stress relaxation behavior under a constant strain. For example, if a constant strain is applied to an ideal elastic crystal (Fig.2.4A), the average atomic separation in the crystal will change which modifies the interactions between the atoms. As long as the strain is constant (and very small), the stress required to maintain will also be constant. This is due to the fact that all the energy is stored by stretching the bonds within the material and there is absence of any relaxation processes (elastic behavior). On the other hand, while stress is initially required to achieve a deformation in a fluid between two plates (Fig.2.4A), once applied no further stress is required to maintain the deformed state. This is because the mechanical energy introduced to the system has been quickly dissipated (viscous behavior) through breaking of non-covalent interactions. Thus, for an ideal

viscous fluid, relaxation is instantaneous so $\tau \approx 0$, while the time-scale of relaxation for an ideal crystal is $\tau \approx \infty$, due to the lack of relaxation modes. Viscoelastic materials exhibit a behavior somewhere in between as they possess means of dissipating mechanical energy, yet also possess physical and chemical interactions that add some resilience to the material network. Thus, measuring the time-scale of relaxation provides a means of characterizing the elastic vs. viscous behavior of viscoelastic materials.

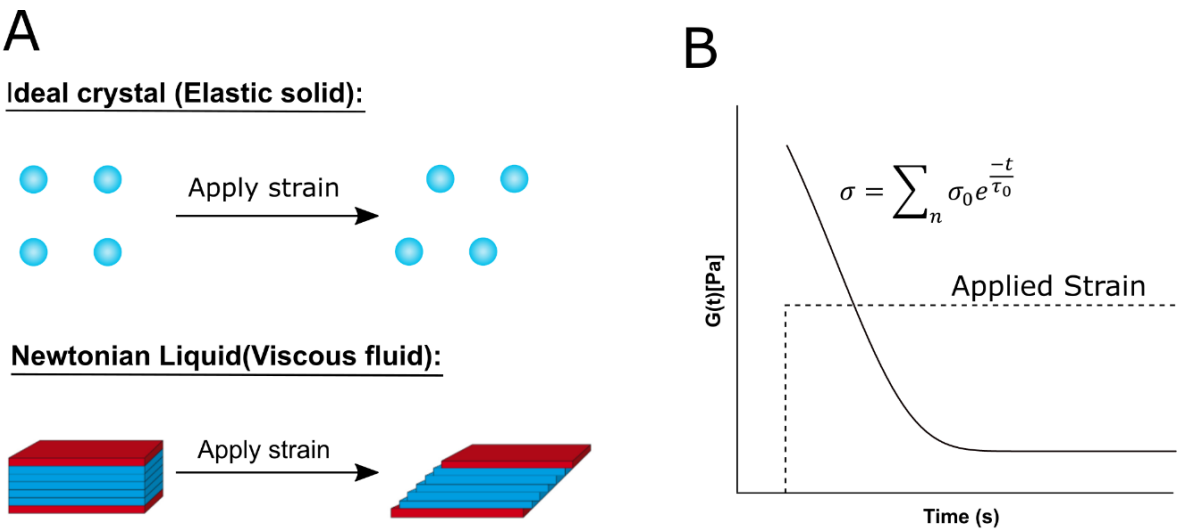

Figure 2.4: Relaxation response in viscous, elastic, and viscoelastic materials. (A) Behavior of ideal elastic solid and Newtonian fluid under applied strain. (B) Stress relaxation decay of a viscoelastic material under a constant applied strain. The relaxation time can be obtained from an exponential fit of the data.

Because viscoelastic materials exhibit elements of both elastic and viscous responses, the relaxation time is a key quantity to characterize their mechanical behavior. To measure this property, a typical stress relaxation experiment is done by applying constant strain and

measuring the decay of the stress in the material. Since the strain is constant, the relaxation modulus is proportional to the stress and can be written as:

$$\boldsymbol{G}\,(\boldsymbol{t}) = \boldsymbol{G_0}\, \boldsymbol{e}^{(-(\frac{\boldsymbol{t}}{\boldsymbol{\tau}})^{\boldsymbol{\alpha}}} \qquad (8)$$

Since the equilibrium state of the material depends on the energy states of the microscopic entities constituting it, microscopic molecular scale events decide the bulk material response to an applied strain at a given timescale. Viscoelastic materials usually exhibit multiple relaxation modes, and the viscoelastic response of a material is determined by how its molecular events react to mechanical deformation. Stress relaxation serves as a valuable tool for investigating the duration of these molecular events within physically crosslinked hydrogels, providing insights into their overall viscoelastic behavior.

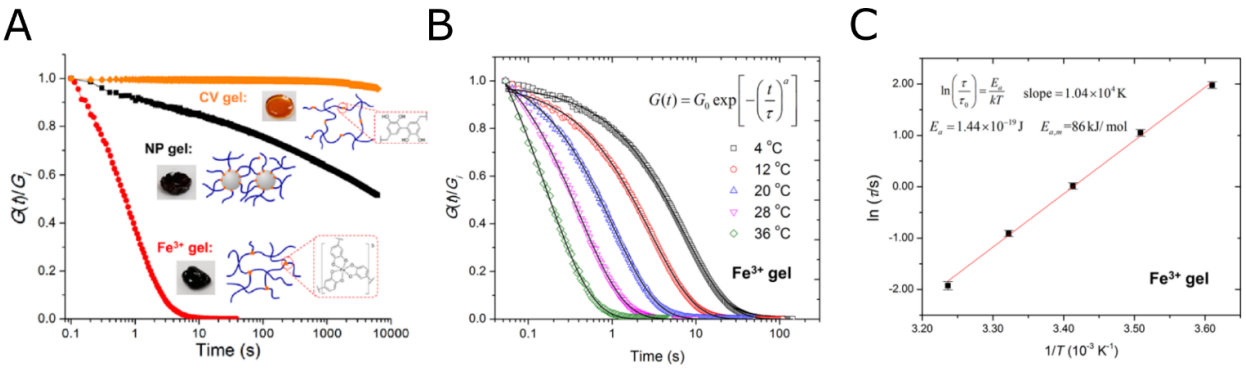

Figure 2.5: Understanding bond dynamics using stress relaxation tests at different temperatures. (A) Stress relaxation test at a constant strain (10%) for covalently crosslinked CV gel, nanoparticle-crosslinked NP gel, and iron crosslinked gel. (B) stress relaxation plots at different temperature for iron crosslinked gel. (C) Arrhenius plot for relaxation time (ln τ) vs inverse temperature (1/T). Adapted with permission from ref.[3]

For example, Figure 2.5A compares the relaxation of a covalently crosslinked hydrogel, nanoparticle crosslinked hydrogel, and metal crosslinked hydrogel. For a covalently crosslinked hydrogel, the relaxation modulus is constant due to the lack of any sacrificial bonds in the material. However, iron crosslinked gels relax quickly due to their ability to dissipate energy through the breakage and reformation of metal coordination bonds.[3] Due to the higher crosslinking density, the nanoparticles-crosslinked hydrogels exhibited a slower relaxation. If we assume that the metal dissociation is thermally activated, then we can assign an activation energy value to the metal crosslink since the relaxation time $\boldsymbol{\tau}$ follows Arrhenius's behavior.

$$\tau(T) = \tau_0 \, e^{\frac{E_a}{kT}} \quad (9)$$

where τ is the characteristic time scale, k is Boltzmann constant, and E_a is the activation energy. To obtain the activation energy value, stress relaxation studies can be performed at different temperatures (Fig.2.5B), then the relaxation time is plotted versus inverse temperature, and the activation energy is extracted from the slope of the fitted curve (Fig.2.5C). This approach highlights the capability of rheology in unraveling the intricate molecular processes at the microscopic level that underlie the macroscopic response of bulk materials to deformation.

2.3 Constitutive Models for Viscoelastic Materials: Maxwell Model

It is common to reduce the dimensionality of the material functions by fitting the experimental data from mechanical experiments on viscoelastic materials to a *constitutive model*. [4]

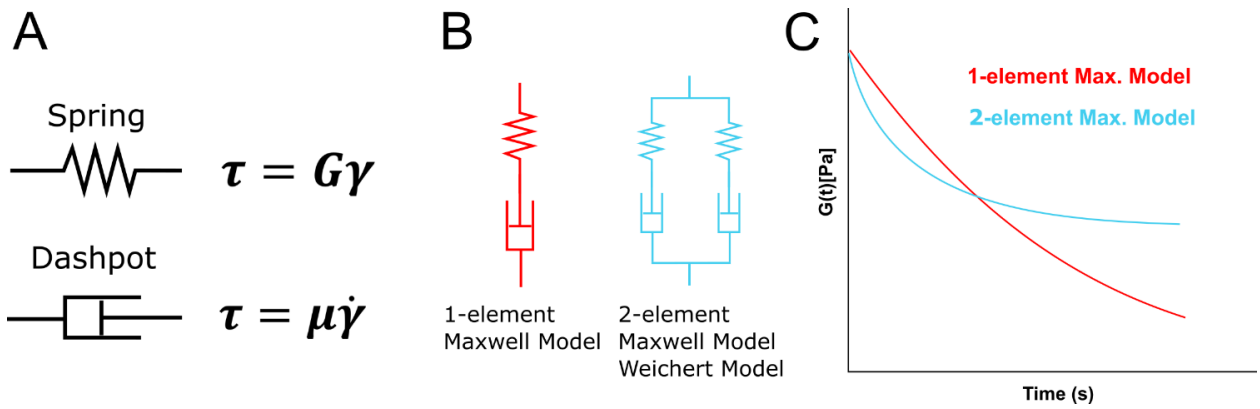

Figure 2.6: Maxwell model for viscoelastic materials. (A) Mechanical analogs representing Hookean solids (spring) and ideal fluids (dashpot). (B) Viscoelastic materials with one relaxation mode can be represented with Maxwell model with a spring and a dashpot in series, while materials with two relaxation modes can be represented with 2 Maxwell models in parallel. (C) stress relaxation showing a monoexponential decay for materials with one relaxation mode and biexponential decay for materials having two relaxation mode.

Constitutive models are, in a nutshell, the relationships between the stress and strain of a material and their time derivatives. For ideal solid materials, for instance, the constitutive model is a Hookean-like ($F = K\Delta L$) linear proportionality between stress and strain ($\sigma = G\gamma$). While in a Newtonian fluid the proportionality is between stress and strain rate (Fig. 2.6A) For a viscoelastic material, Maxwell model combines viscous and elastic responses phenomenologically. Mechanical analogs can be useful to describe viscoelastic models – they serve as a representation of how the viscous and elastic response are combined in a given model. A dashpot represents the viscous response, while a spring represents the elastic response. For example, a simple one-element maxwell model where the material exhibits one molecular relaxation event contains a dashpot and spring in series (Fig. 2.6B). However, more complex

linear viscoelastic materials with multiple relaxation pathways underlying their stress relaxation behavior, can be modeled using Maxwell-Weichert model. This model consists of n Maxwell models in parallel and represented using the equation below. For example, if the relaxation data fits to a biexponential decay, we can model the material using Maxwell-Weichert model with 2 Maxwell models in parallel (n=2).

$$\boldsymbol{\sigma(t)} = \sum_{\boldsymbol{n}} \boldsymbol{\sigma_n}\ \boldsymbol{e}^{(-(\frac{\boldsymbol{t}}{\boldsymbol{\tau}})^{\boldsymbol{\alpha}}} \qquad (10)$$

It is important to mention that relaxation modes are time-dependent where some of them will only show up at specific timescales.

2.4 Raman Spectroscopy: Characterization of Metal-Coordinate Bonds

Raman spectroscopy is a powerful vibrational spectroscopy technique that can be used to characterize the structure of biomolecules like proteins and peptides.[5] One major distinction between Raman and FTIR spectroscopy lies in the use of a single frequency laser source rather than a range of wavelengths. In Raman spectroscopy, the sample is illuminated with an intense monochromatic laser and the inelastically scattered light is analyzed by a CCD camera, recording intensity of scattered light as a function of Raman shift (i.e., change in energy relative to the incident laser source displayed in wavenumbers typically). Obtained Raman spectra provide a fingerprint that represents the set of chemical bonds in the material.[6]

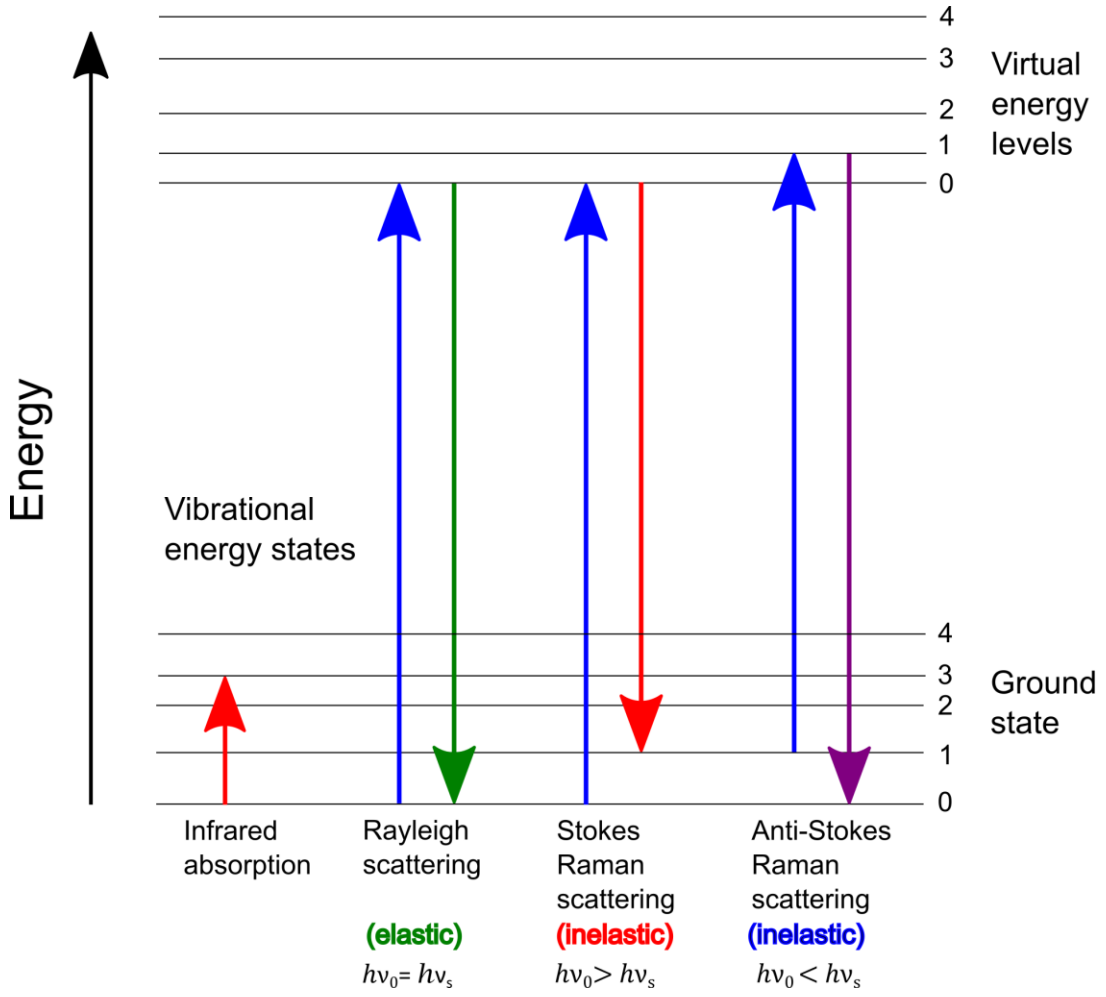

Figure 2.7 : Raman scattering and infrared absorption phenomena.

When an incident light is directed onto a sample, this light can be reflected, absorbed, or scattered depending on the different factors like the angle of incidence and wavelength of light. In terms of scattering, photons can be scattered elastically or inelastically, which is visualized in the Jablonski plot in Figure 2.7. In elastic scattering (also known as Rayleigh scattering), the wavelength of the scattered photon is equal to that of the incident light ($h\nu_0 = h\nu_s$, where h represents the Planck's constant, v is the frequency of the light). In a Raman spectrum, this is the strong peak occurring at 0 cm^{-1}. Inelastic scattering can be divided into Stokes and Anti-Stokes

scattering, and this effect provides the Raman peaks that give information on vibrational modes present in a sample. During inelastic Stokes Raman scattering, a photon loses energy when interacting with a molecular bond, such that the frequency of the scattered light is decreased relative to the incidence light ($h\nu_0 > h\nu_s$). This occurs when a molecular vibration in its ground state is excited into a virtual state by the incident photon, before relaxing to an excited energy state with the energy difference between the ground and excited energy states equal to the energy lost by the Stokes scattered photon. In a Raman spectrum this change in energy would be observed as a peak appearing at a Raman shift equal to the energy loss. In the less common Anti-Stokes scattering, the energy of the scattered light is higher than the incident laser light since in this case, the photon is interacting with a molecule already in an excited state bringing it to a virtual state before returning to the lower energy ground state. In general, Raman spectroscopy examines inelastic scattered light to acquire information about the chemical structure, conformation, and orientation of molecules in different materials.

Raman Analysis on Proteins and Peptides: DOPA and Histidine

Raman spectroscopy is a potent technique to characterize proteins due to the fact that the backbone of the polypeptides with distinct peak position associated with different secondary structures and also that many side chain residues are Raman active. For example, the Amide I vibration (1634-1676 cm^{-1}) which arises from the stretching of the carbonyl peak along with the Amide III vibration originating from a combination of C-N stretching, and N-H bending can give valuable information about the secondary structure of proteins or peptides.[7] For instance, β-

sheet structures display a strong Amide I vibration between 1662 -1670 cm^{-1}.[8] However, for α-helical proteins or peptides, Amide I peak will appear as a peak between 1645-1658 cm^{-1} and an Amide III peak between 1280-1320 cm^{-1}.[9, 10] Moreover, Raman spectroscopy can give characteristic peaks for various side chain residues like histidine, tyrosine and DOPA in their free and metal-bound states.

Raman Structural Markers of Histidine Side Chains:[11]

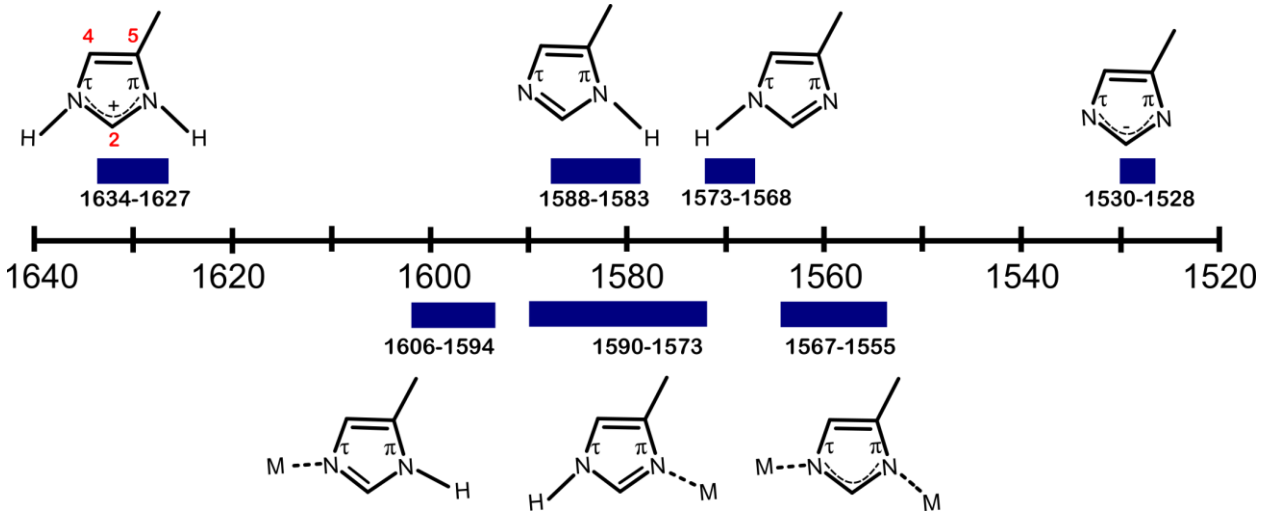

Figure 2.8: Characteristic imidazole ring vibrations of histidine in various protonation and coordination states. Adapted with minor changes from ref.[11]

The amino acid histidine is Raman active and very useful for differentiating the different states of the side chain.[12] For example, Raman peaks in the region between 1520-1640 cm^{-1} can distinguish between different protonation and metal coordination states of the imidazole ring.[11] In this region, the peaks arise from the stretching vibration of the C_4=C_5 double bond which shifts according to the protonation and metal coordination state of the imidazole ring. When the pH<6.5 (pKa of imidazole) both Nτ and Nπ will be protonated which yields a peak between 1627-

1634 cm^{-1}). In the neutral state, histidine can tautomerize into a state where the hydrogen is bound to Nτ (1568-1573 cm^{-1}) or bound to Nπ closer to the CH_2 group (1583-1588 cm^{-1}). Under neutral to basic conditions, free nitrogens can bind different divalent cations like $Ni^{2+,}$ Cu^{2+}, Co^{2+} and Zn^{2+}, and each one can shift the peak position by a certain degree. When the metal ion binds to Nτ atom this leads to a peak at 1594-1606 cm^{-1}, while binding to Nπ gives rise to a peak between 1573-1588 cm^{-1}. At extremely basic conditions (pH=14), both nitrogens become deprotonated forming an imidazolate ion (1528-1530 cm^{-1}). This knowledge was crucial to understand the structural organization of different proteins and track histidine metal coordination in the mussel byssus.

DOPA- Metal Coordination:

Raman spectroscopy has also been extensively used to characterize interactions between DOPA and metal ions in natural and synthetic catechol-containing materials.[13, 14] In the free state, DOPA only shows phenyl ring vibrations in the region between 1250 and 1500 cm^{-1} which can overlap with a lot of other vibrations.[3] However, when bound to metals like iron as shown in the figure below, Raman spectroscopy gives a signature set of peaks for the different metal coordination states that exist at different pH values (mono (pH=5), bis (pH=8), or tris (pH=12)).[15] These peaks are resonance-enhanced depending on the wavelength of the incident laser, providing very strong peaks specific and distinctive for the metal coordination bonds. In the metal-free state, no peaks are observed in the region between 400-650 cm^{-1}. However, upon the addition of Fe^{3+}, three peaks arise between 470-670 cm^{-1} due to the chelation of iron metals by

the oxygen atoms on the dopamine. The shape and the intensity of these peaks can distinguish between the coordination states of iron and DOPA.[16]

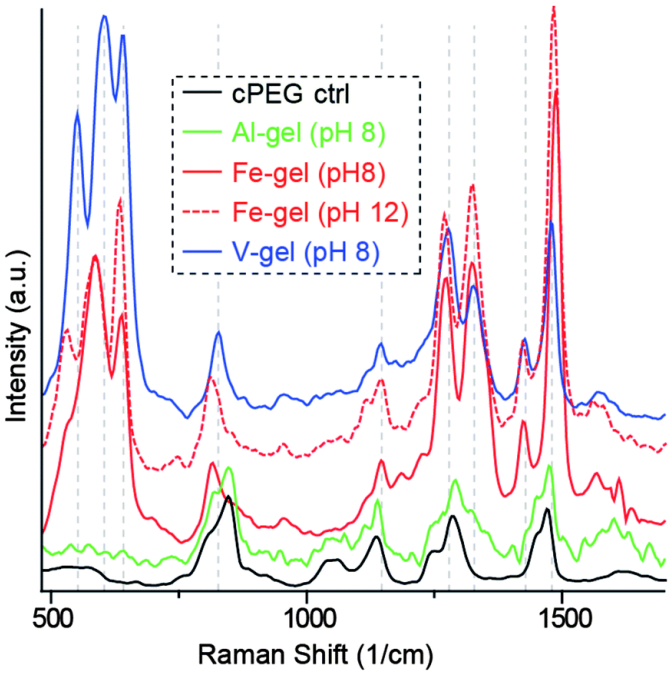

Figure 2.9: Signature Raman peaks of DOPA-metal coordination bonds. Adapted with permission from ref.[16]

2.5 Bioconjugation Toolbox

Bioconjugation is the process of connecting a biological moiety (e.g., peptide) to another substrate.[17] These substrates can be a synthetic polymer like polyacrylamide or polyethylene glycol, fluorescent dye, nanoparticles, drugs, or another biomolecule. This technique is crucial in many fields including drug delivery[18], bioimaging[19] , and medical diagnostics[20]. Throughout the years, scientists have developed an extensive range of reactions that can be utilized for each

specific type of bioconjugation. One of the most widely used bioconjugation reactions to form an amide linkage between a carboxylic acid and a primary amine is carbodiimide conjugation or EDC/NHS chemistry.

2.5.1 Carbodiimide Crosslinker Chemistry EDC/NHS

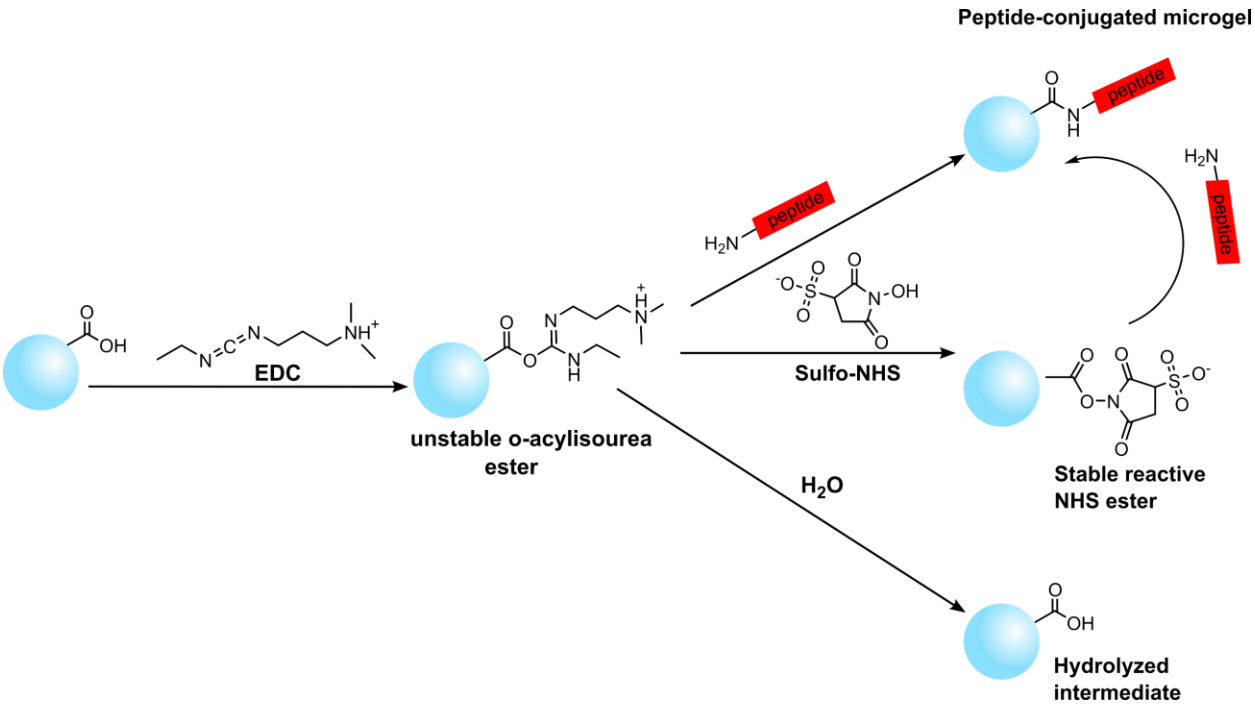

Figure 2.10: Schematic representation of different reaction pathways for EDC/NHS coupling of a peptide to a carboxylated particle.

As shown in the figure above, EDC (1-ethyl-3-(3-dimethylaminopropyl) carbodiimide) acts as a coupling agent and reacts with the carboxylic acid group to get an unstable activated o-acylisourea ester which can react with a primary amine (peptide's N-terminus) to form a stable amide linkage. However, this intermediate is not very stable in water, as it can be hydrolyzed back to the carboxylic acid form. To address this challenge, Sulfo-NHS (N-

hydroxysulfosuccinimide) can improve the efficiency of the coupling by reacting with o-acylisourea ester to form a more stable intermediate which can react with the amine to form a stable amide bond increasing the specificity and the yield of the coupling. The main enemy to this reaction is hydrolysis. This necessitates the use of excess coupling reagents and optimizing the different factors in the reaction like the choice of buffer, temperature, and pH. The optimal pH for the carboxylic acid activation is between 4.5-5[21] , while the coupling the pH should be raised above 7, but not much higher to avoid the hydrolysis of the intermediate. Finally, to avoid side reaction primary amines and carboxylic acids from the buffers and phosphate salts should be excluded to avoid any side reactions. EDC/NHS chemistry cannot be used to link all types of peptides or proteins. For example, coupling peptides containing lysine residues will lead to amide linkage with the amino group at the N-terminus and with the side chains of lysine residues. To solve this problem thiol/maleimide (Michael addition) can avoid this type of side reaction.

2.5.2 Thiol-Maleimide Coupling Chemistry

Thiol-maleimide coupling is a 1,4 Michael addition reaction between the thiol group and an α,β-unsaturated maleimide ring to form an irreversible stable thioester linkage.

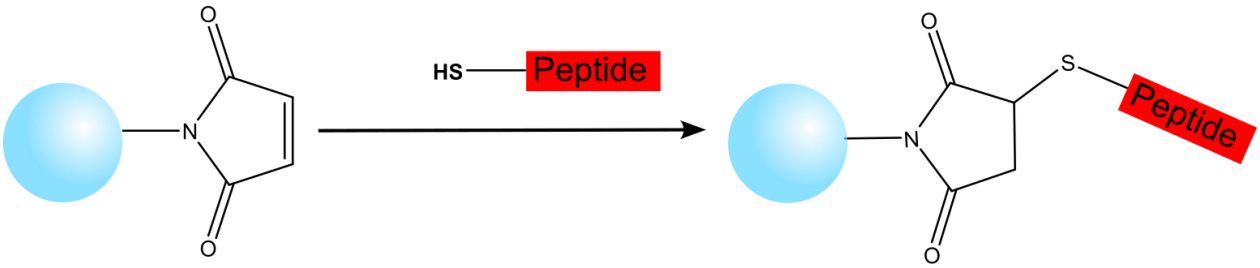

Figure 2.11: Schematic representation of thiol-maleimide coupling.

The advantage of this reaction is that it is rapid, and it is effective at physiologically relevant pHs 6.5-7.5.[22] However, in more basic environment (pH> 8.5) , maleimide can react with primary amines as a side reaction. As a result, it is important to keep the pH below 7.5 where thiol-maleimide reaction dominates. It should be noted, that hydrolysis also affects this Michael addition reaction with a rate that increases with pH and temperature as noted in the study done by Kirchoff.[23] For the scope of this thesis, in lysine containing peptides, cysteine was added at the N-terminus and the thiol side chain is allowed to react with the maleimide group on the other moieties. TCEP (Tris (2 carboxyethyl)phosphine hydrochloride) is usually added to the peptide prior to the coupling to break the disulfide bridging between the peptides.

2.6 References

1. Hajighasem, A.; Kabiri, K., Cationic highly alcohol-swellable gels: synthesis and characterization. *Journal of Polymer Research* **2013,** *20* (8), 218.

2. Tang, S.; Olsen, B. D., Relaxation Processes in Supramolecular Metallogels Based on Histidine–Nickel Coordination Bonds. *Macromolecules* **2016,** *49* (23), 9163-9175.

3. Li, Q.; Barrett, D. G.; Messersmith, P. B.; Holten-Andersen, N., Controlling Hydrogel Mechanics via Bio-Inspired Polymer–Nanoparticle Bond Dynamics. *ACS Nano* **2016,** *10* (1), 1317-1324.

4. Zhou, X.; Yu, D.; Barrera, O., Chapter Three - Mechanics constitutive models for viscoelastic solid materials: Development and a critical review. In *Advances in Applied Mechanics*, Bordas, S. P. A., Ed. Elsevier: 2023; Vol. 56, pp 189-321.

5. Benevides, J. M.; Overman, S. A.; Thomas Jr., G. J., Raman Spectroscopy of Proteins. *Current Protocols in Protein Science* **2003,** *33* (1), 17.8.1-17.8.35.

6. Larkin, P., Chapter 1 - Introduction: Infrared and Raman Spectroscopy. In *Infrared and Raman Spectroscopy*, Larkin, P., Ed. Elsevier: Oxford, 2011; pp 1-5.

7. Movasaghi, Z.; Rehman, S.; Rehman, I. U., Raman Spectroscopy of Biological Tissues. *Applied Spectroscopy Reviews* **2007,** *42* (5), 493-541.

8. Sadat, A.; Joye, I. J., Peak Fitting Applied to Fourier Transform Infrared and Raman Spectroscopic Analysis of Proteins. *Applied Sciences* **2020,** *10* (17), 5918.

9. Paquin, R.; Colomban, P., Nanomechanics of single keratin fibres: A Raman study of the α-helix →β-sheet transition and the effect of water. *Journal of Raman Spectroscopy* **2007,** *38* (5), 504-514.

10. Mikhonin, A. V.; Ahmed, Z.; Ianoul, A.; Asher, S. A., Assignments and Conformational Dependencies of the Amide III Peptide Backbone UV Resonance Raman Bands. *The Journal of Physical Chemistry B* **2004,** *108* (49), 19020-19028.

11. Takeuchi, H., Raman structural markers of tryptophan and histidine side chains in proteins. *Biopolymers* **2003,** *72* (5), 305-317.

12. Zhu, G.; Zhu, X.; Fan, Q.; Wan, X., Raman spectra of amino acids and their aqueous solutions. *Spectrochimica Acta Part A: Molecular and Biomolecular Spectroscopy* **2011,** *78* (3), 1187-1195.

13. Harrington, M. J.; Masic, A.; Holten-Andersen, N.; Waite, J. H.; Fratzl, P., Iron-Clad Fibers: A Metal-Based Biological Strategy for Hard Flexible Coatings. *Science* **2010,** *328* (5975), 216-220.

14. Priemel, T.; Palia, G.; Förste, F.; Jehle, F.; Sviben, S.; Mantouvalou, I.; Zaslansky, P.; Bertinetti, L.; Harrington, M. J., Microfluidic-like fabrication of metal ion–cured bioadhesives by mussels. *Science* **2021,** *374* (6564), 206-211.

15. Holten-Andersen, N.; Harrington, M. J.; Birkedal, H.; Lee, B. P.; Messersmith, P. B.; Lee, K. Y. C.; Waite, J. H., pH-induced metal-ligand cross-links inspired by mussel yield self-healing polymer networks with near-covalent elastic moduli. *Proceedings of the National Academy of Sciences* **2011,** *108* (7), 2651-2655.

16. Holten-Andersen, N.; Jaishankar, A.; Harrington, M. J.; Fullenkamp, D. E.; DiMarco, G.; He, L.; McKinley, G. H.; Messersmith, P. B.; Lee, K. Y. C., Metal-coordination: using one of nature's tricks to control soft material mechanics. *Journal of Materials Chemistry B* **2014,** *2* (17), 2467-2472.

17. Koniev, O.; Wagner, A., Developments and recent advancements in the field of endogenous amino acid selective bond forming reactions for bioconjugation. *Chemical Society Reviews* **2015,** *44* (15), 5495-5551.

18. Lieser, R. M.; Yur, D.; Sullivan, M. O.; Chen, W., Site-Specific Bioconjugation Approaches for Enhanced Delivery of Protein Therapeutics and Protein Drug Carriers. *Bioconjugate Chemistry* **2020,** *31* (10), 2272-2282.

19. Govindaraju, S.; Rengaraj, A.; Arivazhagan, R.; Huh, Y.-S.; Yun, K., Curcumin-Conjugated Gold Clusters for Bioimaging and Anticancer Applications. *Bioconjugate Chemistry* **2018,** *29* (2), 363-370.

20. Ryzhov, I. M.; Tuzikov, A. B.; Nizovtsev, A. V.; Baidakova, L. K.; Galanina, O. E.; Shilova, N. V.; Ziganshina, M. M.; Dolgushina, N. V.; Bayramova, G. R.; Sukhikh, G. T.; Williams, E. C.; Nagappan, R.; Henry, S. M.; Bovin, N. V., SARS-CoV-2 Peptide Bioconjugates Designed for Antibody Diagnostics. *Bioconjugate Chemistry* **2021,** *32* (8), 1606-1616.

21. Vashist, S. K., Comparison of 1-Ethyl-3-(3-Dimethylaminopropyl) Carbodiimide Based Strategies to Crosslink Antibodies on Amine-Functionalized Platforms for Immunodiagnostic Applications. *Diagnostics* **2012,** *2* (3), 23-33.

22. Ghosh, S. S.; Kao, P. M.; McCue, A. W.; Chappelle, H. L., Use of maleimide-thiol coupling chemistry for efficient syntheses of oligonucleotide-enzyme conjugate hybridization probes. *Bioconjugate Chemistry* **1990,** *1* (1), 71-76.

23. Kirchhof, S.; Strasser, A.; Wittmann, H.-J.; Messmann, V.; Hammer, N.; Goepferich, A. M.; Brandl, F. P., New insights into the cross-linking and degradation mechanism of Diels–Alder hydrogels. *Journal of Materials Chemistry B* **2015,** *3* (3), 449-457.

Chapter 3 : pH-Responsive Reversible Granular Hydrogels Based on Metal-Binding Mussel-Inspired Peptides

3.1 Preface

In **Chapter 1**, we introduced the potential of granular hydrogels as injectable scaffolds for various biomedical applications and highlighted their limitations in dynamic tissues. Next, we demonstrated how mussels use metal coordination to impart toughness and stiffness to their byssi. **Chapter 2** introduced the main characterization techniques used in the data chapters such as rheology, Raman spectroscopy, and bioconjugation techniques. In **Chapter 3**, we drew inspiration from zinc-histidine coordination in the byssus core to design an injectable hydrogel that can be annealed into a tough, porous, and biocompatible scaffold under physiological conditions in the presence of zinc.

Chapter 3 was adapted with permission from: **Rammal, M.; Li, C.; Reeves, J.; Moraes, C.; Harrington, M. J., pH-Responsive Reversible Granular Hydrogels Based on Metal-Binding Mussel-Inspired Peptides. ACS Applied Materials & Interfaces 2023, 15 (24), 29004-29011**.

3.2 Abstract

Taking advantage of their thixotropic behavior, microporosity, and modular properties, granular hydrogels formed from jammed hydrogel microparticles have emerged as an exciting class of soft, injectable materials useful for numerous applications, ranging from the production of biomedical scaffolds for tissue repair to the therapeutic delivery of drugs and cells. Recently, the annealing of hydrogel microparticles *in situ* to yield a porous bulk scaffold has shown numerous benefits in regenerative medicine, including tissue-repair applications. Current annealing techniques, however, mainly rely either on covalent connections, which produce static scaffolds, or transient supramolecular interactions, which produce dynamic but mechanically weak hydrogels. To address these limitations, we developed microgels functionalized with peptides inspired by the histidine-rich cross-linking domains of marine mussel byssus proteins. Functionalized microgels can reversibly aggregate *in situ* via metal coordination cross-linking to form microporous, self-healing, and resilient scaffolds at physiological conditions by inclusion of minimal amounts of zinc ions at basic pH. Aggregated granular hydrogels can subsequently be dissociated in the presence of a metal chelator or under acidic conditions. Based on the demonstrated cytocompatibility of these annealed granular hydrogel scaffolds, we believe that these materials could be developed toward applications in regenerative medicine and tissue engineering.

3.3 Introduction

Injectable granular hydrogels, made from spherical micrometer-sized hydrogel particles, have found significant use in many biomedical applications, including tissue repair and regeneration, local therapeutic delivery of cells/drugs, tissue engineering, and bioprinting.[2-6] Above a certain packing density, hydrogel microparticles (HMPs) jam together to form a dynamic granular scaffold that exhibits unique physical properties such as injectability, porosity, and self-healing. Although these granular systems behave more like a bulk gel at low strain, they flow like a liquid at high strains due to the weak interactions holding them together.[7] This presents some challenges if they are injected into mechanically dynamic tissues like cardiac tissues or vocal folds due to the high strains that the gels experience.[8, 9]

To improve the mechanical properties of such scaffolds and to avoid particle dislodgment in motile tissue settings, hydrogel microparticles can be interconnected using different types of interactions (covalent, physical, hydrophobic, or electrostatic) to form microporous annealed particle (MAP) scaffolds.[10-12] Material degradation kinetics can also be modified by HMP annealing, which introduces a configurable degradation parameter to the material[7]. Current research has focused on employing annealing as a parameter to create stimuli-responsive MAP scaffolds that form under physiological conditions and exhibit controlled degradation behavior. Presently these annealing chemistries largely rely on covalent crosslinking achieved by click chemistry,[13] carbodiimide chemistry,[14] and light-mediated radical reactions[15], which yields mechanically stable, stiff scaffolds. However, due to the covalent nature of interparticle cross-linking, these scaffolds lack both shear-thinning and self-healing properties, which limits their practical application.[14] On the other hand, physically crosslinked granular systems based on

electrostatic interactions[16] or host-guest interactions[17] exhibit viscoelastic properties and thixotropic behavior upon injection, but they are significantly less mechanically robust than covalently crosslinked scaffolds.

We posit that metal coordination cross-linking might offer the best of both worlds by combining the dynamic and self-healing properties of host-guest interactions while maintaining a bond strength approaching that of covalent bonds.[18, 19] However, this dynamic chemistry has not yet been exploited for annealing granular hydrogels, but could offer important advantages, especially due to the pH-sensitivity and reversibility of such interactions. In particular, histidine-metal coordination is an excellent candidate for cross-linking MAPs since the pK_a of the imidazole side chain (~6.5) is close to the physiological pH, enabling the rapid formation of metal crosslinks upon injection into the body. [20, 21]

Due to their high binding affinities and rates of formation, metal coordination-based crosslinks have been shown to endow both biological and synthetic materials with certain desirable properties including triggered self-assembly[22], increased toughness,[23] and adhesion.[24] In nature, marine mussels are well-known for using metal coordination cross-linking to mechanically reinforce their protein-based byssal thread fibers (Fig. 3.1).[25-29] These fibers allow mussels to cling to surfaces on rocky seashores and endure high intertidal zones owing to their exceptional toughness and intrinsic self-healing ability. The core of the byssal thread is composed of collagenous proteins, known preCols, which are organized in a hierarchical semicrystalline arrangement (Fig. 3.1B-D).[30-32] PreCols are natural block copolymers with a collagen core flanked by two histidine-rich domains (HRDs) at both ends (Fig. 3.1C).[31, 33] Prior to thread formation, PreCols are stored closely packed within a smectic liquid crystalline phase inside vesicles under

low pH conditions (Fig. 3.1D).[29, 34] During thread formation, PreCols are secreted into seawater (pH~8.1) in the presence of metal ions, at which point the liquid crystalline phase solidifies into stiff, tough and self-healing semicrystalline fibers (Fig. 3.1D-E).[29]

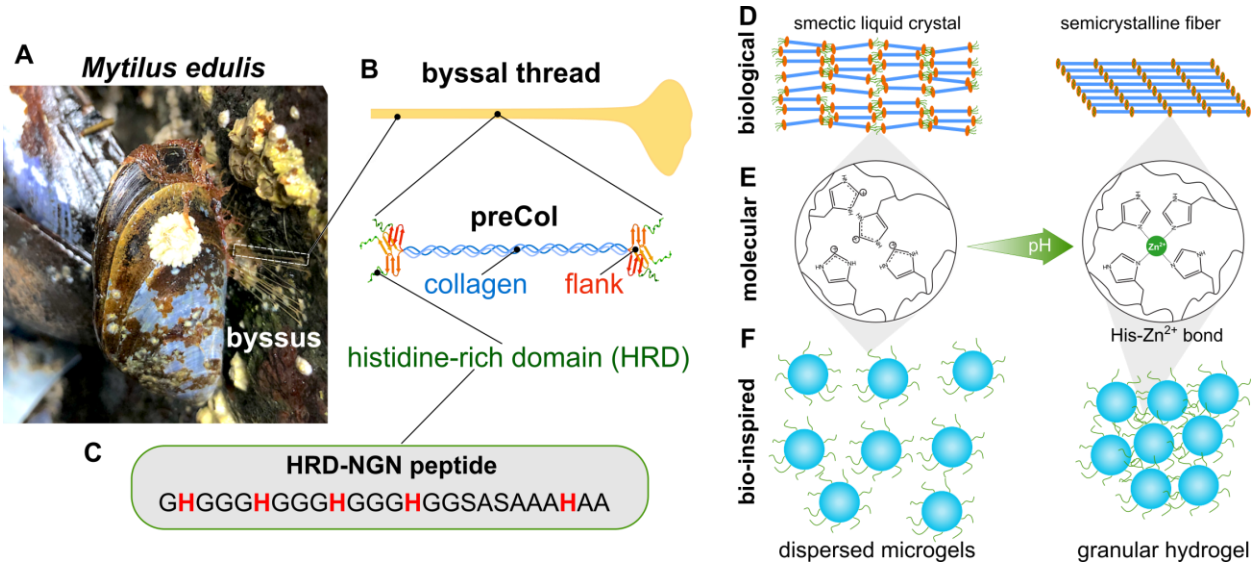

Figure 3.1: Hydrogel microparticle annealing inspired by mussel byssus self-assembly. (A) Marine mussels (*Mytilus edulis*) use high-performance protein-based tough fibers to anchor themselves to rocks under extreme conditions. (B) The distal region of the mussel byssus consists of a large central collagen domain (~130 nm) terminated on both sides by two flanking histidine-rich domains (HRDs). Due to the pH-responsiveness of histidine and its ability to form strong and reversible coordination bonds with metal ions such as Zn^{2+} and Ni^{2+}, these domains play a key role in the self-assembly, toughness and self-healing of the byssus. (C) Synthetic peptide sequence based on the histidine-rich domain of PreCol proteins. (D) Schematic illustration of the proposed mechanism PreCols self-assembly into semicrystalline fibers. At low pH, preCol are closely packed in a liquid crystalline phase inside the vesicles under acidic conditions. Upon secretion to a basic pH in the presence of metal ions, PreCols assemble into semicrystalline fibers aided by histidine-metal coordination cross-links. (E, F) Hydrogel microparticles functionalized with synthetic peptides based on the HRD of PreCol proteins can mimic the byssus formation process through reversible zinc-histidine coordination.

Several studies have shown that HRDs play a critical role in controlling the mechanical response of byssal threads, but also in guiding their assembly in a pH-dependent manner. Spectroscopic and X-ray diffraction techniques combined with mechanical testing *in situ* have revealed that this is accomplished through specific interactions of HRD histidine residues with transition metal ions (such as Zn^{2+} and Cu^{2+}), which results in the formation of a network of metal coordination cross-links that is mechanically robust (Fig. 3.1E).[30, 35, 36] These coordination bonds impart toughness in the threads by sacrificially rupturing under high stress, preventing irreversible breakage of the covalent bonds.[36] Moreover, the native mechanical properties of the threads are recovered upon the reformation of the metal coordination bonds, providing a robust self-healing response.[20] These findings have inspired researchers to use histidine-metal transient interactions to enhance the mechanical properties of polymeric materials functionalized with imidazole groups and to fine-tune their viscoelastic properties.[20, 21, 37] In addition, peptide-polymer hybrids were made using peptides based on preCol HRD sequences to fabricate soft colloidal probes for adhesion studies,[38, 39] pH-responsive hydrogels,[40] and peptide films.[41]

This study presents an approach for assembling reversible MAP scaffolds using HRD peptide-functionalized PEG microgels that can form under physiological conditions (Fig. 3.1F). Analogous to how preCol proteins self-assemble into high-performance fibers when released into seawater, the peptide-functionalized microgels can create a porous scaffold when injected into physiological media in the presence of Zn^{2+} ions – yet assembly is reversible given the transient and stimuli-responsive nature of the His-Zn^{2+} bonds. Microgels were synthesized in a high-salt solution using the colloidal suspension method without the use of any surfactant (Fig. 3.2A).

Carboxylic acid moieties were then grafted onto the PEG backbone, followed by the coupling of the mussel-inspired HRD peptide to the hydrogel microparticles (Fig. 3.2B). As demonstration of potential biomedical application, microgels were loaded into a syringe under slightly acidic conditions in the presence of $ZnCl_2$, and upon injection into physiological conditions, they formed a strongly linked MAP scaffold that could be subsequently dispersed by chelating zinc ions or lowering the pH. Finally, we demonstrate that these crosslinked porous scaffolds provide a cytocompatible microenvironment providing a proof-of-concept for potential tissue engineering applications.

3.4 Chemicals and Methods

3.4.1 Chemicals

All solvents and reagents were used without further purification. PEG-diacrylamide (8000 g/mol) was purchased from Biopharma PEG Scientific, Inc. HRD-NGN (sequence = N-GHGGGHGGGHGGGHGGSASAAAHAAG-$CONH_2$) and RGD (sequence = N-GRGDY-C) peptides were purchased from Biomatik Corporation (Figs. 3.8,3.9). Notably, the C-terminus was amidated on the HRD-NGN peptide to avoid side reactions upon coupling. The carbodiimide coupling reagent EDC was purchased from Oakwood Chemicals. All other chemicals and reagents were purchased from Sigma-Aldrich (Canada).

3.4.2 Synthesis and Characterization of Peptide-Functionalized Microgels

Peptide-functionalized microgels were prepared using a previously published protocol, with minor modifications.[39] Briefly, 100 mg of PEG-diacrylamide (MW = 80000 g/mol) was added to a 1 M sodium sulfate solution and vigorously agitated to initiate the phase separation of the PEG microdroplets. To induce gelation, 0.1 wt% Irgacure 2959 radical photoinitiator was added, and the mixture was cured for 90 s using Heraeus HiLite Power UV-curing unit (Heraeus Kulzer, Germany). Subsequently, the microgel particles were washed and centrifuged several times with milli-Q water to remove the excess salt (Fig. 3.2A). This yields microgels with a diameter between 5 µm and 50 µm, and an Young's modulus that ranges between 100 and 250 kPa[39]. To make the microgels reactive, we grafted carboxylic acid groups onto their surfaces using 500 mg of benzophenone and 3 g of crotonic acid for 15 min under UV light (Fig. 3.2B). This step was repeated five times to ensure high carboxylation yield. The appearance of a sharp carbonyl peak around 1720 cm^{-1} in the ATR- FTIR spectrum (Bruker Alpha II) shows successful grafting (Fig. 3.2C). Next, the microgels were washed several times, and the solvent was exchanged with 0.1 M MES buffer (pH=5.3). For peptide coupling, 90 mg EDC and 80 mg of sulfo-NHS were added to the mixture and shaken for 3 h at room temperature to activate the grafted carboxylic acid groups. After activation, 10 mg of HRD-NGN peptide was added and allowed to react overnight. Finally, the microgels were washed, and peptide functionalization was characterized using ATR-FTIR spectroscopy and confocal Raman microscopy (Fig. 3.2C, D). The same bioconjugation protocol was used to link GRGDY peptide to the surface of the microgels (Fig. 3.7).[42]

3.4.3 ATR-FTIR Spectroscopy

Attenuated total reflectance Fourier transform infrared (ATR-FTIR) spectra were collected from dried microgels using (Bruker Alpha II) equipped with a monolithic diamond ATR accessory (Wavenumber range 500-4000 cm^{-1}, 24 scans, resolution 4 cm^{-1}) after each step to monitor the reactions. Data were collected and processed using OPUS software (7.5) to average collected spectra and remove background signal.

3.4.4 Confocal Raman Spectroscopy

Raman spectroscopic measurements were also performed to characterize the functionalization of the microgels, as well as peptide metal coordination in the presence of zinc ions. These spectra were collected from the dried microgels on glass slides using a confocal Raman microscope (Alpha 300R, WITec). A 532-nm green laser was used at a power between 10 and 15 mW and focused using a 50x objective (Zeiss, numerical aperture [NA] = 0.9). Spectra were collected with a thermoelectrically cooled CCD detector behind a 600 g/mm grating. For single spectra, a 1 s integration time and 100 accumulations were used. Data was collected using WITec ControlFIVE 5.1 software and processed using the WITec Plus software to remove cosmic rays and subtract the background signal.

3.4.5 Rheological Properties

Rheological properties were assessed using a stress-controlled rheometer (MCR 302, Anton Paar) equipped with a 15 mm diameter cone plate at a 1 mm gap height. Amplitude sweep tests were first performed to assess the linear viscoelastic range of the samples, followed by oscillatory frequency sweeps ranging from 10 Hz to 100 H at 1 % strain. Cyclic loading was done

between 0.1 % and 500 % at 1 Hz. Using a Peltier temperature control unit, the temperature was maintained at 24 ^{0}C for all measurements. A solvent trap was used in all the tests to avoid evaporation.

3.4.6 Preparing Gels for Cell Culture

To prepare microgels for cell culture, they were first suspended in phosphate- buffered saline (PBS) (Sigma) for 30 min, centrifuged at 14,000 rpm (21,000 RCF) for 2 min, the supernatant was removed, and resuspended in PBS two more times. After the final wash, microgels were resuspended in PBS with 1% (v/v) antibiotic-antimycotic (anti-anti) (Thermo Fisher Scientific) and left to sterilize overnight under UV light at 36 W. Peptide-functionalized microgels were then handled under sterile conditions in a biological safety cabinet (BSC). The microgels were then centrifuged, and the supernatant was removed.

3.4.7 HS-5 Bone Marrow-Derived Fibroblasts Cultured with Microgels

50 µL of microgels were plated in a 96 well plate with 200 µL of Dulbecco's Modified Eagle Media (DMEM) supplemented with 10% fetal bovine serum (FBS) and 1% antibiotic-antimycotic (anti-anti) to study the cytocompatibility of the fabricated microgels. The plate was centrifuged at 200 RCF for 2 min to bring the gels to the bottom of the well plate. HS-5 cells (ATCC) were seeded at 50,000 cells per well for 3 wells with approximately 30µl of gel in each well on day 0. Media was changed on day 2, and brightfield images were collected on days 1 and 3 using an EVOS m7000 Cell Imaging System (Thermo Fisher Scientific). Cells were live/dead stained on day 3 with calcein AM (Life Technologies), ethidium homodimer-1 (EthD-1) (Life Technologies), and

Hoechst 33342 (Sigma). Calcein AM was added to the cell culture at a final concentration of 2 µM for staining live cells and EthD-1 was added directly to the cell culture at a final concentration of 4 µM for staining dead cells. Hoechst 33342 was added as a nuclear label of live cells at a concentration of 2 µL/ml directly to the cell culture. Cell cultures were left to incubate with staining reagents at 37 °C for 30 minutes before imaging. The number of live and dead cells was quantified by using image analysis software FIJI (NIH) .[43] A parallel control culture was carried out following the same procedure but without the addition of microgels.

3.5 Results and Discussion

3.5.1 Mussel Inspired Peptide

The peptide used in this study, HRD-NGN (N-GHGGGHGGGHGGGHGGSASAAAHAA-$CONH_2$), is derived from the N-terminal histidine-rich domain of the preCol-NG byssal thread protein from the *Mytilus* species (Fig. 3.1A-C). This specific sequence was chosen because it has been maintained by natural selection across multiple species[44] and has been demonstrated in previous studies to contribute to the pH-triggered assembly of the byssal thread as well as the tough and self-healing behavior of the fiber.[35, 36] The sequence has 5 histidine residues that can bind divalent cations such as Zn^{2+}, Cu^{2+} and Ni^{2+}, which contributes to the toughness and self-assembly of the byssus. As outlined in the next section, this peptide was successfully coupled to microgels using carbodiimide crosslinker chemistry.

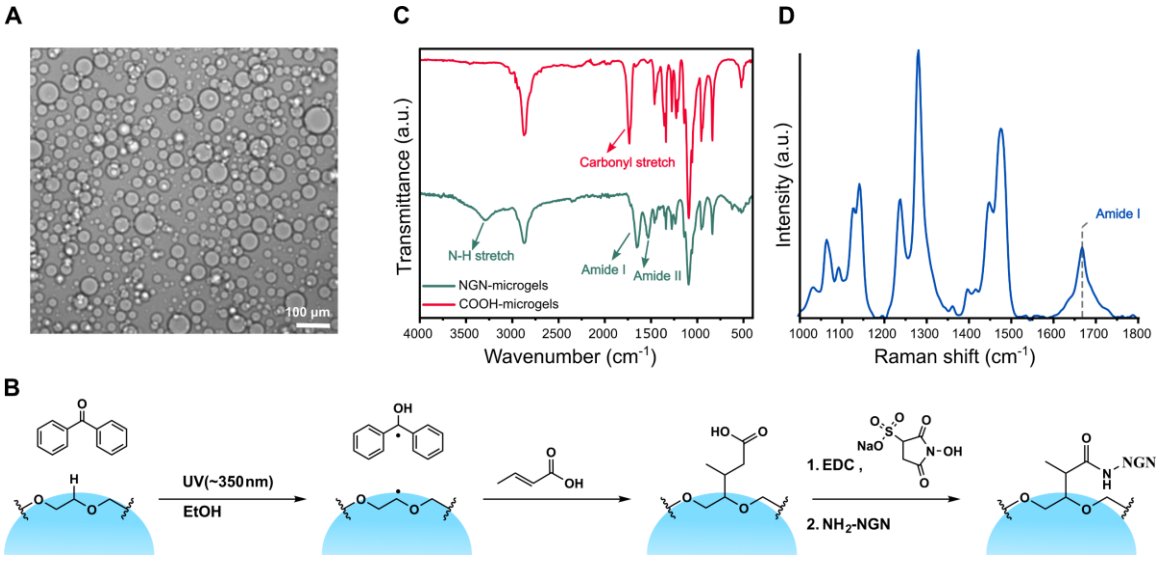

Figure 3.2: Production and post-functionalization of hydrogel microparticles with HRD-NGN peptide. (A) Light microscope image of PEG-diacrylamide microgels using the colloidal suspension method (size 10-50 um). (B) Post-functionalization of PEG microgels with HRD-NGN peptide. Under UV irradiation, benzophenone can abstract a hydrogen atom from the PEG chains, generating surface radicals that allow the coupling of crotonic acid to the surface. Subsequently, carboxylic acid groups on the surface were activated, and the peptide was coupled to the microgels using EDC/NHS chemistry. (C) FTIR spectrum of dried microgels showing successful peptide functionalization (Amide I ~ 1660 cm^{-1} / Amide N-H stretch ~3300 cm^{-1}). (D) Confocal Raman spectrum of the microgels confirms uniform distribution of the peptide on the surface (Amide I ~ 1670 cm^{-1}).

3.5.2 Synthesis and Characterization of Peptide-Functionalized Microgels

PEG microgels were prepared using the colloidal suspension method followed by UV curing to crosslink the polymer network.[39] The size of these microgels produced through this approach ranged between 10 and 50 µm (Fig. 3.2A). To render the surface of the microgels reactive for further functionalization with the HRD-NGN peptide, carboxylic acid groups were added to the

PEG backbone using benzophenone and crotonic acid in the presence of UV light (Fig. 3.2B, 3.5). Finally, the grafted carboxylic acid moieties were activated using carbodiimide chemistry, allowing HRD-NGN to link to the gel network at its N-terminus (Fig. 3.2B). The swelling behavior of these microgels was studied over 7 days in PBS and no significant change in volume was observed (Fig. 3.6). Previous mechanical analysis of HRD-functionalized microgels using an identical production method reported stiffness values of 100 – 250 kPa[39].

Fourier transform infrared (FTIR) spectroscopy and confocal Raman spectroscopy were used to monitor the success of the coupling reactions (Fig. 3.2C-D, 3.5). The ATR-FTIR spectrum (Fig. 3.2C) of dried microgels shows a strong Amide I and amide II vibrations at ~1670 cm^{-1} and 1530 cm^{-1}, as well as the N-H stretch at ~3300 cm^{-1}, which indicates successful peptide functionalization. Confocal Raman spectra were obtained from different spots on the microgels to confirm that the peptide was uniformly distributed on the microgels. As shown in Figure 3.2D, the amide I peak at 1670 cm^{-1}, which arises from the stretching vibration of the peptide backbone carbonyls, indicates efficient and homogenous surface functionalization.

3.5.3 Reversible Annealing Based on Zinc-Histidine Coordination

After successfully functionalizing the surface of the microgels with HRD peptides derived from marine mussels, reversible annealing based on zinc-histidine coordination was tested. Peptide functionalized microgels were loaded into a syringe, and 10 mM $ZnCl_2$ solution was added at pH 5. Under these acidic conditions, microgels will disperse in the solution upon injection (Fig. 3.3A). This is presumably due to the absence of zinc-histidine coordination. However, when the mixture was injected slowly into a physiological buffer (pH 7.4), a robust microporous annealed particle

(MAP) scaffold was rapidly formed (Fig. 3.3A). There was no evidence of significant numbers of free microgels upon injection, indicating a high efficiency of granular hydrogel formation. Microscopic and spectroscopic analysis revealed that the granular hydrogel formed by annealing of the microgels, presumably via zinc-histidine coordination bonds, which is consistent with the pH-dependent metal binding observed in previous studies using this peptide (Fig. 3.3A).[35]

In further support of stabilization via metal coordination bonds, the scaffold can be dispersed on demand through addition of EDTA, which is a broad-range metal chelator with a high binding affinity for zinc metal ions. This process is reversible – after Zn^{2+} ions are re-added to the dispersed system, the microgels can reassemble back into a porous scaffold. Importantly, the reversible annealing of the microgels can also be mediated through pH – annealed granular hydrogels will disperse under mildly acidic conditions and re-anneal under slightly basic conditions. This is also consistent with the role of His-Zn^{2+} coordination given that histidine typically has a pK_a of ~6.5 and the protonated form, dominant under acidic conditions, is unable to participate in metal coordination bonds. As further evidence, we attempted injecting microgels into the physiological buffer in the absence of Zn^{2+} ions and did not observe the formation of an annealed granular hydrogel – rather, the microgels simply dispersed in the solution.

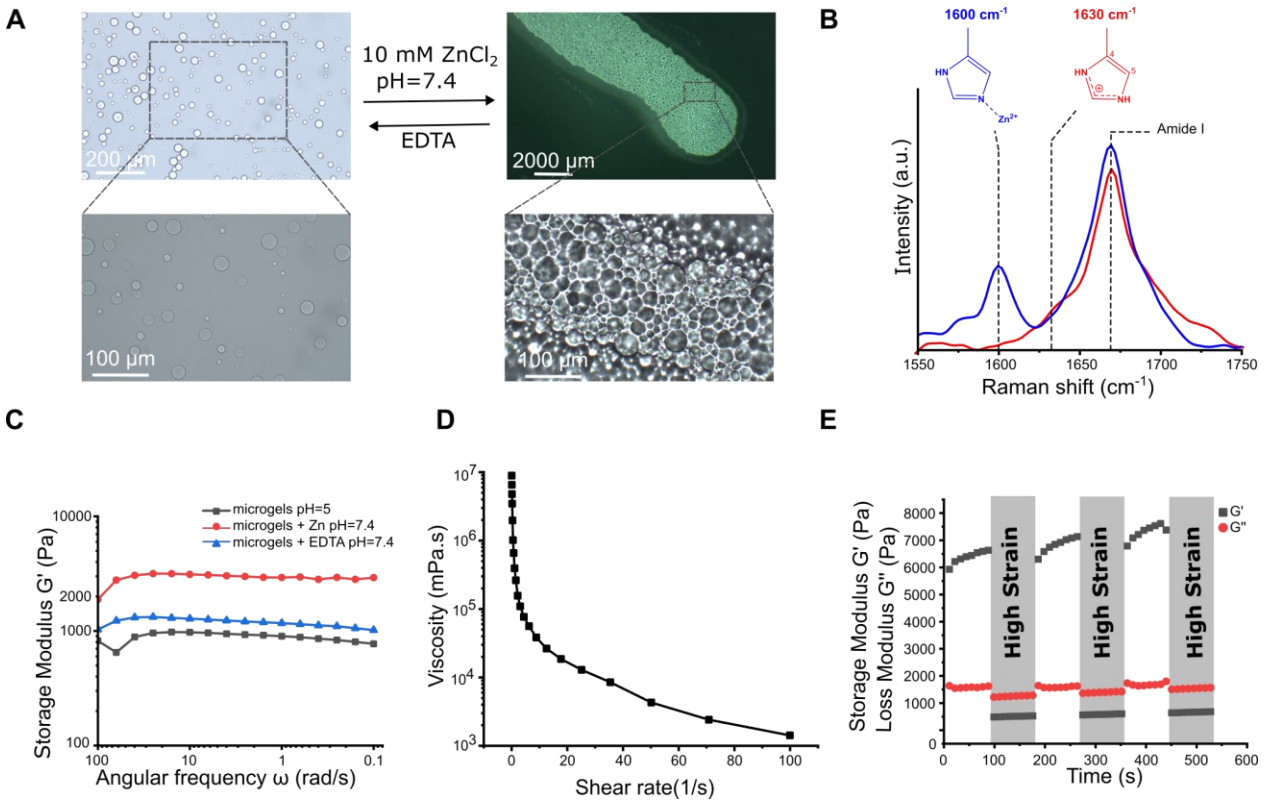

Figure 3.3: Reversible annealing based on zinc-histidine coordination. (A) Peptide-functionalized microgels loaded into a syringe at pH=5 in the presence of low concentrations of $ZnCl_2$ form a MAP scaffold upon injection in PBS buffer at pH=7.4. The crosslinked scaffold can be dispersed by chelating the zinc metal ions with EDTA. (B) Raman spectroscopy of microgels functionalized with HRD-NGN peptide at pH=5 in the absence of Zn^{2+} (red curve) and in the presence of Zn^{2+} at pH=7.4 and a His/Zn^{2+} ratio of 3:1(blue curve). The characteristic wavenumbers of the metal-free and metal-coordinated imidazole ring vibration confirms annealing via zinc/histidine coordination. (C) Frequency sweep at 0.1 % strain for peptide-functionalized microgels at pH=5 (black), annealed peptide-functionalized microgels in the presence of Zn^{2+}at pH=7.4 (red), and MAP scaffold after treatment with EDTA (blue). (D) Viscosity as a function of shear rate shows shear thinning behavior of annealed microgel. (E) Strain-cycle experiment for peptide-functionalized microgels between 1% and 500 % strains.

To further verify that this reversible annealing is based on zinc-histidine coordination, confocal Raman spectra were collected from the dispersed phase and annealed scaffold (Fig. 3B). Unlike FTIR spectroscopy, Raman spectroscopy is able to distinguish between metal-coordinated and non-coordinated His residues because the C_4=C_5 ring vibration of the imidazole moiety is highly sensitive to the protonation, coordination, and tautomerization states of histidine.[45] In the absence of metals at pH 5, a shoulder peak appears at 1630 cm^{-1} assigned to the cationic imidazolium form of histidine[46], in addition to the protein amide I vibration at 1670 cm^{-1}. However, upon the addition of zinc metal and raising the pH to 7.4, a strong peak appears at 1600 cm^{-1}, which based on previous studies of the same peptide and other histidine-containing systems is attributed to His-Zn^{2+} coordination.[39, 46]

3.5.4 Rheology

The mechanical properties of the MAP scaffold and the effect of Zn-histidine coordination on bulk mechanics were tested using oscillatory shear rheology. As shown in figure 3C, the storage modulus G' exhibits an approximately 3-fold increase upon the addition of zinc ions to the dispersed microgels when raising the pH above the pK_a of histidine. The increase in storage modulus is attributed to the increase in the number of crosslinks in the network due to formation of intermolecular His-Zn^{2+} linkages between the faces of adjacent microgels. This indicates that annealing based on metal coordination bonds arising from the HRD peptide can impact the bulk mechanical properties of granular hydrogels. To demonstrate the reversibility of this mechanical transition, the annealed scaffold was dispersed using EDTA, and the same test was repeated, resulting in a return to the initial storage modulus before annealing (Fig. 3C).

Usually, annealing based on non-covalent interactions yields a scaffold with thixotropic and self-healing properties that are conducive to injectability. Such materials exhibit liquid-like flow properties under high shear yet behave as solids at rest. To simulate the injection process, we applied an increasing shear rate to the annealed scaffold (Fig. 3D). Under low shear rate (0.1 s^{-1}), the viscosity was ~9×10^6 mPa·s, showing a solid like behavior. However, a shear-thinning behavior was observed at higher shear rate where the viscosity dropped to ~1420 mPa·s at 100 s^{-1}. To test the reversibility of the annealing crosslinks, we applied an alternating series of low (0.1%) and high (500%) strains (Fig. 3E). Under low-strain conditions, the storage modulus was maintained at 6 kPa while the loss modulus was 3 times lower (G''=1.5kPa) consistent with a more solid-like behavior. When the strain was increased to 500 %, the material rapidly transitioned to a more viscous, fluid-like behavior with a decrease of storage modulus to G'=400 Pa that dropped below the loss modulus (G" =1100 Pa) signifying a tan delta of greater than one. The process was nearly fully reversible upon shifting back to low-strain conditions, with a slight increase in the storage modulus observed over time. It seems plausible that this indicates a slight drying of the sample over time; however, it is also conceivable that the failure of the gel at high strains leads to a reorganization of the bonding network increasing the number of cross-links between microgels. This remains to be verified. Nevertheless, these rheological properties render these microgels injectable without affecting their performance post-injection due to their ability to regenerate their moduli at rest. Because of their thixotropic behavior, this would conceivably allow them to be 3D printed into various shapes to conform to the needs of different biomedical applications.

3.5.5 Cytocompatibility of Zinc-Annealed Scaffolds

The potential of His-Zn^{2+} annealed MAP scaffolds for applications in 3D cell culture was tested using HS-5 human fibroblasts as a model cell culture line, as shown in Figure 3.4. Peptide-functionalized PEG microgels were further modified with RGD containing peptides using carbodiimide chemistry to support cell adhesion on the granular bead surfaces (Fig. 3.4A, 3.7).[42] Control tests revealed that the addition of the GRGDY peptide to the HRD-NGN-functionalized microgels did not affect the ability of microgels to anneal. The annealed scaffolds were then mixed with HS-5 fibroblasts and centrifuged to incorporate them within the granular scaffold. A gel volume of approximately 30 µl was seeded with approximately 50,000 HS-5 cells in each of 3 wells and incubated for 3 days. As shown in Figure 3.4A-C, cells quickly integrated into the scaffolds by filling the connecting microscale voids and adhering to the microgels. The live and dead cell assay in figure 3.4A showed minimal cell death and good cell spreading, demonstrating that the cells are metabolically active and engaging with the scaffold with no signs of cytotoxicity. Cell viability, defined as the number of live cells divided by the total cell number, was found to be 86 ± 3% for the annealed MAP scaffold, which is comparable to that of control media at 81 ± 11% for this specific experimental cell passage (Fig. 3.4E). These results indicate that the annealed scaffold shows no cytotoxicity over a period of 3 days, indicating promise for future development as an injectable ECM-like microenvironment. After three days, the observed development of pseudopodia indicates that the fibroblasts are spreading within the annealed microgels (white arrows, Fig. 3.4C).

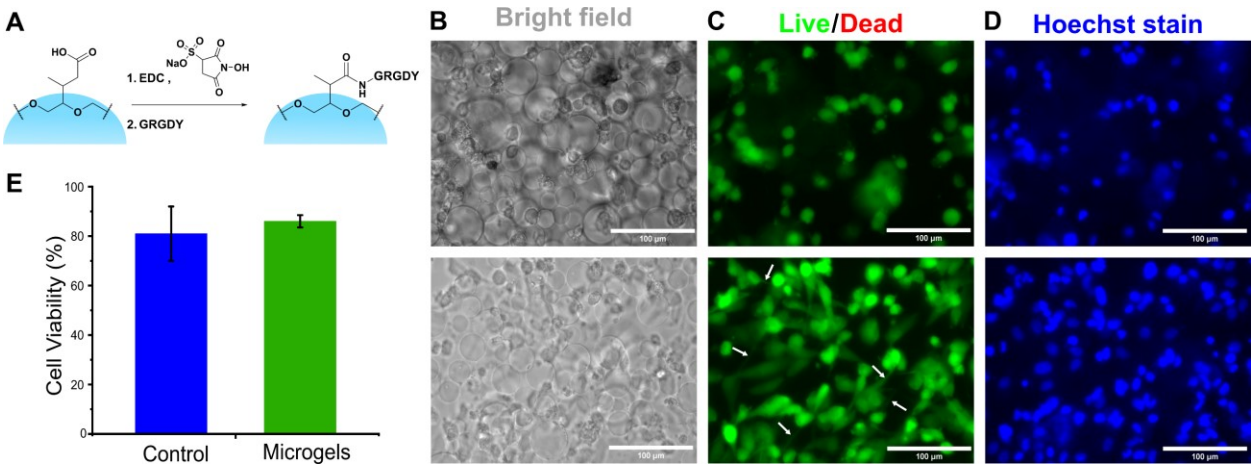

Figure 3.4: Zinc-annealed microgels provide a porous scaffold for 3D cell culture. (A) Functionalization of microgels with GRGDY peptide using carbodiimide chemistry to enhance cell viability and cellular adhesion. (B) Bright-field images showing HS-5/fibroblasts in the zinc-annealed microgels after 3 days. (C) Assessment of live (green) and dead (red) cells, showing that the 3D culture of HS-5/fibroblasts in annealed scaffolds show no sign of cytotoxicity and good cell spreading based on the appearance of pseudopodia after 3 days (white arrows). (D) Fluorescence microscopy images of cells stained with Hoechst 33342 to localize the nuclei of the fibroblast cells. (E) Cell viability graph shows that zinc-annealed scaffolds do not show any sign of cytotoxicity and provide a medium for the fibroblasts.

3.6 Conclusion

We developed an injectable MAP scaffold using histidine-zinc coordination inspired by protein sequences that marine mussels utilize to self-assemble tough and self-healing collagenous fibers from liquid crystal precursor phases. Analogous to the self-assembly of preCol proteins into high-performance fibers upon secretion into seawater, microgels functionalized with the pH-responsive HRD-NGN peptide can instantly form a mechanically robust, porous scaffold upon injection into physiological media. Owing to the dynamic nature of the annealing crosslinks, this

hydrogel displayed thixotropic and self-healing properties that provide a strong potential for injection – e.g., into motile tissue environments or for use in 3D printing applications. The scaffold can also be reversibly separated back into dispersed microgels by disrupting the complexation of Zn^{2+} ions either through lowering pH conditions or by using a metal chelator (e.g., EDTA). Finally, these annealed scaffolds stabilized via strong, yet reversible metal coordination bonds provide a cytocompatible microenvironment, resulting in good cell viability and spreading.

3.7 Supplementary Information

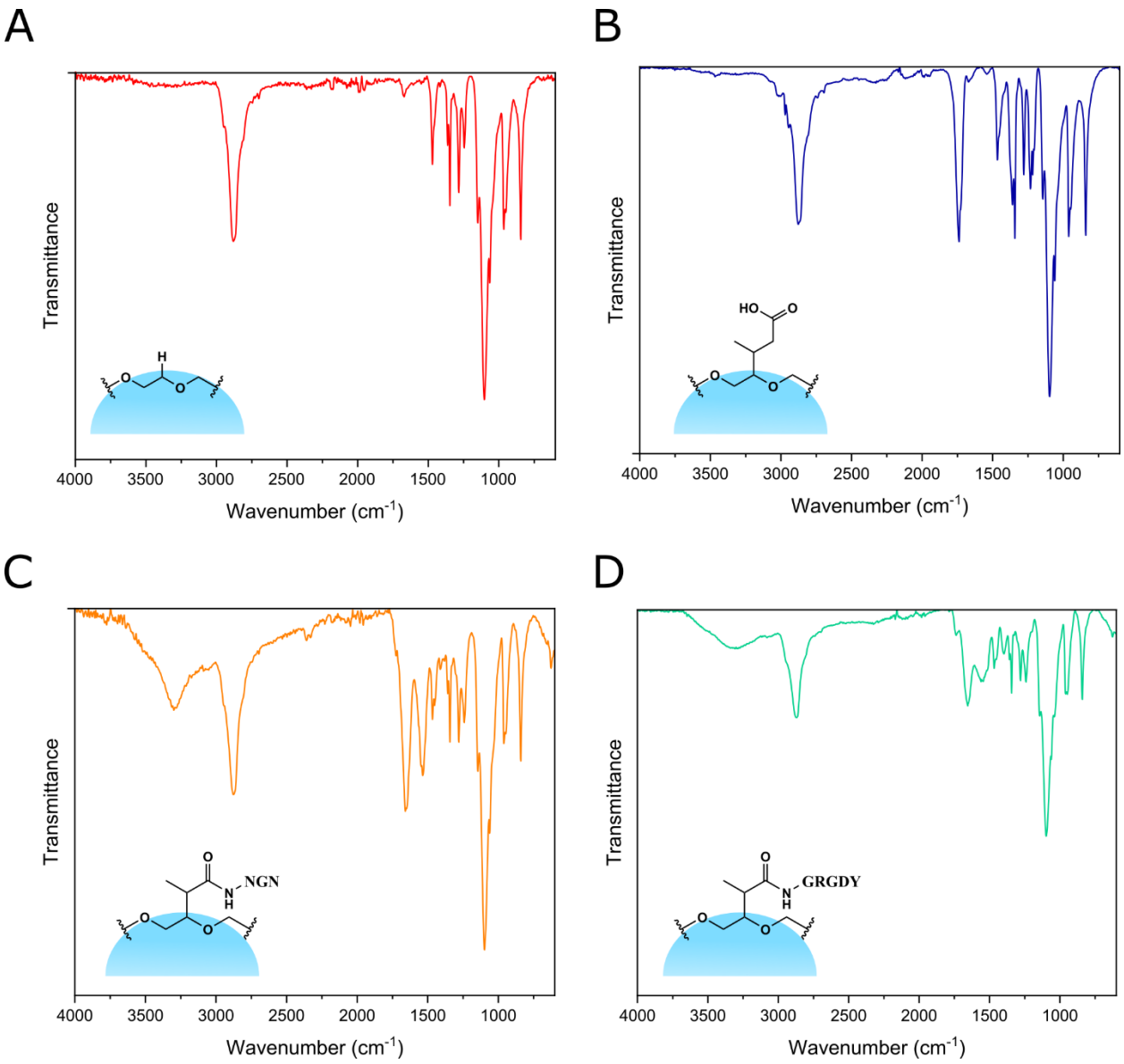

Figure 3.5: FTIR of microgels at different stages of functionalization. A) FTIR-spectrum of unfunctionalized microgels. B) Carboxylated microgels. C) NGN-functionalized microgels. D) GRGDY- functionalized microgels.

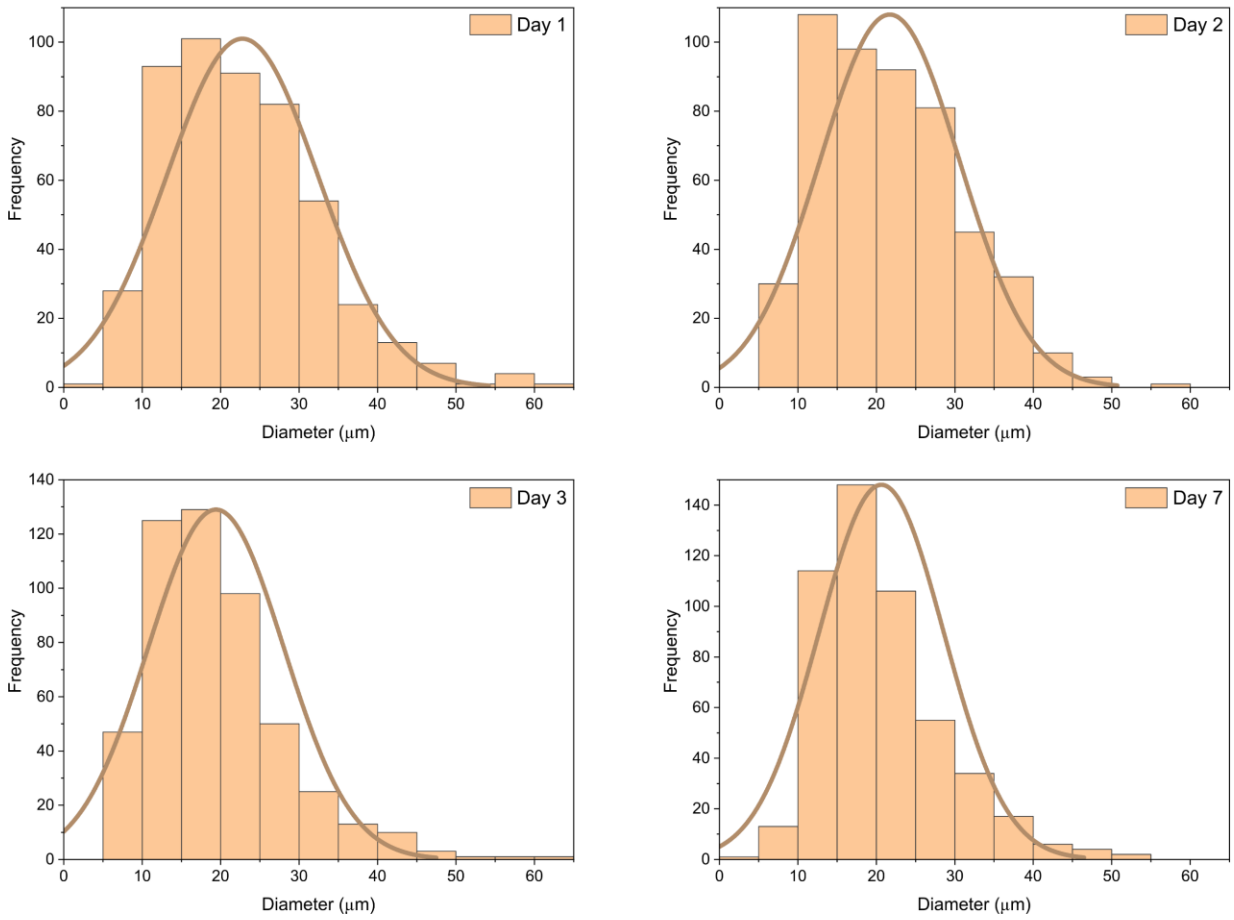

Figure 3.6: Microgel swelling and stability experiments. Histograms showing how microgel diameter stays constant over a period of 7 days. Diameter measured from light microscope images of dispersed microgels using ImageJ (N = ~500 microgels for each time point).

Synthesis of HRD-NGN/RGD microgels

100 mg of PEG-diacrylamide (MW = 80000 g/mol) was added to a 1 M sodium sulfate solution and vigorously shaken to form PEG microdroplets. To form the microgels, 0.1 wt% Irgacure 2959 radical photoinitiator was added, and the mixture was cured for 90 s using Heraeus HiLite Power UV-curing unit (Heraeus Kulzer, Germany). Excess salt was washed away through multiple

centrifugations and rinsing with milli-Q water. Carboxylic acid groups were then grafted onto the microgels using 500 mg of benzophenone and 3 g of crotonic acid for 15 min under UV light (Fig. 3.2B). This step was repeated five times to ensure high carboxylation yield. Next, the microgels were washed several times, and the solvent was exchanged with 0.1 M MES buffer (pH=5.3). For peptide coupling, 90 mg EDC and 80 mg of sulfo-NHS were added to the mixture and shaken for 3 h at room temperature to activate the grafted carboxylic acid groups. After activation, 10 mg of HRD-NGN peptide and 2 mg of GRGDY peptide were dissolved in 0.1 M MOPS buffer (pH=7), added to the microgels, and the mixture was allowed to react overnight.

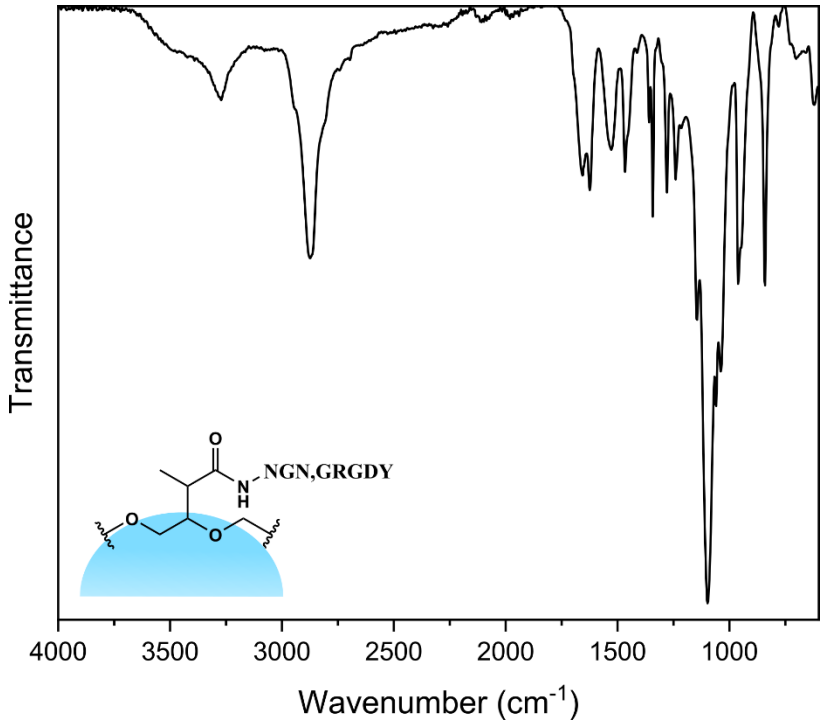

Figure 3.7: FTIR spectrum of microgels functionalized with HRD-NGN and GRGDY peptides (dry state).

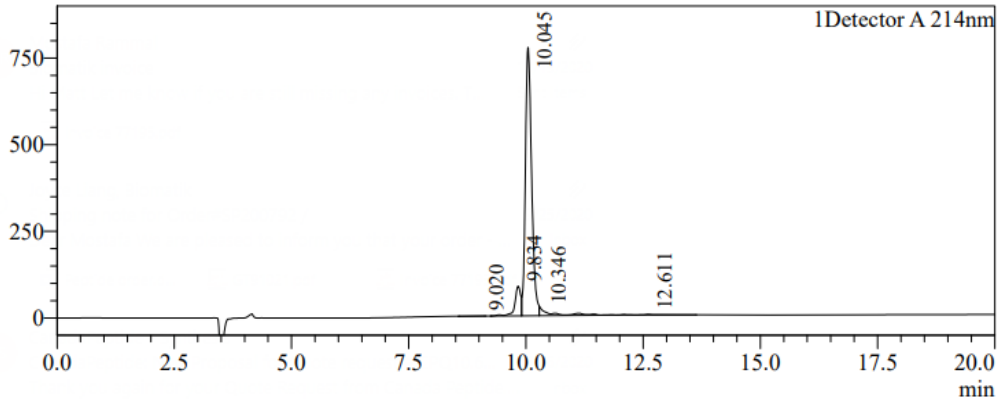

Peak Table

Detector A 214nm

Peak#	Ret. Time	Area	Height	Area%
1	9.020	9719	364	0.12
2	9.834	745773	85713	8.90
3	10.045	7160256	774034	85.47
4	10.346	393102	16616	4.69
5	12.611	68757	2153	0.82
Total		8377606	878881	100.00

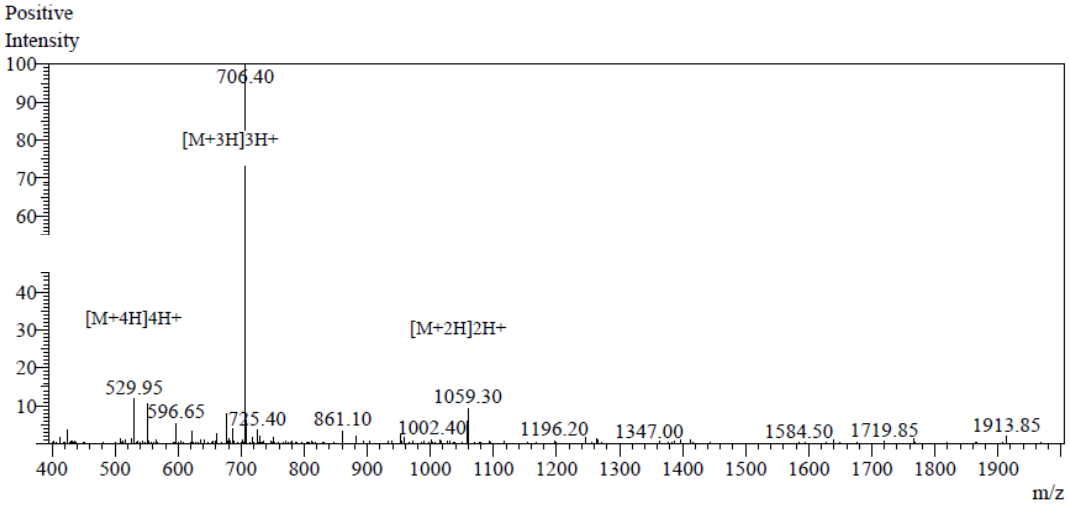

Dissolution method	:5%HAC+8%ACN+87%H2O	Interface	:ESI
Date Acquired	:2020/09/11 15:02:55	Detector	:-0.2kv
Injection Volume	:0.2ul	CDL Temp	:250C
Nebulizing Gas	:1.5L/min	CDL Volt	:0v
Prerod Bias	:+4.5kv	Block Temp	:200
T.Flow	:0.2ml/min	B.conc	:50%H2O/50%MEOH

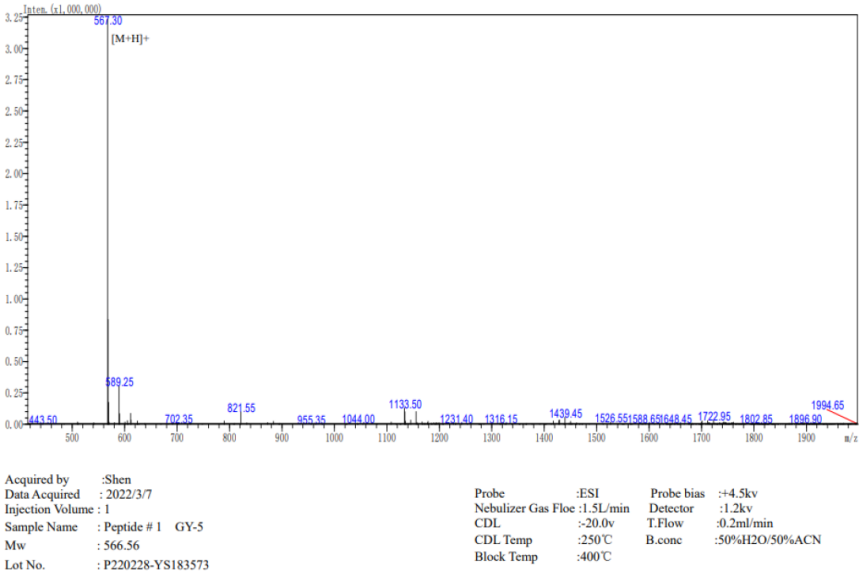

Figure 3.8: HPLC analysis and mass spectrometry of HRD-NGN peptide (Biomatik Inc.).

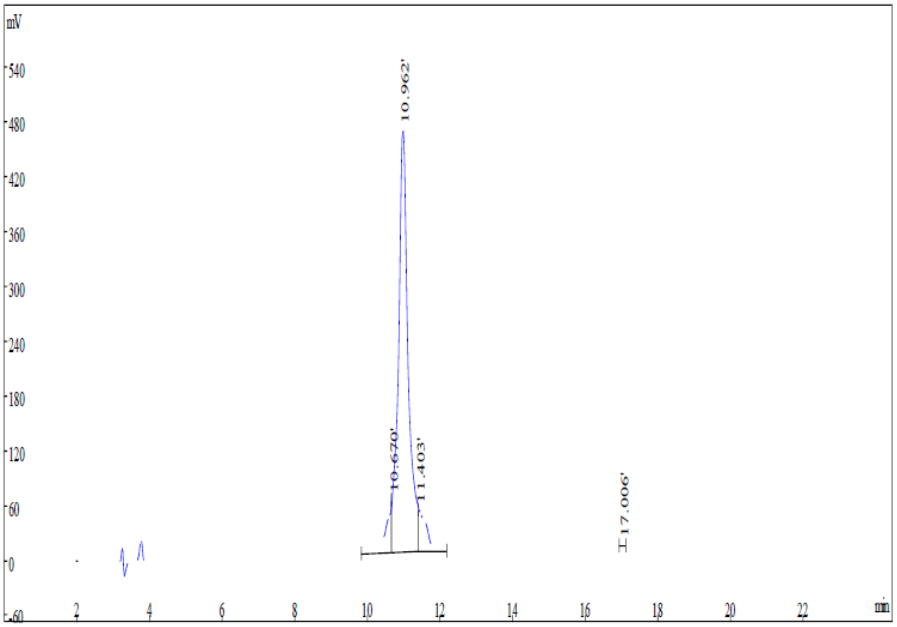

Rank	Time	Conc.	Area	Height
1	10.670	6.972	654620	57239
2	10.962	86.61	8131155	460369
3	11.403	6.382	599218	45280
4	17.006	0.03862	3626	617
Total		100	9388619	563505

Figure 3.9: HPLC analysis and mass spectrometry of GRGDY peptide (Biomatik Inc.).

3.8 References

1. Rammal, M.; Li, C.; Reeves, J.; Moraes, C.; Harrington, M. J., pH-Responsive Reversible Granular Hydrogels Based on Metal-Binding Mussel-Inspired Peptides. *ACS Applied Materials & Interfaces* **2023,** *15* (24), 29004-29011.

2. Griffin, D. R.; Weaver, W. M.; Scumpia, P. O.; Di Carlo, D.; Segura, T., Accelerated wound healing by injectable microporous gel scaffolds assembled from annealed building blocks. *Nature Materials* **2015,** *14* (7), 737-744.

3. Gu, Z.; Dang, T. T.; Ma, M.; Tang, B. C.; Cheng, H.; Jiang, S.; Dong, Y.; Zhang, Y.; Anderson, D. G., Glucose-Responsive Microgels Integrated with Enzyme Nanocapsules for Closed-Loop Insulin Delivery. *ACS Nano* **2013,** *7* (8), 6758-6766.

4. Feyen, D. A. M.; Gaetani, R.; Deddens, J.; van Keulen, D.; van Opbergen, C.; Poldervaart, M.; Alblas, J.; Chamuleau, S.; van Laake, L. W.; Doevendans, P. A.; Sluijter, J. P. G., Gelatin Microspheres as Vehicle for Cardiac Progenitor Cells Delivery to the Myocardium. *Advanced Healthcare Materials* **2016,** *5* (9), 1071-1079.

5. Van Vlierberghe, S.; Dubruel, P.; Schacht, E., Biopolymer-Based Hydrogels As Scaffolds for Tissue Engineering Applications: A Review. *Biomacromolecules* **2011,** *12* (5), 1387-1408.

6. Highley, C. B.; Song, K. H.; Daly, A. C.; Burdick, J. A., Jammed Microgel Inks for 3D Printing Applications. *Advanced Science* **2019,** *6* (1), 1801076.

7. Daly, A. C.; Riley, L.; Segura, T.; Burdick, J. A., Hydrogel microparticles for biomedical applications. *Nature Reviews Materials* **2020,** *5* (1), 20-43.

8. Hasan, A.; Khattab, A.; Islam, M. A.; Hweij, K. A.; Zeitouny, J.; Waters, R.; Sayegh, M.; Hossain, M. M.; Paul, A., Injectable Hydrogels for Cardiac Tissue Repair after Myocardial Infarction. *Advanced Science* **2015,** *2* (11), 1500122.

9. Taheri, S.; Bao, G.; He, Z.; Mohammadi, S.; Ravanbakhsh, H.; Lessard, L.; Li, J.; Mongeau, L., Injectable, Pore-Forming, Perfusable Double-Network Hydrogels Resilient to Extreme Biomechanical Stimulations. *Advanced Science* **2022,** *9* (2), 2102627.

10. Nih, L. R.; Sideris, E.; Carmichael, S. T.; Segura, T., Injection of Microporous Annealing Particle (MAP) Hydrogels in the Stroke Cavity Reduces Gliosis and Inflammation and Promotes NPC Migration to the Lesion. *Advanced Materials* **2017,** *29* (32), 1606471.

11. Truong, N. F.; Kurt, E.; Tahmizyan, N.; Lesher-Pérez, S. C.; Chen, M.; Darling, N. J.; Xi, W.; Segura, T., Microporous annealed particle hydrogel stiffness, void space size, and adhesion properties impact cell proliferation, cell spreading, and gene transfer. *Acta Biomaterialia* **2019,** *94*, 160-172.

12. Wilson, K. L.; Pérez, S. C. L.; Naffaa, M. M.; Kelly, S. H.; Segura, T., Stoichiometric Post-Modification of Hydrogel Microparticles Dictates Neural Stem Cell Fate in Microporous Annealed Particle Scaffolds. *Advanced Materials* **2022,** *34*, 2201921.

13. Caldwell, A. S.; Campbell, G. T.; Shekiro, K. M. T.; Anseth, K. S., Clickable Microgel Scaffolds as Platforms for 3D Cell Encapsulation. *Advanced Healthcare Materials* **2017,** *6* (15), 1700254.

14. Li, F.; Truong, V. X.; Fisch, P.; Levinson, C.; Glattauer, V.; Zenobi-Wong, M.; Thissen, H.; Forsythe, J. S.; Frith, J. E., Cartilage tissue formation through assembly of microgels containing mesenchymal stem cells. *Acta Biomaterialia* **2018,** *77*, 48-62.

15. Sheikhi, A.; de Rutte, J.; Haghniaz, R.; Akouissi, O.; Sohrabi, A.; Di Carlo, D.; Khademhosseini, A., Microfluidic-enabled bottom-up hydrogels from annealable naturally-derived protein microbeads. *Biomaterials* **2019,** *192*, 560-568.

16. Hsu, R.-S.; Chen, P.-Y.; Fang, J.-H.; Chen, Y.-Y.; Chang, C.-W.; Lu, Y.-J.; Hu, S.-H., Adaptable Microporous Hydrogels of Propagating NGF-Gradient by Injectable Building Blocks for Accelerated Axonal Outgrowth. *Advanced Science* **2019,** *6* (16), 1900520.

17. Mealy, J. E.; Chung, J. J.; Jeong, H.-H.; Issadore, D.; Lee, D.; Atluri, P.; Burdick, J. A., Injectable Granular Hydrogels with Multifunctional Properties for Biomedical Applications. *Advanced Materials* **2018,** *30* (20), 1705912.

18. Khare, E.; Holten-Andersen, N.; Buehler, M. J., Transition-metal coordinate bonds for bioinspired macromolecules with tunable mechanical properties. *Nature Reviews Materials* **2021,** *6* (5), 421-436.

19. Chaudhuri, O.; Gu, L.; Klumpers, D.; Darnell, M.; Bencherif, S. A.; Weaver, J. C.; Huebsch, N.; Lee, H.-p.; Lippens, E.; Duda, G. N.; Mooney, D. J., Hydrogels with tunable stress relaxation regulate stem cell fate and activity. *Nature Materials* **2016,** *15* (3), 326-334.

20. Zechel, S.; Hager, M. D.; Priemel, T.; Harrington, M. J., Healing through Histidine: Bioinspired Pathways to Self-Healing Polymers via Imidazole–Metal Coordination. *Biomimetics* **2019,** *4* (1), 20.

21. Fullenkamp, D. E.; He, L.; Barrett, D. G.; Burghardt, W. R.; Messersmith, P. B., Mussel-Inspired Histidine-Based Transient Network Metal Coordination Hydrogels. *Macromolecules* **2013,** *46* (3), 1167-1174.

22. Weng, W.; Beck, J. B.; Jamieson, A. M.; Rowan, S. J., Understanding the Mechanism of Gelation and Stimuli-Responsive Nature of a Class of Metallo-Supramolecular Gels. *Journal of the American Chemical Society* **2006,** *128* (35), 11663-11672.

23. Sun, W.; Xue, B.; Fan, Q.; Tao, R.; Wang, C.; Wang, X.; Li, Y.; Qin, M.; Wang, W.; Chen, B.; Cao, Y., Molecular engineering of metal coordination interactions for strong, tough, and fast-recovery hydrogels. *Science Advances* **2020,** *6* (16), eaaz9531.

24. Lee, B. P.; Messersmith, P. B.; Israelachvili, J. N.; Waite, J. H., Mussel-Inspired Adhesives and Coatings. *Annual Review of Materials Research* **2011,** *41* (1), 99-132.

25. Harrington, M. J.; Masic, A.; Holten-Andersen, N.; Waite, J. H.; Fratzl, P., Iron-Clad Fibers: A Metal-Based Biological Strategy for Hard Flexible Coatings. *Science* **2010,** *328* (5975), 216-220.

26. Degtyar, E.; Harrington, M. J.; Politi, Y.; Fratzl, P., The mechanical role of metal ions in biogenic protein-based materials. *Angew. Chem. Intl. Ed.* **2014,** *53* (45), 12026-12044.

27. Holten-Andersen, N.; Mates, T. E.; Toprak, M. S.; Stucky, G. D.; Zok, F. W.; Waite, J. H., Metals and the Integrity of a Biological Coating: The Cuticle of Mussel Byssus. *Langmuir* **2009,** *25* (6), 3323-3326.

28. Jehle, F.; Macías-Sánchez, E.; Sviben, S.; Fratzl, P.; Bertinetti, L.; Harrington, M. J., Hierarchically-structured metalloprotein composite coatings biofabricated from co-existing condensed liquid phases. *Nat. Commun.* **2020,** *11* (1), 862.

29. Renner-Rao, M.; Clark, M.; Harrington, M. J., Fiber Formation from Liquid Crystalline Collagen Vesicles Isolated from Mussels. *Langmuir* **2019,** *35* (48), 15992-16001.

30. Reinecke, A.; Bertinetti, L.; Fratzl, P.; Harrington, M. J., Cooperative behavior of a sacrificial bond network and elastic framework in providing self-healing capacity in mussel byssal threads. *Journal of Structural Biology* **2016,** *196* (3), 329-339.

31. Waite, J. H.; Qin, X.-X.; Coyne, K. J., The peculiar collagens of mussel byssus. *Matrix Biology* **1998,** *17* (2), 93-106.

32. Krauss, S.; Metzger, T. H.; Fratzl, P.; Harrington, M. J., Self-repair of a biological fiber guided by an ordered elastic framework. *Biomacromolecules* **2013,** *14* (5), 1520-1528.

33. Coyne, K. J.; Qin, X.-X.; Waite, J. H., Extensible Collagen in Mussel Byssus: A Natural Block Copolymer. *Science* **1997,** *277* (5333), 1830-1832.

34. Jehle, F.; Priemel, T.; Strauss, M.; Fratzl, P.; Bertinetti, L.; Harrington, M. J., Collagen Pentablock Copolymers Form Smectic Liquid Crystals as Precursors for Mussel Byssus Fabrication. *ACS Nano* **2021,** *15* (4), 6829-6838.

35. Reinecke, A.; Brezesinski, G.; Harrington, M. J., pH-Responsive Self-Organization of Metal-Binding Protein Motifs from Biomolecular Junctions in Mussel Byssus. *Advanced Materials Interfaces* **2017,** *4* (1), 1600416.

36. Schmitt, C. N. Z.; Politi, Y.; Reinecke, A.; Harrington, M. J., Role of Sacrificial Protein–Metal Bond Exchange in Mussel Byssal Thread Self-Healing. *Biomacromolecules* **2015,** *16* (9), 2852-2861.

37. Grindy, S. C.; Learsch, R.; Mozhdehi, D.; Cheng, J.; Barrett, D. G.; Guan, Z.; Messersmith, P. B.; Holten-Andersen, N., Control of hierarchical polymer mechanics with bioinspired metal-coordination dynamics. *Nature Materials* **2015,** *14* (12), 1210-1216.

38. Pussak, D.; Behra, M.; Schmidt, S.; Hartmann, L., Synthesis and functionalization of poly(ethylene glycol) microparticles as soft colloidal probes for adhesion energy measurements. *Soft Matter* **2012,** *8* (5), 1664-1672.

39. Schmidt, S.; Reinecke, A.; Wojcik, F.; Pussak, D.; Hartmann, L.; Harrington, M. J., Metal-Mediated Molecular Self-Healing in Histidine-Rich Mussel Peptides. *Biomacromolecules* **2014,** *15* (5), 1644-1652.

40. Trapaidze, A.; D'Antuono, M.; Fratzl, P.; Harrington, M. J., Exploring mussel byssus fabrication with peptide-polymer hybrids: Role of pH and metal coordination in self-assembly and mechanics of histidine-rich domains. *European Polymer Journal* **2018,** *109*, 229-236.

41. Jehle, F.; Fratzl, P.; Harrington, M. J., Metal-Tunable Self-Assembly of Hierarchical Structure in Mussel-Inspired Peptide Films. *ACS Nano* **2018,** *12* (3), 2160-2168.

42. Rowley, J. A.; Madlambayan, G.; Mooney, D. J., Alginate hydrogels as synthetic extracellular matrix materials. *Biomaterials* **1999,** *20* (1), 45-53.

43. Schindelin, J.; Arganda-Carreras, I.; Frise, E.; Kaynig, V.; Longair, M.; Pietzsch, T.; Preibisch, S.; Rueden, C.; Saalfeld, S.; Schmid, B.; Tinevez, J.-Y.; White, D. J.; Hartenstein, V.; Eliceiri, K.; Tomancak, P.; Cardona, A., Fiji: an open-source platform for biological-image analysis. *Nature Methods* **2012,** *9* (7), 676-682.

44. Harrington, M. J.; Waite, J. H., Holdfast heroics: comparing the molecular and mechanical properties of Mytilus californianus byssal threads. *J. Exp. Biol.* **2007,** *210* (24), 4307-4318.

45. Toyama, A.; Ono, K.; Hashimoto, S.; Takeuchi, H., Raman Spectra and Normal Coordinate Analysis of the N1−H and N3−H Tautomers of 4-Methylimidazole: Vibrational Modes of Histidine Tautomer Markers. *The Journal of Physical Chemistry A* **2002,** *106* (14), 3403-3412.

46. Takeuchi, H., Raman structural markers of tryptophan and histidine side chains in proteins. *Biopolymers* **2003,** *72* (5), 305-317.

Chapter 4 : Mussel-Inspired Self-Healing and Thermochromic Elastomeric Films Via Catechol-Vanadium Coordination

4.1 Preface

In **Chapter 3**, we utilized histidine-zinc coordination that marine mussels use to self-assemble strong, self-healing collagenous fibers from liquid crystal precursor phases to develop a tough, injectable, and self-healing MAP scaffold. These annealed scaffolds offer a cytocompatible microenvironment that promotes good cell viability and spreading.

Chapter 4 introduces a new method for the fabrication of flexible, robust, and effective thermochromic materials inspired vanadium-catechol coordination in the cuticle of the mussel byssus. Our method provides a simple, low temperature methodology for generating VO_2 hydrogels and elastomeric films that preserve the intrinsic thermochromic characteristics of VO_2 nanoparticles.

This chapter is the subject of a manuscript in preparation under the title "**Mussel-Inspired Self-Healing and Thermochromic Elastomeric Films via Catechol Vanadium Coordination"** by Mostafa Rammal, Matthew Harrington.

4.2 Abstract

Smart flexible materials capable of dynamically adjusting or manifesting different properties in response to an applied stimulus are in high demand due to their versatile applications in various fields, such as transparent electronics, soft robotics, and smart windows. For instance, vanadium dioxide (VO_2) thin films show considerable promise as energy-efficient coatings due to their thermochromic properties. However, conventional fabrication methods necessitate the utilization of sophisticated and costly instrumentation or high temperature annealing processes. Such conditions can alter the oxidation state of vanadium, potentially compromising its thermochromic properties. Furthermore, owing to the intrinsic crystalline structure of VO_2, films produced via conventional methods typically exhibit a marked brittleness. Thus, the challenge relies in developing a facile, scalable, and cost-effective fabrication process, making thermochromic technology more accessible and affordable for a variety of applications. To address these limitations, we developed a room-temperature process to fabricate thermochromic VO_2 hydrogels and elastomeric films, inspired by the vanadium-catechol coordination chemistry that mussels use to produce high-performance adhesive fibers. The straightforward fabrication of these polymeric systems, while preserving the thermochromic properties of the nanoparticles, marks a valuable approach for producing high-performance, flexible thermochromic materials.

4.3 Introduction

Thermochromic materials have garnered considerable attention in recent years due to their ability to reversibly modulate optical and electrical properties in response to temperature changes. Notably, vanadium dioxide (VO_2) is the most extensively studied and utilized thermochromic material, primarily due to its reversible monoclinic-rutile structural phase transition leading to a shift from an infrared-transparent semiconductor state to a reflective metallic state occurring around 68 °C.[1] Doping of VO_2 crystals with elements like tungsten (W), molybdenum (Mo), and niobium (Nb) enables precise control over the phase-transition temperature (τ_c) and optical properties of the material.[2-4] These intriguing characteristics render VO_2 appealing for various applications, including flexible electronics,[1, 5, 6] smart windows,[7] thermal sensors,[8] artificial skin, [9] and camouflage devices. [10]

Traditional fabrication methods, such as pulsed laser deposition,[11] chemical vapor deposition,[12] and magnetron sputtering,[13] often require vacuum-based deposition and annealing at elevated temperatures. Despite their prevalence, these techniques pose challenges related to cost, stability, processing temperatures, film oxidation, and substrate compatibility.[14] Solution-based and polymer-assisted deposition methods have emerged as alternatives, offering economical, scalable, and chemically versatile means to produce high-performance thermochromic materials.[15] However, given the susceptibility of oxidation into less thermochromically efficient polymorphs, maintaining nanoparticle stability and ensuring uniform distribution are paramount for optimizing material's performance.[16] Embedding VO_2 nanoparticles within a polymer matrix has shown potential in creating flexible films while protecting nanoparticles from degradation.[15,

[17] Nevertheless, achieving a homogeneous distribution of nanoparticles within the polymer matrix poses a challenge due to nanoparticle agglomeration resulting from weak polymer-nanoparticles interactions. Hence, addressing these challenges involves optimizing the dispersion process through engineering the polymer-nanoparticles interactions, ultimately yielding thermochromic materials with superior mechanical properties and long-term stability. Inspired by marine mussels, utilizing catechol-metal coordination bonds between the polymer and the nanoparticles could offer an intriguing solution to this problem.

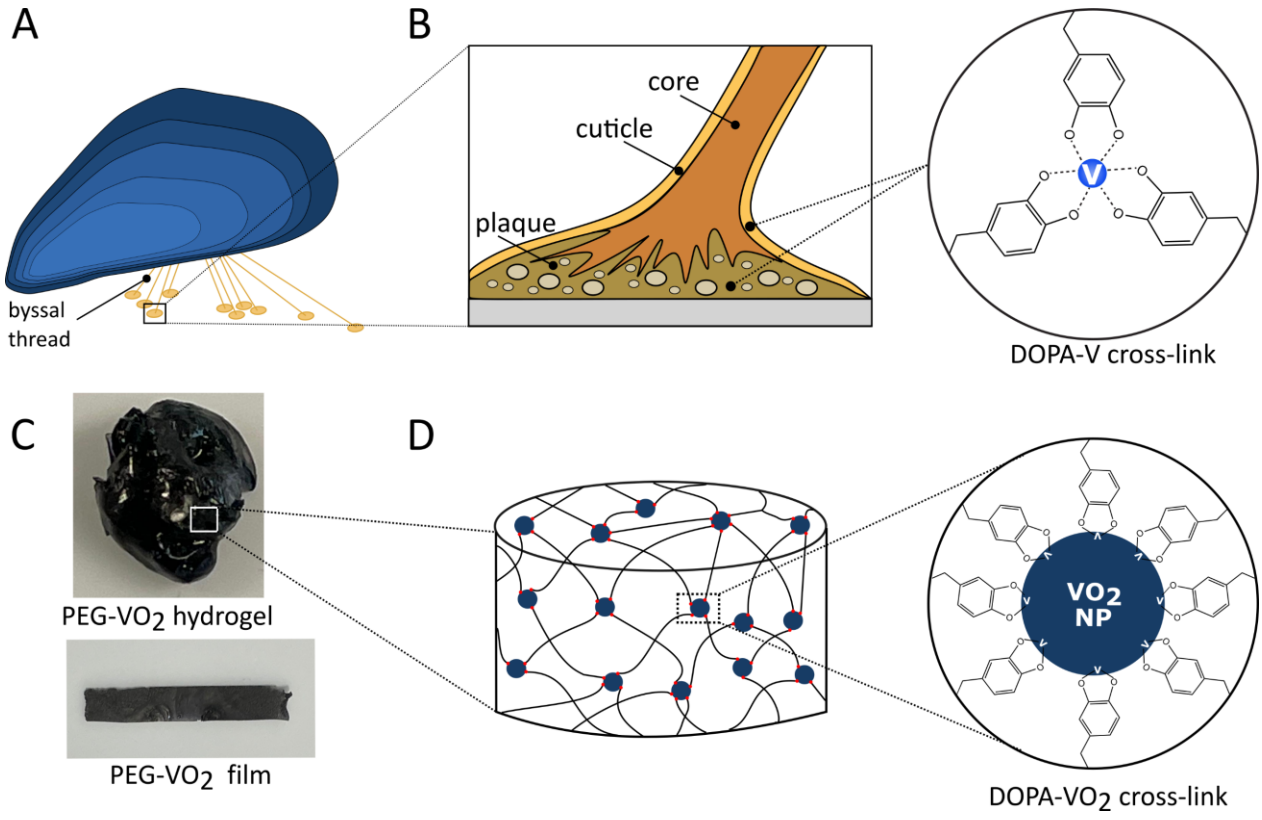

Figure 4.1: Mussel-inspired fabrication of thermochromic VO_2 hydrogels and films. (A) Mussels produce durable anchoring filaments, referred to as byssal threads. (B) Schematic representation of a single thread, illustrating the fibrous core, protective cuticle, and the porous adhesive plaque. Vanadium-catechol coordination is an important structural cross-link in both the cuticle and the plaque. (C) Mussel inspired PEG-VO_2 NP hydrogel and film. (D) Schematic illustration of

the hydrogel structure, emphasizing the crosslinking of the PEG-DOPA polymer with VO_2 nanoparticles.

Mussels are renowned for employing metal coordination cross-links to enhance the mechanical strength of the protein-based byssal thread attachment fibers (Fig. 4.1A) .[18-20] Through this strong yet reversible chemistry, mussels create tough and self-healing fibers that can adhere to various surfaces underwater. Numerous studies have highlighted the role of 3,4-dihydroxyphenylalanine (DOPA) in achieving strong adhesion and mechanical robustness,[21, 22] through establishing coordination bonds with transition metal ions.[18, 23, 24] Although initial research suggested iron (Fe) as the key metal binding partner, recent studies revealed that V is the more commonly used metal crosslinker (Fig. 4.1B).[23, 25] Inspired by the mussel byssus, there have been numerous studies over the last decade on catechol-functionalized polymers crosslinked using transition metal ions to create self-healing soft materials[26-29]and adhesives for both dry and wet surfaces.[30, 31] More recently, researchers reported a method to prepare a nanocomposite hydrogel via mussel-inspired metal coordination, employing a catechol-functionalized polymer and iron oxide (Fe_3O_4) nanoparticles as building blocks.[32] Contrary to gels formed by cross-linking catechol ligands with metal ions, those crosslinked with nanoparticles demonstrated more solid-like yet still dynamic hydrogel mechanics.[32]

In this study, we report a novel method to fabricate dynamic hydrogels using VO_2 nanoparticles that can be processed into a stable, flexible, and elastomeric thermochromic films, utilizing mussel-inspired vanadium-catechol coordination chemistry (Fig. 4.1C). The resulting hydrogels show excellent dispersion of nanoparticles and demonstrated more solid-like behavior,

characterized by a slower relaxation rate compared to gels crosslinked with metals[29], while still maintaining the capacity for self-healing and thermochromic response. Moreover, films cast from the polymer-nanoparticle composite were flexible and extensible, with hydration-dependent mechanical response ranging elastomeric to thermoplastic-like. This method can be easily scaled, as it only requires mixing a catechol-functionalized polymer with VO_2 nanoparticles. This work emphasizes the need to tailor interactions between VO_2 nanoparticles and the polymer matrix, allowing for the fabrication of thermochromic materials with customizable mechanical properties and enduring stability.

4.4 Results and Discussion

4.4.1 Preparation of PEG-VO_2 Hydrogels and Films

Prior to the preparation of PEG-DOPA-VO_2 composites, a full characterization of the commercial VO_2 nanoparticles was carried out. This process was essential to determine their morphology, purity, and crystal phase. To verify the size and morphology of the VO_2 nanoparticles, we employed scanning electron microscopy (SEM), which showed that the nanoparticles exhibit a spherical morphology with a size range between 100-200 nm (Fig. 4.2A). The phase composition and crystallinity of the nanoparticles were characterized using powder x-ray diffraction (pXRD) (Fig. 4.5). The sample displayed characteristic diffraction peaks associated with the VO_2 (M1) phase (COD ID:3000344, P21/C, a=5.752316 Å; b=43525392 Å; c=5.382365 Å, α and γ= 90°, β=122.611°) with minimal impurity phases detected.[33] To assess the thermal stability and in the VO_2 nanoparticles, we conducted a thermogravimetric analysis (TGA) under ambient air conditions (Fig. 4.6). Upon heating from 0 °C to 150 °C, a 3% loss was detected due to the solvent

trapped in the nanoparticle sample. Since amorphous carbon combustion initiates at roughly 150 °C, the very small weight reduction (0.16 %) between 150 to 350 °C can be attributed to the loss of carbon in combustion. This was followed by a subsequent ~7.5% weight gain consistent with the oxidation of VO_2 into V_2O_5. Differential scanning calorimetry (DSC) was then employed to study the phase transition of VO_2 nanoparticles and pinpoint metal-insulator transition temperature (Fig. 4.2B). Notably, one peak was observed across the 0-90 °C temperature range, indicating a first-order phase transition. A small thermal hysteresis was observed between the heating and cooling curves, with a phase transition temperature T_c upon heating around 70.5°C, which aligns closely with reported values of 68 °C.[34, 35] This clearly shows the transition from the monoclinic insulator phase (M1) to the rutile metal phase (R) accompanied by the change of heat flow upon heating and cooling. Collectively, these measurements confirm the presence of pure VO_2 (M1) nanoparticles with a size that ranges between 100-200 nm that undergo reversible insulator-metal transition around 70 °C.

Composite PEG-DOPA-VO_2 hydrogels were formulated in a simple one step method – 1 wt% VO_2 nanoparticles were added to a 400 mg/ml solution of DOPA-functionalized 4-arm polyethylene glycol (4cPEG), which was prepared according to previous formulations (Fig. 4.2C).[36] This mixture underwent sonication to ensure a homogeneous distribution of nanoparticles within the solution. Subsequently, the pH was carefully adjusted to slightly above neutral using 1 M NaOH, which triggers instantaneous gelation into solid-like hydrogels that retain their structural integrity and shape at room temperature, in contrast with the more viscous response of gels from the identical polymer but with crosslinked soluble vanadium cations instead of nanoparticles (Fig. 4.2C). To prepare thermochromic and elastomeric PEG-DOPA-VO_2 films, the polymer-

nanoparticles mixture was spin-coated on plasma treated glass slide and baked in the oven overnight at 50 °C. When dried, the films were rigid, but still demonstrated notable flexibility (Fig. 4.2C). Upon hydration, the films swelled slightly, but stayed intact and appeared more flexible. Detailed mechanical characterization of hydrogels and films is described below.

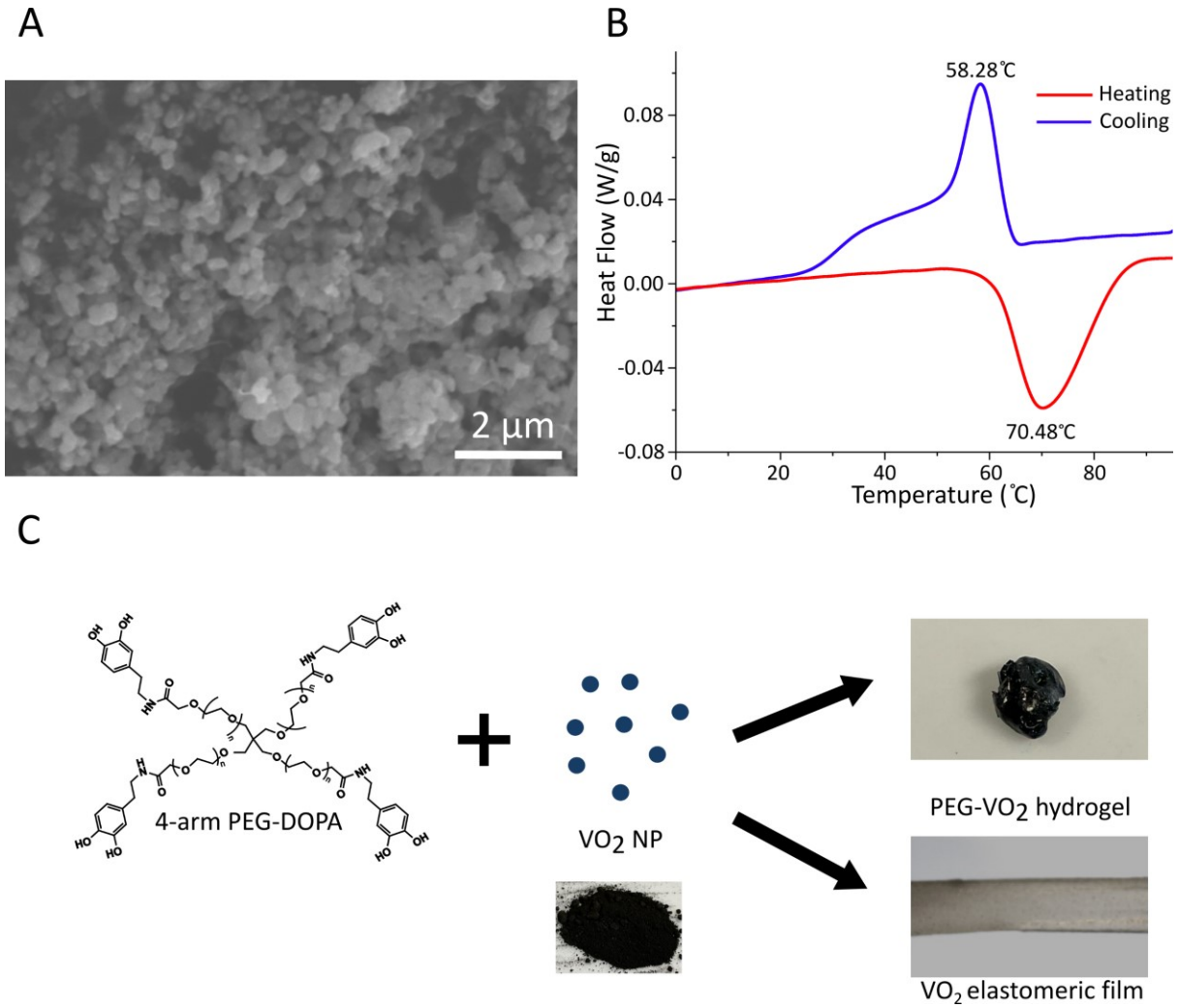

Figure 4.2 : Characterization of VO_2 nanoparticles and preparation of PEG-DOPA-VO_2 composite materials. (A) SEM image of VO_2 nanoparticles showing a size distribution between 100 and 200 nm. (B) DSC curves of VO_2 showing insulator-to metal phase transition upon the heating and cooling of the sample. (C) Preparation of VO_2 hydrogels and films from PEG-DOPA and VO_2 nanoparticles.

4.4.2 Characterization of PEG-DOPA-VO_2 Hydrogels

To investigate the nature of the bonds that stabilize the gel network , we utilized confocal Raman spectroscopy as it was previously shown to be an effective technique to characterize DOPA-metal coordination bonds in biological and synthetic materials (Fig. 4.3A).[25, 37] Indeed, Raman measurements of the PEG-DOPA-VO_2 hydrogels exhibited three characteristic Raman resonance peaks in the range of 500-700 cm^{-1} arising from metal-oxygen bond vibrations in bidentate catechol-metal complexes.[25] These peaks had nearly identical positions to those measured on a control hydrogel produced by crosslinking with V^{3+} metal ions as performed previously[23, 29] indicating similar coordination chemistry with a well-defined geometry, which is contrary to previously reported PEG-DOPA hydrogels crosslinked with iron oxide nanoparticles where a broad peak was observed in this region.[32]

The linkage of the DOPA moieties to the surfaces of the VO_2 NPs creates a hydrogel network in which many hundreds of PEG chains might be linked to the surface of a single NP. Drawing analogy to previous studies on hydrogels comprised of PEG-DOPA and iron oxide NPs, this is expected to significantly alter the viscoelastic response and relaxation behavior in comparison to hydrogels cross-linked simply with metal ions. To investigate the complex interplay between the polymer-NP interface crosslink dynamics and the bulk mechanical response of the hydrogel, we measured the rheological response of PEG-DOPA-VO_2 gels, in comparison to gels cross-linked with V^{3+} and those crosslinked covalently via oxidation of DOPA with $NaIO_4$.

Oscillatory frequency sweep experiments performed in the linear viscoelastic (LVE) region (1 % strain) reveal that all three gels have storage modulus (G') values in the range of 10^4 Pa, with the

covalently cross-linked gel having a slightly higher value (Fig. 4.3B). Covalent gels displayed a predominantly solid-like response, with the storage modulus G' significantly larger than the loss modulus G" across the entire frequency range examined, indicating little in the way of relaxation or damping behavior. In contrast and consistent with previous studies [32], PEG-DOPA-V^{3+} gels exhibited a much more fluid-like response at lower frequencies with a crossover point (G'= G") from solid to fluid-like response around 0.5 rad/s. As previously demonstrated, this arises from the transient and dynamic nature of catechol-V coordination bond, which is thought to break and reform on the scale of seconds at room temperature.[29] However, despite the transient nature of the DOPA-V cross-links at the surface of the NPs, the PEG-DOPA-VO_2 gels did not exhibit a crossover point in the frequency range examined, indicating a more solid-like behavior similar to what was observed previously with PEG-DOPA hydrogels crosslinked with Fe_3O_4 (Fig. 4.3B). This difference with metal ion cross-linked hydrogels was previously explained by the fact that a single metal ion would have a maximum three ligands connecting three chains, whereas a single NP could have hundreds of polymer chains attached to the surface.[32] Thus, even if some bonds break and reform on the scale of seconds, the polymer network remains largely intact without relaxing appreciably.

Nonetheless, stress relaxation experiments reveal that PEG-DOPA-VO_2 will relax significantly over longer timescales ($\tau \approx 212$ s) not probed by the frequency sweep experiments, indicating the dynamic nature of the bonding, which contrasts with the covalently cross-linked hydrogels which barely relax at all during the course of ~15 minutes due to the irreversible nature and the absence of any other relaxation pathways (Fig. 4.3C) The dynamic and reversible nature of the cross-linking in the PEG-DOPA-VO_2 hydrogels is further emphasized in strain pulse experiments that

demonstrate the self-healing nature of the gels. Indeed, applying a series of low (0.1%) and high 500% strain (Fig. 4.3D), we observed a more like a liquid-like behavior with G'' higher than G' at 500%; however, when the applied strain is reduced back to 0.1%, the gel restores its solid-like elasticity with G' exceeding G''. This effect was reproducible over numerous pulses of high and low strain. This demonstrates the reversibility and the self-healing capabilities of PEG-DOPA-VO_2 hydrogels.[38] Importantly, it emphasizes that the gel formation is not due to irreversible DOPA covalent crosslinks.

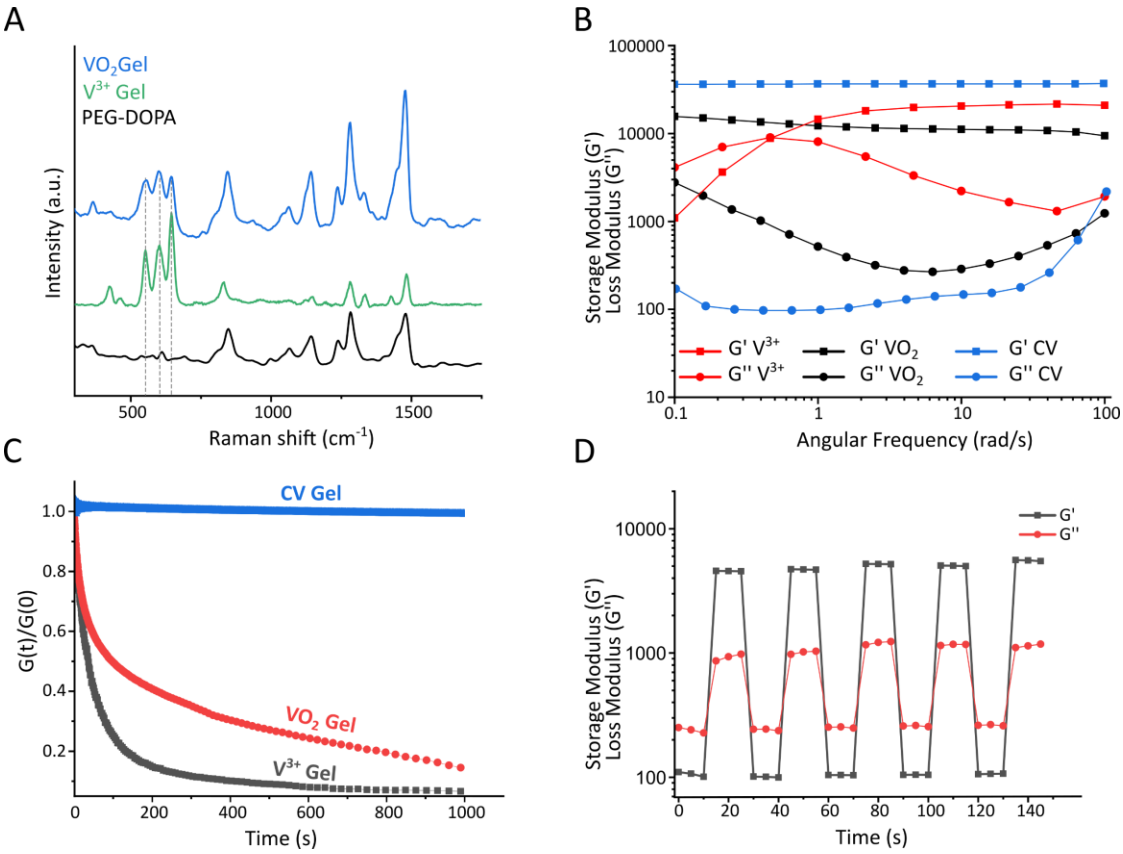

Figure 4.3: VO_2 gel spectroscopic and mechanical properties. (A) Comparative confocal Raman spectra of V^{3+} Gel, VO_2 (NP Gel), and CV Gel. (B) Frequency sweep at 1 % strain (within the linear viscoelastic range) of V^{3+} Gel, VO_2 (NP Gel), and CV Gel. (C) Comparative step- strain relaxation curves for V^{3+} Gel, VO_2 (NP Gel), and CV Gel. (D) Self-healing step-strain experiment between 1% and 500 % showing full recovery of the storage modulus.

4.4.3 Thermochromic Properties of Flexible VO_2 Polymeric Films

After evaluating the mechanical properties of the PEG-DOPA-VO_2 hydrogels, we attempted to prepare self-healing PEG-DOPA-VO_2 composite films with inherent thermochromic properties. As described above, VO_2 nanoparticles were dispersed in a PEG-DOPA solution, uniformly dispersed on a glass slide, and allowed to cure for 24 h at 50 °C. To probe the thermochromic properties of the prepared film, UV–VIS–NIR transmission spectra were collected for the PEG-DOPA-VO_2 composite films at two distinct temperatures (Fig. 4.4A). At 40 °C, which lies below the metal-insulator transition temperature (~68 °C), the film exhibited high transmittance in the NIR range, linked to the VO_2 maintaining its transparent rutile M1 phase. Conversely, as the temperature was raised to 80 °C, a noticeable drop in transmittance was observed, due to the phase transition of VO_2 nanoparticles to the reflective metallic M2 phase. The IR modulation, defined by the ability of the film to alter the transmission or reflection of infrared radiation in response to changes in temperature, was calculated to be 21.2% at 2000 nm. This shows that the thermochromic efficiency of the VO_2 nanoparticles was not affected when bound to the polymer.

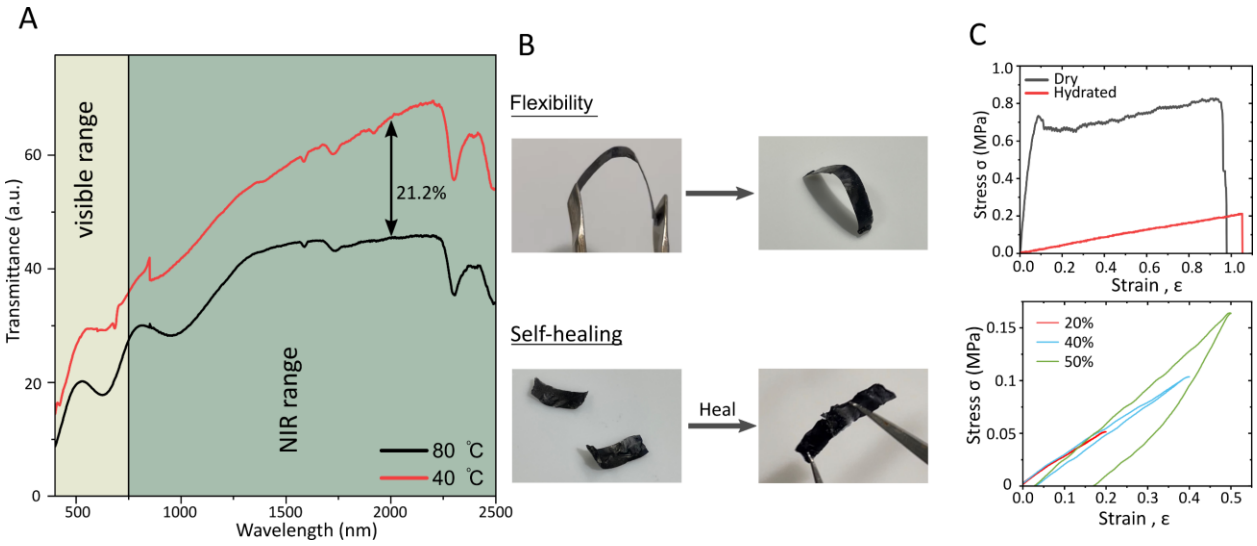

Figure 4.4: Thermochromic properties of VO_2/PEG-DOPA films. (A) Temperature-dependent UV-Vis–NIR transmission spectra of VO_2 polymeric film deposited on a glass slide. (B) Mechanical flexibility of VO_2 films under bending stress. Self-Healing capabilities of VO_2 polymeric films, demonstrated by rapid restoration post-cutting. (C) Stress-strain curve for Uniaxial tensile testing. Top graph shows two pull-to-break stress-strain curves for the dry and hydrated film. Bottom graph shows strain-history dependence with varying strain percentages.

These films can be easily formulated with different thickness and mechanical properties by controlling the polymer to NP ratio. The resulting films were found to be durable, withstanding different types of forces. To demonstrate how flexible the film is, it was subjected to multiple cycles of bending without showing any signs of permanent deformation or failure as shown in figure 4.4B. This flexibility is highly advantageous for diverse applications, such as flexible coatings for smart windows (Fig.4.4B).[39] Moreover, the obtained films exhibited self-healing properties, likely due to the reversible nature of DOPA-V bonds holding the network together. To demonstrate this ability, the film was sliced into two parts using a sharp blade. A small droplet of water was then applied to one end, and the other section was gently pressed against it. Within a

few seconds, self-healing was observed, as demonstrated by the fact that the mended film could be repeatedly stretched to ensure a robust bond.

The mechanical behavior of the films was tested using a tensile tester under both dry and wet conditions (Fig. 4.4C). In the dry state, the films exhibit plastic deformation with a clear yield point at ~10% strain followed by a post-yield plateau until failure at ~100% strain. Interestingly, hydrating the films resulted in a slight swelling and a much more elastomeric behavior with a lower stiffness and strength, but high resilience in cyclic loading and very little residual strain observed following loading up to < 40% strain. This versatile and robust mechanical response combined with thermochromic optical properties provides advantageous properties in comparison with current VO_2-based materials .[15] Overall, these findings shows that reversible DOPA-V interactions can be utilized to form a durable, flexible, and self-healing films without sacrificing the thermochromic properties of the nanoparticles. It is worth noting that the interactions between the polymer and the nanoparticles facilitated a uniform dispersion within the film. Consequently, we observed minimal to no nanoparticle clustering in the material.

4.5 Conclusion

This study presents a novel approach to creating flexible, durable, and efficient thermochromic materials inspired by the vanadium-catechol coordination in the mussel byssus cuticle. Our approach, which mimics the distinctive DOPA-V cross-link chemistry found in the adhesive fibers of marine mussels, offers a facile, low temperature process for creating VO_2 hydrogels and elastomeric films that maintain the inherent thermochromic properties of VO_2 nanoparticles. The

mechanical integrity self-healing nature of these films, demonstrated through rigorous mechanical testing, underscores their practicality and longevity, rendering them promising for real-world applications. Our straightforward approach preserves thermochromic qualities of VO_2, making it a practical choice for flexible, high-performance thermochromic materials, with broad potential applications. Our findings highlight the significant potential of employing bio-inspired coordination chemistry to advance the field of flexible thermochromic films.

4.6 Chemicals and Methods

Chemicals

All chemicals and solvents were used without undergoing additional further purification. Vanadium dioxide nanoparticles (100-200nm) were purchased from Guangzhou Hongwu Material Technology CO., LTD. 4-arm PEG-Sc, Mw 10KDa was purchased from Laysan Bio,inc. All other reagents and chemicals were procured from Millipore Sigma.

Synthesis and Characterization of 4-arm PEG-DOPA

The synthesis of 4-Arm PEG-DOPA was conducted using a modified protocol based on the approach described by Huang et al. Under a nitrogen atmosphere, a solution was prepared by dissolving 5 gram of 4-arm PEG succinimidyl carbonate (MW 10 KDa) in 40 ml of anhydrous N, N-dimethylformamide (DMF). Simultaneously, a solution of dopamine hydrochloride weighing 600 mg was dissolved in 40 ml of N,N-dimethylformamide (DMF) and afterwards neutralized with 0.6 ml of N-methylmorpholine. This neutralized solution was added to the PEG-SC solution after a

duration of 15 minutes. The reaction was conducted overnight under an inert nitrogen atmosphere. Following that, the product was subjected to a 24-hour process of dialysis against water that was buffered at a pH of 3.5. This was accomplished by using a dialysis membrane with a molecular weight cutoff of 3.5 kDa, obtained from Spectrum in Rancho Dominguez, CA. Subsequently, the substance underwent an additional 2-hour dialysis process using MQ water. After that, the solution was freeze-dried and stored at -20 °C under nitrogen to prevent catechol oxidization. Finally, the confirmation of functionalization was carried out using ^{1}H nuclear magnetic resonance spectroscopy. The two singlet peaks around 8.7 correspond to the two hydroxyl hydrogens of the catechol group indicating successful coupling (Fig. 4.7).

Preparation of Gels

VO_2 Gels and Films

VO_2 nanoparticle gel samples were prepared by mixing 100 µl of 4-arm-PEG-DOPA with 1 mg of VO_2 nanoparticles (100-200nm), and the pH was adjusted to 7, using 1 M NaOH. The sample was sonicated to allow homogenous distribution of the nanoparticles in the gel matrix, leading to instantaneous gelation. The pH of the resultant gel was measured using a Mettler Toledo Surface pH Electrode. For the preparation of film samples, 100 µl of 4-arm-PEG-DOPA was combined with 1 mg of VO_2 nanoparticles. After sonication, the mixture was evenly spread onto a slide and subsequently cured at 50 °C.

V^{3+} Gels

V^{3+} gel samples were prepared by mixing 200 µl of 4-arm-PEG-DOPA with 66 µl of 80 mM freshly prepared VCl_3 at a ratio of 3:1 of catechol to V^{3+}. After mixing, the pH was adjusted to 8 using 40 µL of 1M NaOH to form a dark blue elastic gel. The pH of the resultant gel was also measured using a Mettler Toledo Surface pH Electrode.

Covalently Crosslinked PEG-DOPA

Covalent gels were synthesized based on a published report, with minor modifications.[26] In an Eppendorf tube, 80 mM $NaIO_4$ was introduced to 400 µL of 4-arm-PEG-DOPA (1:2 molar ratio), followed by vigorous shaking. Subsequently, the tube was inverted, and its contents were allowed to cure at room temperature overnight, resulting in the formation of an amber-hued solid-like gel.

Nuclear Magnetic Resonance (NMR)

4-arm-PEG-dopa sample was prepared using deuterated Dimethyl sulfoxide (DMSO, 99.7% atom %, Sigma-Aldrich), and the spectrum was collected on a Bruker AVIIIHD 500 MHz NMR spectrometer.

Rheological Characterization

The rheological characteristics of the covalent, metal-crosslinked, and NP gels were assessed using an Anton Paar rheometer (MCR 302), equipped with a 15 mm cone-plate accessory (PP-15). Initially, the linear viscoelastic (LVE) range was determined by subjecting the sample to an

incremental strain from 0.1% to 100% and monitoring the values of the storage modulus (G') and the loss modulus (G''). After identifying the LVE range, frequency sweep tests were conducted, keeping a constant strain of 5% (Fig. 4.8) while varying the angular frequency from 0.1 rad/s to 100 rad/s. Subsequently, stress relaxation tests were performed using a 10% step strain (γ), and the relaxation modulus (G(t) = σ/γ) was continuously recorded throughout the test period. Each test was done three times on identical samples to validate reproducibility. A cyclic loading test involved subjecting the gel to a nonlinear regime, straining at γ = 500% at an oscillatory angular frequency of ω = 1 rad/s, leading to gel network failure. This was followed by subjecting the gel to a small strain within the LVE range while monitoring the recovery of the storage modulus (G'). The temperature during measurements was maintained at a constant 24 °C using a Peltier unit. To prevent evaporation, a solvent trap was employed throughout all test procedures.

Raman Spectroscopic Measurements

Raman spectroscopic measurements were conducted on thin dried hydrogel samples mounted on quartz slides using a confocal Raman microscope (Alpha 300R, WITec). A 785-nm near infrared (NIR) laser, operating at a power ranging between 20 and 30 mW, was focused on the sample using a 50× objective (Zeiss, numerical aperture [NA] = 0.9). Spectra were obtained using a thermoelectrically cooled CCD detector, using a 600-g/mm grating. Each spectrum is an average of 50 accumulations with 1 s integration time. Data was collected using WITec ControlFIVE 5.1 software and subsequent processing, such as cosmic ray removal and background signal subtraction, was performed using WITec Plus software. Spectra were finally smoothed using Savitzky-Golay smoothing filter.

Scanning Electron Microscopy (SEM)

For SEM analysis, samples were characterized using a Hitachi SU3500 scanning electron microscope at 30 keV.

UV-Vis-NIR Spectroscopy

To characterize the thermochromic properties of the polymeric films, absorption spectra at different temperatures were collected using Jasco V-670 UV-Vis-NIR spectrometer equipped with a Peltier temperature control unit.

Mechanical Testing

The mechanical properties of the samples were evaluated using a CellScale UStretch tensile tester, equipped with a load cell of 0.5 N capacity. Additionally, a video was captured utilizing a camera featuring a 1/2-inch monochrome CCD sensor, which provided a resolution of 1280x960 pixels.

Powder X-ray Diffraction and Thermal Gravimetric Analysis (TGA)

The powder x-ray diffraction pattern of VO2 nanoparticles was recorded on a Bruker D8 advance diffractometer equipped with Cu Kα radiation (λ = 1.5406 Å), With 2θ ranging between 10° and 70°. While thermogravimetric analysis (TGA) was obtained under air using Metler Toledo TGA/DSC1 instrument, employing a heat rate of 2 °C per minute from 0 °C to 800 °C.

4.7 Supplementary Information

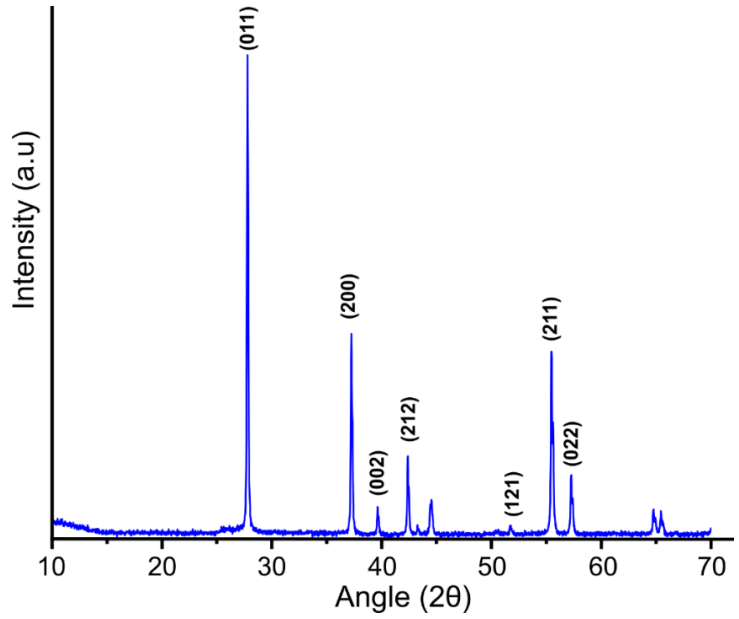

Figure 4.5: Powder X-ray diffraction pattern of VO_2 nanoparticles showing a pure M1 phase.

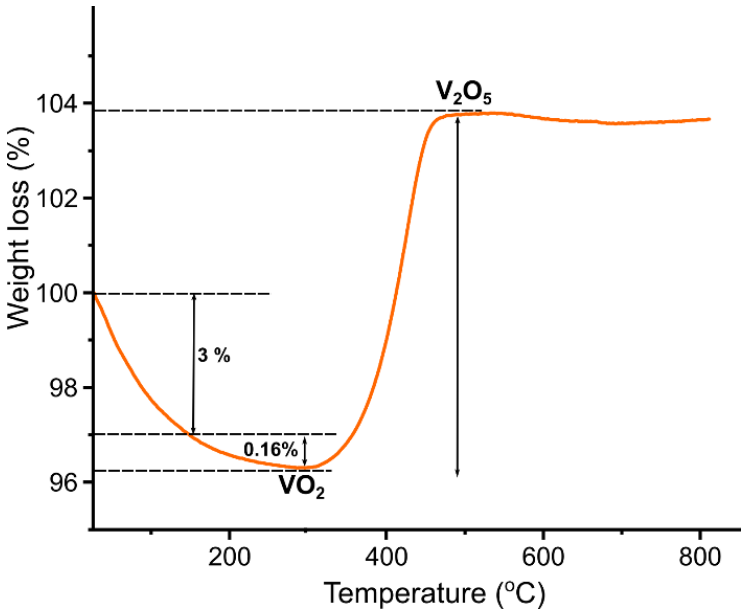

Figure 4.6: Thermogravimetric analysis of VO_2 nanoparticles conducted under air.

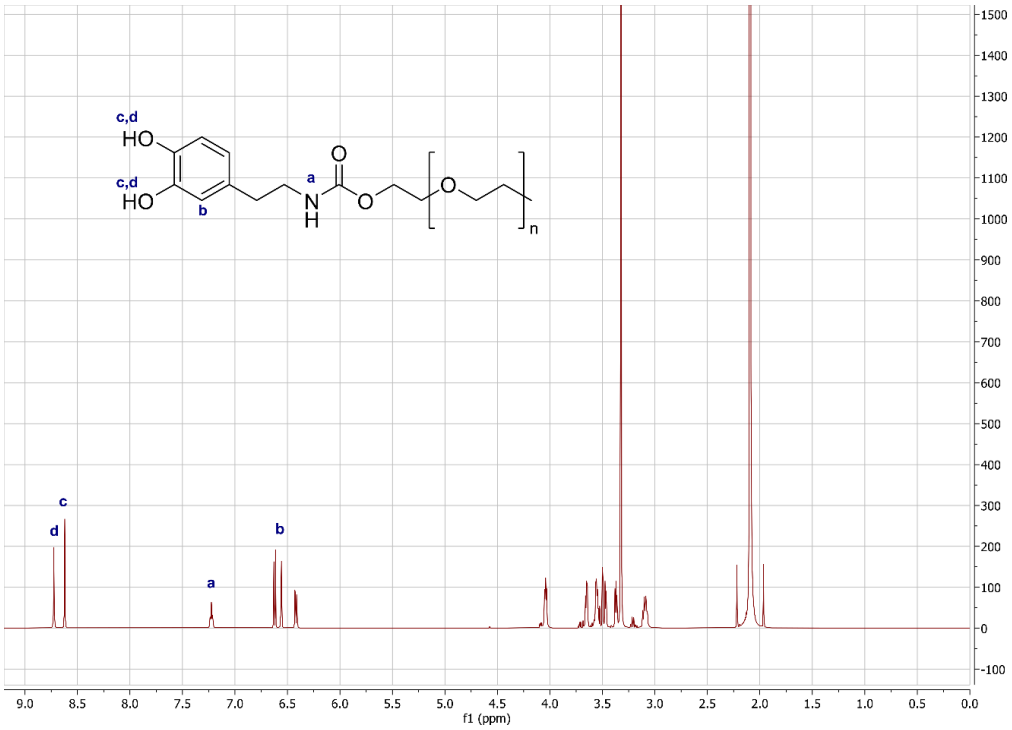

Figure 4.7: ^{1}H NMR spectrum of 4cPEG-DOPA.

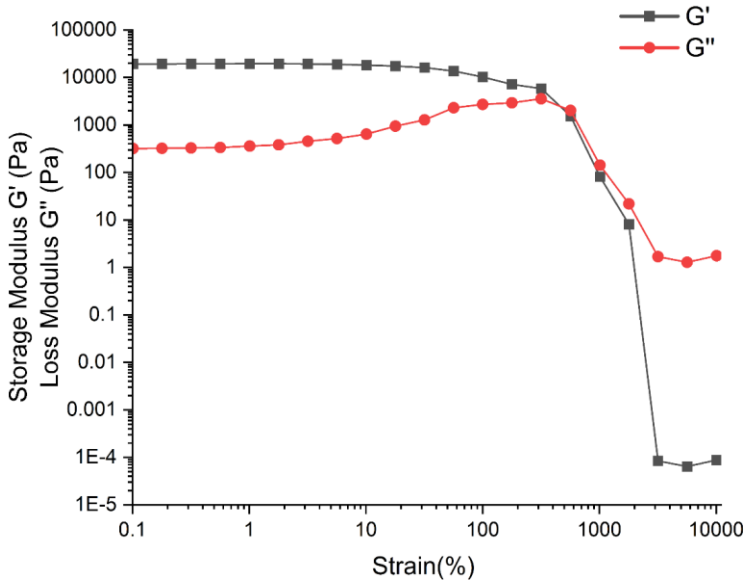

Figure 4.8: Amplitude sweep of PEG-DOPA-VO_2 hydrogel.

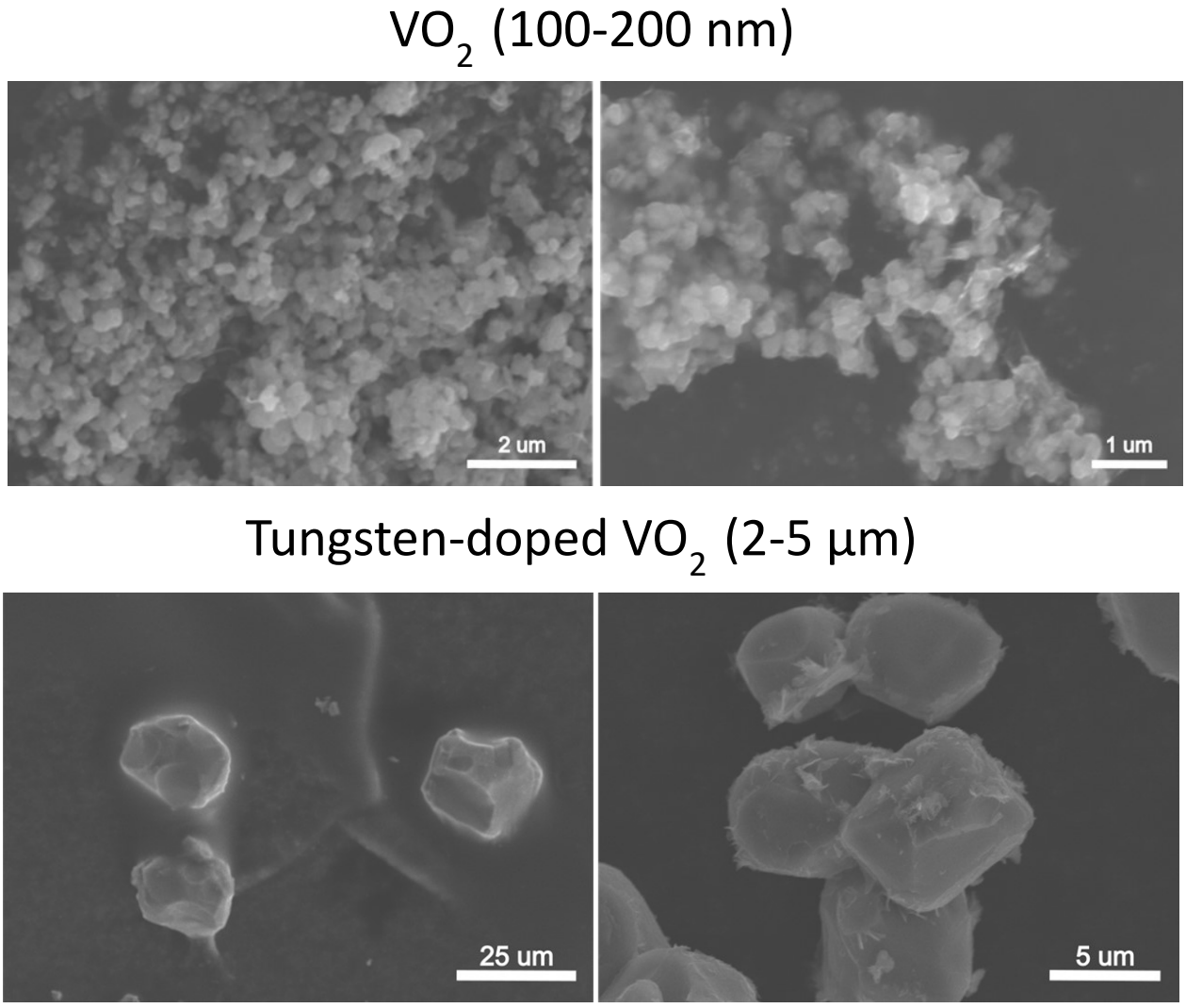

Figure 4.9: SEM images of VO_2 nanoparticles and tungsten-doped VO_2. Doping lead to an increase in crystal size which was not optimal for our applications.

4.8 References

1. Chang, T.-C.; Cao, X.; Bao, S.-H.; Ji, S.-D.; Luo, H.-J.; Jin, P., Review on thermochromic vanadium dioxide based smart coatings: from lab to commercial application. *Advances in Manufacturing* **2018,** *6* (1), 1-19.

2. Hu, L.; Tao, H.; Chen, G.; Pan, R.; Wan, M.; Xiong, D.; Zhao, X., Porous W-doped VO2 films with simultaneously enhanced visible transparency and thermochromic properties. *Journal of Sol-Gel Science and Technology* **2016,** *77* (1), 85-93.

3. Mai, L. Q.; Hu, B.; Hu, T.; Chen, W.; Gu, E. D., Electrical Property of Mo-Doped VO2 Nanowire Array Film by Melting−Quenching Sol−Gel Method. *The Journal of Physical Chemistry B* **2006,** *110* (39), 19083-19086.

4. Piccirillo, C.; Binions, R.; Parkin, I. P., Nb-Doped VO2 Thin Films Prepared by Aerosol-Assisted Chemical Vapour Deposition. *European Journal of Inorganic Chemistry* **2007,** *2007* (25), 4050-4055.

5. Li, G.; Xie, D.; Zhang, Z.; Zhou, Q.; Zhong, H.; Ni, H.; Wang, J.; Guo, E.-j.; He, M.; Wang, C.; Yang, G.; Jin, K.; Ge, C., Flexible VO2 Films for In-Sensor Computing with Ultraviolet Light. *Advanced Functional Materials* **2022,** *32* (29), 2203074.

6. Chang, T.; Zhu, Y.; Huang, J.; Luo, H.; Jin, P.; Cao, X., Flexible VO2 thermochromic films with narrow hysteresis loops. *Solar Energy Materials and Solar Cells* **2021,** *219*, 110799.

7. Shen, N.; Chen, S.; Huang, R.; Huang, J.; Li, J.; Shi, R.; Niu, S.; Amini, A.; Cheng, C., Vanadium dioxide for thermochromic smart windows in ambient conditions. *Materials Today Energy* **2021,** *21*, 100827.

8. Elango, P. F. M.; Kabir, S.; Kechanda Prasanna, P.; Low, M. X.; Yang, M.; Chakraborty, S.; Walia, S.; Sriram, S.; Bhaskaran, M., Vanadium Dioxide-Based Miniaturized Thermal Sensors: Humidity Effects on Phase Change and Sensitivity. *ACS Applied Electronic Materials* **2022,** *4* (11), 5456-5467.

9. Rahman, M. A.; Walia, S.; Naznee, S.; Taha, M.; Nirantar, S.; Rahman, F.; Bhaskaran, M.; Sriram, S., Artificial Somatosensors: Feedback Receptors for Electronic Skins. *Advanced Intelligent Systems* **2020,** *2* (11), 2000094.

10. Chandra, S.; Franklin, D.; Cozart, J.; Safaei, A.; Chanda, D., Adaptive Multispectral Infrared Camouflage. *ACS Photonics* **2018,** *5* (11), 4513-4519.

11. Barimah, E. K.; Boontan, A.; Steenson, D. P.; Jose, G., Infrared optical properties modulation of VO2 thin film fabricated by ultrafast pulsed laser deposition for thermochromic smart window applications. *Scientific Reports* **2022,** *12* (1), 11421.

12. Vernardou, D.; Louloudakis, D.; Spanakis, E.; Katsarakis, N.; Koudoumas, E., Thermochromic amorphous VO2 coatings grown by APCVD using a single-precursor. *Solar Energy Materials and Solar Cells* **2014,** *128*, 36-40.

13. de Castro, M. S. B.; Ferreira, C. L.; de Avillez, R. R., Vanadium oxide thin films produced by magnetron sputtering from a V2O5 target at room temperature. *Infrared Physics & Technology* **2013,** *60*, 103-107.

14. Cao, X.; Chang, T.; Shao, Z.; Xu, F.; Luo, H.; Jin, P., Challenges and Opportunities toward Real Application of VO₂-Based Smart Glazing. *Matter* **2020,** *2* (4), 862-881.

15. Kabir, S.; Yang, D.; Ahmad Kayani, A. B.; Zhang, H.; Nirantar, S.; Sriram, S.; Walia, S.; Bhaskaran, M., Solution-Processed VO2 Nanoparticle/Polymer Composite Films for Thermochromic Applications. *ACS Applied Nano Materials* **2022,** *5* (8), 10280-10291.

16. Chang, T.; Cao, X.; Li, N.; Long, S.; Zhu, Y.; Huang, J.; Luo, H.; Jin, P., Mitigating Deterioration of Vanadium Dioxide Thermochromic Films by Interfacial Encapsulation. *Matter* **2019,** *1* (3), 734-744.

17. Chen, Y.; Fan, L.; Fang, Q.; Xu, W.; Chen, S.; Zan, G.; Ren, H.; Song, L.; Zou, C., Free-standing SWNTs/VO2/Mica hierarchical films for high-performance thermochromic devices. *Nano Energy* **2017,** *31*, 144-151.

18. Harrington, M. J.; Masic, A.; Holten-Andersen, N.; Waite, J. H.; Fratzl, P., Iron-Clad Fibers: A Metal-Based Biological Strategy for Hard Flexible Coatings. *Science* **2010,** *328* (5975), 216-220.

19. Holten-Andersen, N.; Mates, T. E.; Toprak, M. S.; Stucky, G. D.; Zok, F. W.; Waite, J. H., Metals and the Integrity of a Biological Coating: The Cuticle of Mussel Byssus. *Langmuir* **2009,** *25* (6), 3323-3326.

20. Schmitt, C. N. Z.; Politi, Y.; Reinecke, A.; Harrington, M. J., Role of Sacrificial Protein–Metal Bond Exchange in Mussel Byssal Thread Self-Healing. *Biomacromolecules* **2015,** *16* (9), 2852-2861.

21. Waite, J. H.; Tanzer, M. L., Polyphenolic Substance of Mytilus edulis: Novel Adhesive Containing L-Dopa and Hydroxyproline. *Science* **1981,** *212* (4498), 1038-1040.

22. Lee, H.; Scherer, N. F.; Messersmith, P. B., Single-molecule mechanics of mussel adhesion. *Proceedings of the National Academy of Sciences* **2006,** *103* (35), 12999-13003.

23. Mesko, M.; Xiang, L.; Bohle, S.; Hwang, D. S.; Zeng, H.; Harrington, M. J., Catechol-Vanadium Binding Enhances Cross-Linking and Mechanics of a Mussel Byssus Coating Protein. *Chemistry of Materials* **2021,** *33* (16), 6530-6540.

24. Jehle, F.; Macías-Sánchez, E.; Sviben, S.; Fratzl, P.; Bertinetti, L.; Harrington, M. J., Hierarchically-structured metalloprotein composite coatings biofabricated from co-existing condensed liquid phases. *Nature Communications* **2020,** *11* (1), 862.

25. Priemel, T.; Palia, G.; Förste, F.; Jehle, F.; Sviben, S.; Mantouvalou, I.; Zaslansky, P.; Bertinetti, L.; Harrington, M. J., Microfluidic-like fabrication of metal ion–cured bioadhesives by mussels. *Science* **2021,** *374* (6564), 206-211.

26. Holten-Andersen, N.; Harrington, M. J.; Birkedal, H.; Lee, B. P.; Messersmith, P. B.; Lee, K. Y. C.; Waite, J. H., pH-induced metal-ligand cross-links inspired by mussel yield self-healing polymer networks with near-covalent elastic moduli. *Proceedings of the National Academy of Sciences* **2011,** *108* (7), 2651-2655.

27. Wang, X.; Jiang, Z.; Shi, J.; Zhang, C.; Zhang, W.; Wu, H., Dopamine-Modified Alginate Beads Reinforced by Cross-Linking via Titanium Coordination or Self-Polymerization and Its Application in Enzyme Immobilization. *Industrial & Engineering Chemistry Research* **2013,** *52* (42), 14828-14836.

28. Krogsgaard, M.; Behrens, M. A.; Pedersen, J. S.; Birkedal, H., Self-Healing Mussel-Inspired Multi-pH-Responsive Hydrogels. *Biomacromolecules* **2013,** *14* (2), 297-301.

29. Holten-Andersen, N.; Jaishankar, A.; Harrington, M. J.; Fullenkamp, D. E.; DiMarco, G.; He, L.; McKinley, G. H.; Messersmith, P. B.; Lee, K. Y. C., Metal-coordination: using one of nature's

tricks to control soft material mechanics. *Journal of Materials Chemistry B* **2014,** *2* (17), 2467-2472.

30. Lee, H.; Lee, B. P.; Messersmith, P. B., A reversible wet/dry adhesive inspired by mussels and geckos. *Nature* **2007,** *448* (7151), 338-341.

31. Hu, Z.; Wu, W.; Yu, M.; Wang, Z.; Yang, Z.; Xing, X.; Chen, X.; Niu, L.; Yu, F.; Xiao, Y.; Chen, J., Mussel-inspired polymer with catechol and cationic Lys functionalities for dentin wet bonding. *Materials Today Bio* **2023,** *18*, 100506.

32. Li, Q.; Barrett, D. G.; Messersmith, P. B.; Holten-Andersen, N., Controlling Hydrogel Mechanics via Bio-Inspired Polymer–Nanoparticle Bond Dynamics. *ACS Nano* **2016,** *10* (1), 1317-1324.

33. Wilson, C. E.; Gibson, A. E.; Cuillier, P. M.; Li, C.-H.; Crosby, P. H. N.; Trigg, E. B.; Najmr, S.; Murray, C. B.; Jinschek, J. R.; Doan-Nguyen, V., Local structure elucidation of tungsten-substituted vanadium dioxide. *Scientific Reports* **2022,** *12* (1), 14767.

34. Victor, J.-L.; Gaudon, M.; Salvatori, G.; Toulemonde, O.; Penin, N.; Rougier, A., Doubling of the Phase Transition Temperature of VO2 by Fe Doping. *The Journal of Physical Chemistry Letters* **2021,** *12* (32), 7792-7796.

35. Liu, M.; Sternbach, A. J.; Wagner, M.; Slusar, T. V.; Kong, T.; Bud'ko, S. L.; Kittiwatanakul, S.; Qazilbash, M. M.; McLeod, A.; Fei, Z.; Abreu, E.; Zhang, J.; Goldflam, M.; Dai, S.; Ni, G.-X.; Lu, J.; Bechtel, H. A.; Martin, M. C.; Raschke, M. B.; Averitt, R. D.; Wolf, S. A.; Kim, H.-T.; Canfield, P. C.; Basov, D. N., Phase transition in bulk single crystals and thin films of by nanoscale infrared spectroscopy and imaging. *Physical Review B* **2015,** *91* (24), 245155.

36. Huang, W.-C.; Ali, F.; Zhao, J.; Rhee, K.; Mou, C.; Bettinger, C. J., Ultrasound-Mediated Self-Healing Hydrogels Based on Tunable Metal–Organic Bonding. *Biomacromolecules* **2017,** *18* (4), 1162-1171.

37. Zvarec, O.; Purushotham, S.; Masic, A.; Ramanujan, R. V.; Miserez, A., Catechol-Functionalized Chitosan/Iron Oxide Nanoparticle Composite Inspired by Mussel Thread Coating and Squid Beak Interfacial Chemistry. *Langmuir* **2013,** *29* (34), 10899-10906.

38. Mealy, J. E.; Chung, J. J.; Jeong, H.-H.; Issadore, D.; Lee, D.; Atluri, P.; Burdick, J. A., Injectable Granular Hydrogels with Multifunctional Properties for Biomedical Applications. *Advanced Materials* **2018,** *30* (20), 1705912.

39. Kim, H.; Kim, Y.; Kim, K. S.; Jeong, H. Y.; Jang, A. R.; Han, S. H.; Yoon, D. H.; Suh, K. S.; Shin, H. S.; Kim, T.; Yang, W. S., Flexible Thermochromic Window Based on Hybridized VO2/Graphene. *ACS Nano* **2013,** *7* (7), 5769-5776.

Chapter 5：DOPA-Rich Mussel Byssus Peptide Initiates V- and Fe-Coordinated Gelation at Low pH

5.1 Preface

So far, we have shown two examples of how mussel-inspired metal coordination can help build high performance hydrogel materials. In **Chapter 3**, we developed microgels functionalized with peptides inspired by the histidine-rich cross-linking domains of marine mussel byssus proteins. Functionalized microgels can reversibly aggregate *in situ* via metal coordination cross-linking to form microporous, self-healing, and resilient scaffolds at physiological conditions by inclusion of minimal amounts of zinc ions at basic pH. In **Chapter 4**, we pioneered a room-temperature process to fabricate thermochromic VO_2 hydrogels and elastomeric films, inspired by the vanadium-catechol coordination chemistry that mussels use to produce high-performance adhesive fibers.

Chapter 5 reveals the significant influence of the protein sequence on DOPA's metal chelation behavior. Comparative analysis shows superior metal binding at lower pH values for DOPA-rich peptides compared to DOPA-functionalized polymers. Leveraging the enhanced interaction between catechol and iron in physiological environments, we created an injectable granular system through the integration of mfp1 peptides onto the microgels. These microgels can undergo crosslinking, forming a porous and self-healing scaffold in the presence of iron at neutral pH levels.

This chapter is the subject of a manuscript in preparation under the title "**DOPA-Rich Mussel Byssus Peptide Initiates V- and Fe- Coordinated Gelation at Low pH"** by Mostafa Rammal, Matthew Harrington.

5.2 Abstract

Drawing inspiration from the chemical mechanisms found within the byssus fibers of marine mussels, coordination between 3,4-dihydroxyphenylalanine (DOPA) and metals has emerged as a powerful crosslinking strategy for creating a diverse array of high-performance supramolecular polymers and adhesives. These materials exhibit excellent mechanical properties, owing to the reversible yet strong catechol-metal coordinate bonds. Despite these remarkable properties and adaptability across diverse applications, synthetic mussel-inspired polymers still fall short in terms of matching the overall performance of the natural system. Apart from the structural complexity of the natural system, this discrepancy arises from the reductionist approach employed to create mussel-inspired polymeric materials. This method involves isolating the DOPA moiety from its natural sequence and grafting it onto various polymers, thereby removing it from its native biochemical context. Recent studies have explored the role of the sequence on the metal chelation behavior of DOPA, revealing striking differences between the performance of synthetic and natural systems – using DOPA within its native peptide sequence enhanced metal binding at lower pH levels, particularly vanadium, broadening the scope of potential applications for these materials. Here, we utilized a synthetic peptide derived from the DOPA-rich mfp1 protein present in the byssus to fabricate supramolecular hydrogels with enhanced properties compared with their synthetic counterparts. Taking advantage of the enhanced catechol-iron complexation at physiological conditions, we formulated an injectable microporous annealed scaffold using mfp1-functionalized microgels. Due to the demonstrated cytocompatibility, this system holds the potential for future tissue repair applications.

5.3 Introduction

Marine mussels utilize catechol moieties from 3,4-dihydroxyphenylalanine (DOPA) to achieve strong underwater adhesion and fabricate tough and self-healing biopolymer fibers and coatings.[1-3] Investigations have showcased how DOPA's coordination with metals like iron and vanadium enhances the mechanical attributes of the cuticle—an outer protective e layer enveloping mussel byssal threads (Fig. 5.1B).[4-8] The cuticle exhibits extraordinary hardness and stiffness while preserving an unexpected level of flexibility—a unique combination rarely seen in synthetic materials. Various research groups have endeavored to replicate the mechanical and adhesive properties of mussel proteins using synthetic polymers. These efforts have involved the synthesis of polymeric systems through the integration of DOPA into synthetic polymer structures within in the backbone, side chains, or terminal groups.[9-12] Since the pioneering studies by Holten-Andersen and coworkers over a decade ago [13], the field of mussel-inspired DOPA-metal coordination polymers has expanded significantly. Thousands of publications and investigations have leveraged DOPA-metal coordination for the development of a wide array of catechol-functionalized polymers. These materials have found applications in self-healing hydrogels, multifunctional coatings, and surgical adhesives (Fig. 5.1D).[13-16] However, these catechol polymeric systems still face major challenges, such as the inability to form strong coordinate bonds at physiologically relevant values, limiting their biological applications. Moreover, the necessity to elevate the pH hastens the oxidation process of DOPA moieties, detrimentally impacting the mechanical properties of these materials such as the loss of self-healing capabilities.[13] For instance, in the case of catechol-functionalized polyethylene glycol PEG-DOPA polymer, achieving tris coordination with iron demands raising the pH to 12 which

increases the likelihood of DOPA oxidation (Fig. 5.1D).[13, 17] However, recent studies have shown that recombinant mfp-1 protein binds metal ions at a much lower pH than pure catechol, leading to the hypothesis that specific features of the native sequence might function to enhance metal binding during the low pH formation process .[18-20] In particular, this sequence was highly effective at creating interactions with vanadium ions, which have also been identified as a key cross-linking metal in the native byssus materials.[18, 19] This highlights the substantial influence that the protein sequence can have on the metal-binding behavior of DOPA and the resulting mechanical stability of the cross-linking involved. Isolating DOPA from its native context within bioinspired polymeric systems may lead to missing out on numerous advantages associated with DOPA's capabilities. Herein, we explored the potential for creating self-healing catechol-based metallopolymer gels under acidic and physiological pH conditions (Fig. 5.1F-H). This was achieved by employing a synthetic DOPA-containing peptide sequence derived from the mfp-1 protein, mainly found in the cuticle.[21, 22] This peptide (mfp1) enables multivalent cross-linking with both Fe and V, resulting in enhanced elasticity and slower relaxation compared to the highly viscous behavior observed in PEG-DOPA under similar conditions (Fig. 5.1F-G). Taking advantage of this enhanced binding at physiological pH, we developed an injectable granular system by integrating mfp1 peptide into microgels. Functionalized microgels can be reversibly annealed via metal coordination to form a microporous, resilient, and self-healing scaffold (Fig. 5.1H). Given the demonstrated cytocompatibility of these annealed granular hydrogel scaffolds, we believe that these materials hold promising potential for advancement in regenerative medicine applications.[23]

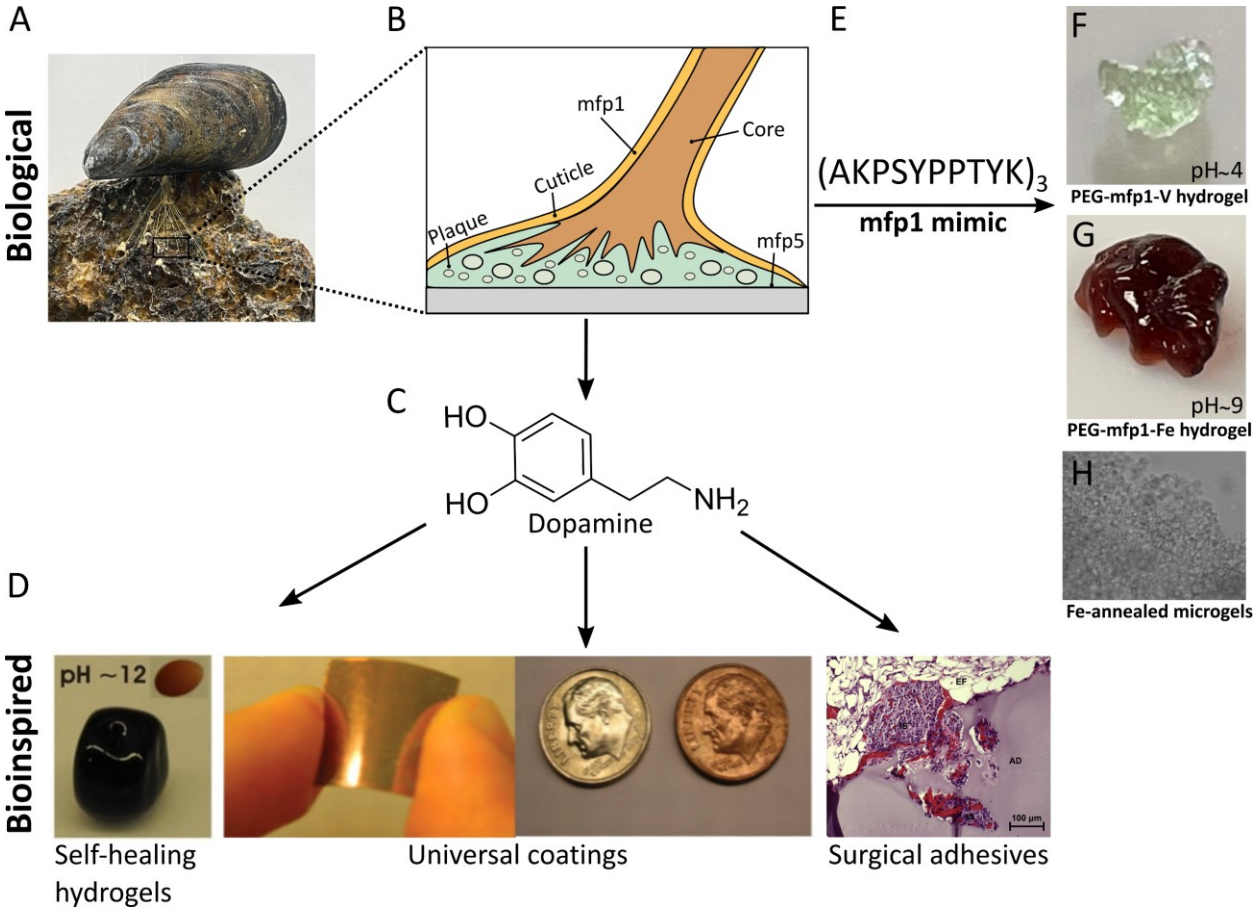

Figure 5.1: The influence of protein the sequence on DOPA's metal chelation behavior. (A) Mussel attached to a rock using multiple byssal threads. (B) Schematic depiction of the byssus, emphasizing its three primary components (core, cuticle, and plaque), alongside the two key DOPA-rich proteins that have been influential in inspiring various materials. (C) Dopamine molecule, the main building block that inspired countless applications. (D) Using DOPA as a crosslinking building block allowed the engineering of several materials with unique properties, such as self-healing hydrogels[13], multifunctional coatings[24], and surgical adhesives.[25](E) Using DOPA in its natural sequence can have a substantial effect on the metal chelation behavior yielding hydrogels that exhibit slower relaxation and can form at acidic pH values. (F) Vanadium can crosslink PEG-mfp1 into a stiff hydrogel at pH=4. (G) PEG-mfp1 forms tris coordination with iron at pH=9 substantially lower than PEG-$DOPA_4$ (pH=12) (Fig. 5.1D). (H) Mfp1-functionalized microgels crosslinked with iron at pH=7.4.

5.4 Results and Discussions

5.4.1 Synthesis of PEG-Mfp1 and PEG-DOPA Conjugates

Mfp1 peptide, comprised of 3 repeats of **AKPSY*PPTY*K** (where **Y*** is DOPA), was manually synthesized via solid-phase peptide synthesis utilizing Fmoc chemistry and HCTU coupling strategy. A cysteine residue was introduced at the N-terminus to allow for thiol-maleimide Michael addition to the PEG chain (Fig. 5.7). In a phosphate-buffered saline, the peptide was coupled to a 4-arm PEG-maleimide, and successful functionalization was assessed using nuclear magnetic resonance spectroscopy (Fig. 5.8). Following a previous protocol, PEG-DOPA, a 4 arm PEG polymer terminated with 4 catechol groups, was synthesized by reacting Dopamine hydrochloride with 4-arm PEG-NHS (more detailed protocol can be found in the methods section) (Fig. 5.9).

5.4.2 pH-Dependent UV-Vis Spectra of Metal Binding by PEG-Mfp1 vs PEG-DOPA

To gain initial insights into the contrasting metal chelation behaviors of isolated DOPA versus DOPA within the native mfp1 sequence, we carried out a comparative UV−Vis spectroscopic analysis involving PEG-mfp1 and PEG-DOPA (Fig. 5.2). This involved examining solutions of both systems combined with Fe and V solutions across various pH values ranging from ~3 to 12. UV−Vis spectroscopy is a powerful analytical technique for differentiating diverse binding states of catechol-containing compounds with various metals. These interactions often manifest distinctive charge transfer bands, exhibiting discernible spectral characteristics for mono, bis, and tris coordination of catechol−Fe and catechol−V metal complexes.[13, 26] UV-Vis

spectra were taken after mixing both systems having equal catechol concentrations with Fe^{III} and V^{III} in a stoichiometric ratio of 1 metal: 3 DOPA groups.

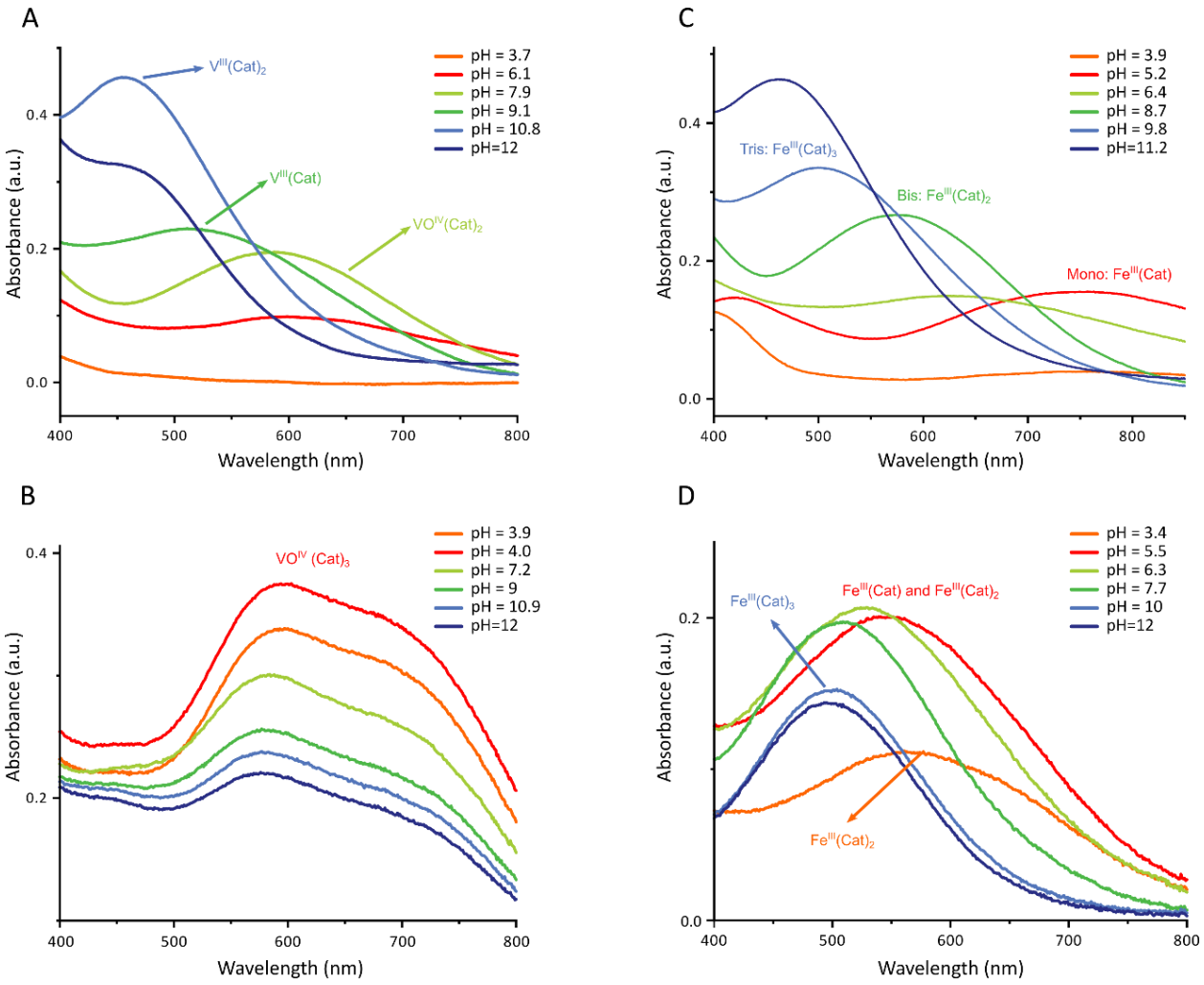

Figure 5.2: pH-dependent UV–Vis spectra of metal binding by PEG-mfp1 vs PEG-DOPA. All titrations were done starting with the same concentration of DOPA and the ratio of metal to DOPA was maintained at 1:3. (A) and (B) Titration curves of PEG-DOPA and PEG-mfp1 with VCl_3 respectively showing the complexes formed at representative pH values. (C) and (B) Titration curves of PEG-DOPA and PEG-mfp1 with $FeCl_3$ respectively highlighting dominant complexes at selected pH values.

The spectra revealed distinct signals representing mono, bis, or tris complex formations between catechols and the metal ions (V, Fe) present in the solution and the transition pH values (Fig. 5.2). Starting with PEG-DOPA with vanadium (Fig. 5.2A), no significant catechol-V coordination is observed at acidic pH values. As the pH is raised, VO^{IV} starts forming bis coordination bonds reaching a max at pH= 7.9. Above pH=10, V^{III}(Cat) is observed; however, its intensity begins to decrease as the pH increases most probably due to the oxidation of the catechol groups. On the other hand, PEG-mfp1 conjugate clearly forms tris DOPA−V(IV) complexation characterized by the presence of two peaks and a high extinction coefficient, aligning with earlier reports, using 12 repeats of the same sequence (Fig. 5.2B).[20] This further highlights the sequence preference for binding V metal at low pH values.

Examining the spectra of PEG-mfp1 and PEG-DOPA with iron, we also see clear differences in the complexes formed at different pH values. For PEG-DOPA, mono coordination prevails at acidic pH value, transitioning to bis coordination around 6.4 and becoming predominant around pH=8.7. Tris complexes form above 9.8 and reach the maximum intensity at pH=11.2 (Fig. 5.2C). This observation explains the need to raise the pH to extremely high values in order to form elastic PEG-DOPA hydrogels.[13] The necessity of elevating the pH to extremely high levels has restricted the utilization of metal crosslinked DOPA systems in biological applications, leading to a shift towards employing covalently crosslinked catechol systems instead.[27, 28]. However, PEG-mfp1 is able to form bis complexes at acidic pH values as low as 3.4 with tris complex forming around neutral pH values ~6.3 and reaching maximum intensity around pH=10 (Fig. 5.2D). This is

relevant for both metals as there is growing evidence that cuticle proteins are stored at acidic pH values before secretion.[29, 30] These striking differences in metal chelation between both conjugates highlight the role of sequence and shows why taking DOPA out of its evolved biochemical context can lead to the loss of several inherent properties. After the characterization of metal coordination for both systems, we attempted to prepare hydrogels using both polymers at different pH values and characterize their rheological properties.

5.4.3 Preparation and Characterization of DOPA-Crosslinked Hydrogels

The two polymers were crosslinked separately with iron and vanadium at varying pH levels to create hydrogels. In a simple two-step process, PEG-mfp1 or PEG-DOPA solution was mixed with an 80 mM metal solution (Fe or V) at a ratio of 1 metal: 3 DOPAs, followed by the addition of NaOH to reach the desired pH value. Following gel preparation, frequency sweep tests were performed on the samples to characterize their elastic and relaxation properties at different timescales (Fig. 5.3B-C).

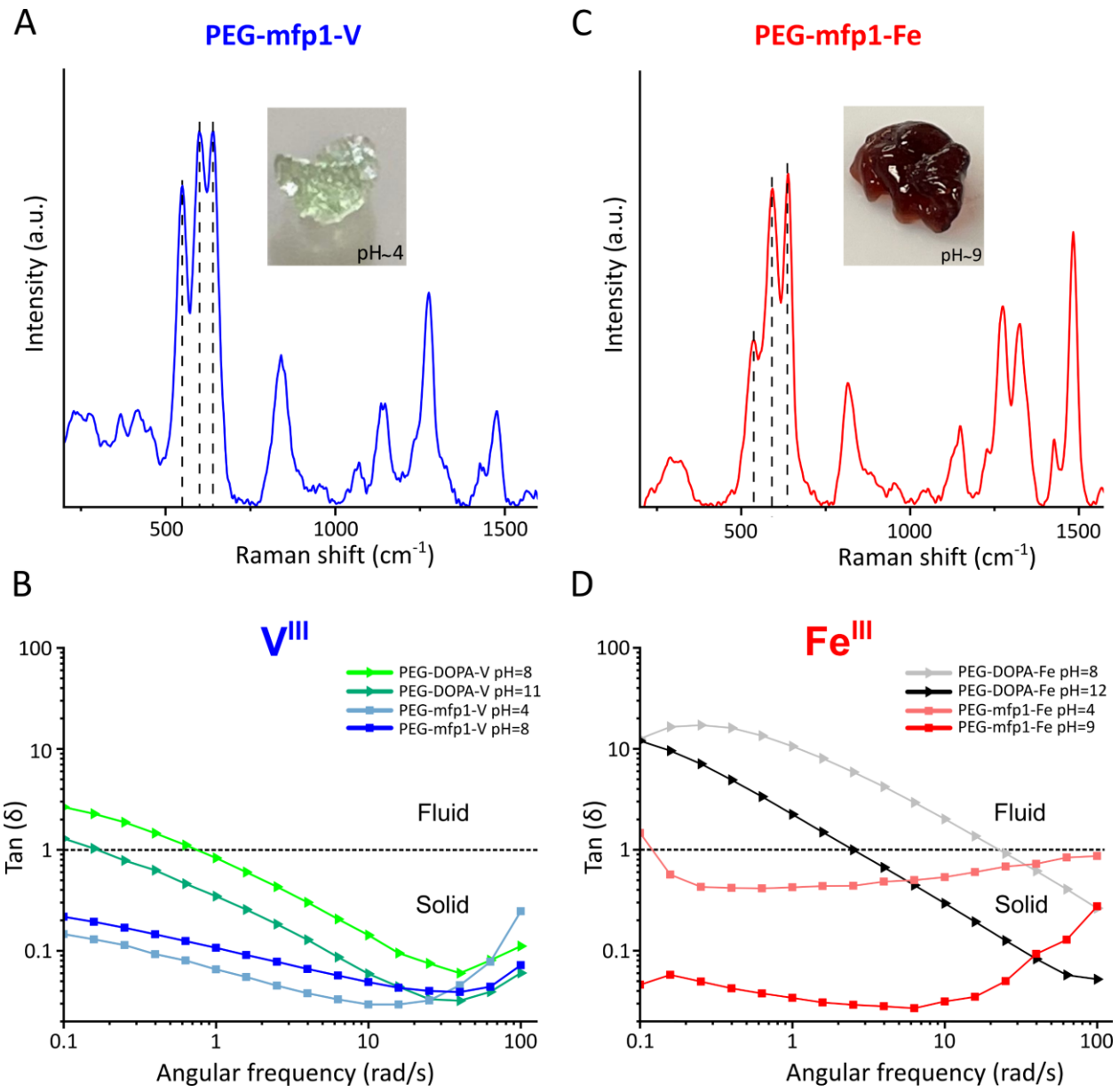

Figure 5.3: Comparative rheological analysis of PEG-mfp1 vs PEG- hydrogels. (A) and (B) Confocal Raman spectrum showing vanadium-catechol binding at pH =4, and iron-catechol binding at pH=7. (C) and (D) Tan delta plots comparing the rheological properties of PEG-DOPA vs PEG-mfp1 crosslinked with vanadium and iron respectively at selected pH values.

Upon the addition of V^{III} cations to PEG-mfp1 solution a green elastic gel was formed confirming the strong tris coordination at acidic pH values shown in the absorption spectrum (Fig. 5.3A-B). On the other hand, PEG-DOPA is not able to form stable gels with V unless the pH is raised above 7. To further elucidate the nature of this crosslinking phenomenon, we utilized confocal Raman spectroscopy, a highly effective technique employed to characterize DOPA-metal coordination bonds.[4, 17] The emergence of three distinct resonance peaks centered at approximately 600 cm^{-1} provides clear evidence for metal coordination between vanadium and catechol groups (Fig. 5.3A). [13] Furthermore, the clear presence of the charge transfer peak (CT) around 550 cm^{-1} supports the presence of a bidentate chelation as previously identified.[31] Frequency sweep tests performed on PEG-mfp1 gels formed at pH=4, shows a solid-like behavior (Tan $\delta<1$) over the whole frequency range and a storage modulus (stiffness) above 1 KPa. The absence of a crossover point highlights the slow relaxation of the network. This behavior can likely be attributed to the presence of 6 DOPA residues per chain, signifying a prolonged relaxation time compared to PEG-DOPA, which contains only one DOPA residue on each of the 4 PEG arms. When the pH is raised to 8, tan δ increases slightly, which agrees with the drop of tris-V^{IV} peak in the UV-Vis spectrum (Fig. 5.3A, B). On the other hand, PEG-DOPA will not form a gel below pH 7, PEG-DOPA gels formed via V coordination at pH 8 and 11 exhibit solid-like behavior at high frequencies and a shift towards viscous behavior at lower frequencies with relaxation times on the scale of seconds (Fig. 5.3B).

In contrast to vanadium cross-linking, mixing iron with PEG-mfp1 at pH=4 leads to a more viscous gel stabilized via bis coordination bonds, but upon raising the pH to 9, a solid elastic slow relaxing gel is formed using a combination of both bis and tris coordination as shown in Figure

5.3C. Consistent with previous reports, we observed that PEG-DOPA forms a green fluid solution with iron at acidic pH (mono coordination), which transforms into a viscous paste and viscoelastic gel as the pH is raised to 8 and 10 where bis and tris coordination dominate, respectively. Similar to vanadium crosslinked PEG-DOPA, both gels exhibit more fluid-like behavior at low frequencies (Fig. 5.3D). This characteristic can also be explained by the existence of multiple DOPA groups per chain in PEG-mfp1, indicating an extended relaxation duration in contrast to PEG-DOPA, which comprises only a single DOPA residue.

The rheological analysis conducted above highlights the increased efficacy of DOPA metal binding when retained within the naturally evolved sequence over individual DOPA molecules grafted on a polymer chain. This augmentation is evident through the creation of more robust complexes at notably lower pH values, coupled with the sustained retention of solid-like behavior over a longer timescale. These observations offer some insight into the performance disparity between mussel byssus fibers and bioinspired polymeric systems.

5.4.4 Synthesis and Characterization of Mfp1-Functionalized Hydrogels

The isolation of DOPA from its natural sequence as used in more reductionist approaches appears to miss a significant untapped potential. To demonstrate the importance of using DOPA within its context, we developed an injectable granular hydrogel system employing iron-DOPA coordinate bonds. For cytoxicity considerations, iron was the preferred choice over vanadium. Microgels were synthesized using the colloidal suspension method, producing microdroplets with sizes ranging from 10 to 50 µm.[32] This process was followed by UV curing, which effectively cross-linked these microdroplets, transforming them into stable microgels (Fig. 5.4A). As previously

reported, the stiffness of individual microgels ranges between 100-250 kPa.[33] In line with previous swelling studies, these microgels demonstrated no substantial volume change over a seven-day period in a phosphate buffer.[34] For mfp1 conjugation to the microgels , we first grafted carboxylic acid moieties onto the PEG backbone. This step was succeeded by the attachment of a maleimide moiety, achieved through EDC/NHS carbodiimide conjugation. Finally, the mfp1 peptide with cysteine at the N-terminus was grafted onto maleimide-functionalized microgels using thiol-maleimide coupling (Fig. 5.4B). The success of the functionalization was demonstrated by the presence of the Amide I vibration in both FTIR and Raman spectra (Fig. 5.4C-D)

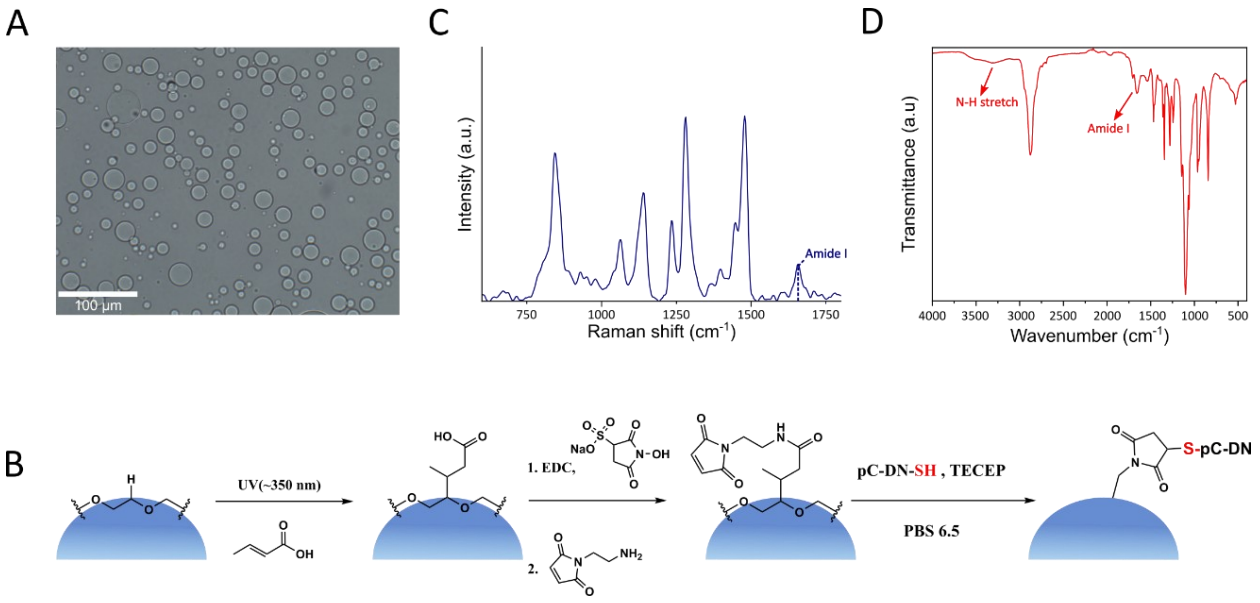

Figure 5.4: Fabrication and subsequent modification of hydrogel microparticles utilizing the mfp1 peptide. (A) Light microscope image showcasing PEG-diacrylamide microgels generated through the colloidal suspension method. (B) Functionalization steps of PEG microgels with the mfp1 peptide. Upon UV irradiation, benzophenone initiates hydrogen extraction from PEG chains, inducing surface radical generation to enable crotonic acid coupling. This is succeeded by surface carboxylic acid group activation using EDC/NHS chemistry, followed by N-(2-Aminoethyl) maleimide group coupling. The final step involves the Michael addition of the mfp1 peptide onto

the microgel surface (C) Confocal Raman spectrum indicating a uniform distribution of the peptide on the microgel surface, evidenced by Amide I peaks at ~1670 cm^{-1}. (D) FTIR spectrum of dried microgels, confirming successful peptide functionalization through observed peaks (Amide N–H stretch ~3300 cm^{-1} and Amide I ~1660 cm^{-1}).

5.4.5 Reversible Annealing at Physiological Conditions

To evaluate the potential of utilizing DOPA-metal coordination as an annealing chemistry to develop injectable granular scaffolds, we evaluated reversible crosslinking of microgels via Fe-DOPA coordination. For this, peptide-functionalized microgels were mixed with a minimal amount of $FeCl_3$ solution at pH=3. Under this acidic condition, microgels are dispersed because iron can only form relatively weak bis coordination bonds with DOPA. Upon raising the pH to 7.4, iron forms both bis and tris complexes enabling crosslinking of microgels into microporous annealed particle (MAP) scaffold (Fig. 5.5A). Color change along with Raman spectroscopic analysis revealed that annealing was caused by Fe-dopa coordination bonds (Fig. 5.5B).[17, 30] The absence of dispersed microgels post-injection revealed uniform functionalization and efficient formation of the granular hydrogel. In support of the annealing mechanism through Fe-dopa coordination rather than DOPA-based oxidative covalent cross-linking, the scaffold's dispersal into individual microgels can be controlled by adding EDTA, a potent metal-chelator with a strong affinity for iron cations.[35] Owing to the reversible nature of these metal coordination bonds, the scaffold can be reformed by reintroducing iron, demonstrating the dynamic and controllable properties of this system.

Spectroscopic analysis

Confocal Raman spectra from the dispersed and annealed scaffold phases were acquired in order to confirm the role of Fe-dopa coordination in the reversible annealing process, as illustrated in Figure 5.5B. As mentioned previously, catechol–metal bonds display distinct resonance Raman vibrational bands in the lower energy region (between 500-700 cm^{-1}). This feature allows for the differentiation between bidentate and monodentate coordination, which can be identified through a characteristic charge transfer (CT) peak at approximately 530 cm^{-1}. The CT band for the iron-annealed scaffold is consistent with a combination of bis and tris complexes, which is in agreement with the color of the scaffold and the titration studies (Fig. 5.2D).

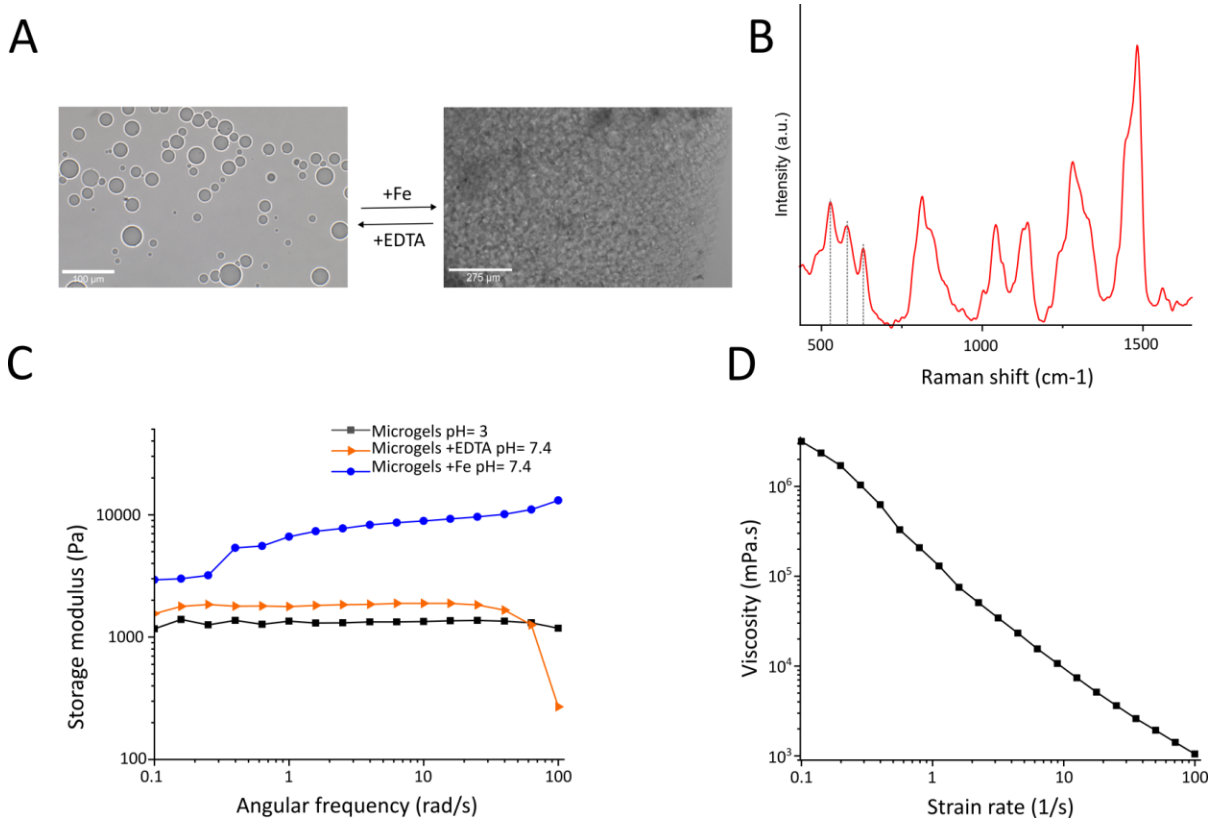

Figure 5.5: Reversible annealing based on iron-DOPA coordination. (A) Microgels functionalized with mfp1 peptide were mixed with Fe at pH= 3. Upon raising the pH to 7.4, the microgels were annealed into a porous scaffold via the formation of Iron coordination bonds (light violet color). Upon the addition of EDTA, the annealed scaffold can be broken back to individual microgels. (B) Confocal Raman spectroscopy of annealed microgels highlighting the Iron-DOPA resonance peaks. (C) Frequency sweep tests for microgels and iron at pH=3 (black), annealed granular hydrogel at pH=7.4 (blue), and scaffold treated with EDTA (orange). (D) Flow curve of annealed microgels demonstrates thixotropic characteristics under high strain rates.

5.4.6 Rheological Characterization

The mechanical properties of the crosslinked scaffold and the impact of Fe-Dopa coordination on its overall bulk mechanics were evaluated using oscillatory shear rheology (Fig. 5.5C). After adding iron ions and raising the pH of the dispersed microgels, the storage modulus G' increased by around 6 times as shown in Figure 5.4C. However, this modulus increase was reversed by adding EDTA to chelate the Fe ions (while retaining the same pH). The development of Fe-DOPA intermolecular connections between neighboring microgels is responsible for the increase in cross-link density in the bulk material, which is responsible for the increase in storage modulus.

5.4.7 Cytocompatibility of Mfp1 Annealed Scaffold

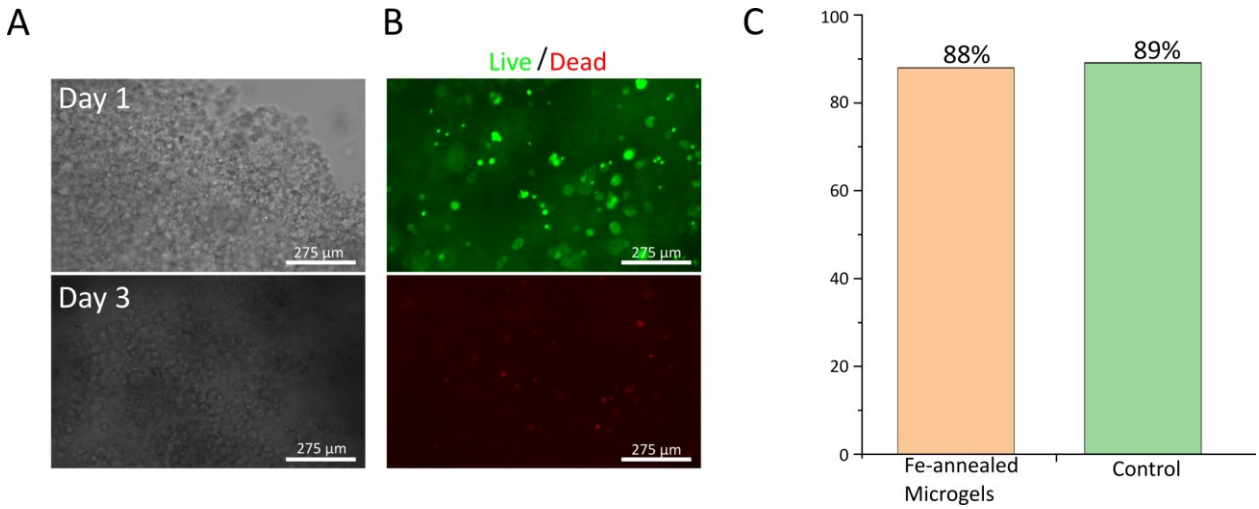

Figure 5.6: Cytocompatibility study of iron-annealed microgels. (A) Bright-field images showing microgels and cells at day 1 and day 3. (B) Evaluation of live (green) and dead (red) cells indicates that the three-dimensional cultivation of T47D cells within annealed scaffolds displays no evidence of cytotoxicity. (C) Cell viability illustrates that Fe-annealed scaffold exhibits no cytotoxic effects and serves as a favorable medium for T47D cell.

The cytocompatibility of Fe-DOPA annealed hydrogel was evaluated for potential use as injectable 3D cell scaffold was evaluated using T47D epithelial cells as a model cell culture line (Fig. 5.6). The annealed scaffolds were combined with T47D cells and subjected to centrifugation to incorporate them into the granular scaffold, followed by a three-day incubation period. Figure 5.6A shows a bright-field image of the annealed scaffold was taken at day 1, but it was challenging to distinguish between the cells and the microgels at this stage without staining. After 3 days, the live and dead cell assay depicted in Figure 5.6B exhibited minimal cell death without any signs of cytotoxicity. Cell viability, defined as the ratio of live cells to the total cell count, was measured

at 89 % for the annealed MAP scaffold, comparable to the control media's viability of 88% (Fig. 5.6C). These findings suggest that over a three-day period, the annealed scaffold demonstrated no cytotoxic effects, showcasing promising potential for future development as an injectable extracellular matrix (ECM)-like microenvironment.

5.5 Conclusion

This study reveals the significant influence of protein sequence on DOPA's metal chelation behavior. Comparative analysis between PEG-mfp1 and PEG-DOPA underscored the formation of distinct complexes at varying pH levels. These differences substantially impacted the rheological properties of gels prepared using both systems. Utilizing the improved binding between catechol and iron under physiological conditions, we developed an injectable granular system by grafting mfp1 peptides on the surface of microgels. These microgels can be crosslinked into a porous self-healing scaffold in the presence of iron at neutral pH values and can be reversibly broken by adding a chelation agent. The scaffold's proven compatibility with cells shows great potential as an injectable scaffold for tissue engineering applications.

5.6 Chemicals and Methods

5.6.1 Chemicals

All solvents and chemicals were used as received, without additional purification. PEG-diacrylamide (8KDa) was purchased from Biopharma PEG Scientific, Inc. 4 arm-PEG-maleimide (40 KDa) and 4 arm-PEG-carboxymethyl ester (40 KDa) were purchased from JeKem technology.

EDC (1-Ethyl-3-(3-dimethylaminopropyl) carbodiimide) coupling reagent was purchased from Oakwood Chemicals, while all other chemicals and reagents were obtained from Millipore-Sigma.

5.6.2 Peptide Synthesis, Purification, and Characterization

Mfp1 was manually synthesized via solid-phase peptide synthesis using Fmoc chemistry and the HCTU coupling strategy. To summarize, each amino acid (3 equiv.) was coupled using in-situ activation with HCTU and diisopropylethylamine (DIEA) in DMF. The progress of each coupling reaction was monitored using the ninhydrin test. The Fmoc-protecting group was removed using a 20% solution of piperidine in DMF. Tyrosine residues were substituted with DOPA by incorporating Fmoc-dopa (acetonide)-OH (BACHEM). Acetylation of the N-terminus was performed twice at room temperature for 30 minutes each using a mixture of acetic anhydride and DIEA (9/1 v/v). Peptides were cleaved from the Rink Amide AM resin using a mixture of TFA, ethanedithiol, phenol, and water (92.5/2.5/2.5/2.5% v/v). The crude peptides were purified using preparative HPLC with a C18 column and a linear gradient of acetonitrile in H_2O/TFA (0.06% v/v). The collected fractions were analyzed with analytical HPLC and 'time of flight' mass spectrometry using an LC/MS-TOF (Fig. 5.7). Fractions containing the desired peptide, with a purity exceeding 95%, were pooled and lyophilized.

5.6.3 Preparation of PEG-Mfp1 and PEG-DOPA

PEG-mfp1 was prepared using thiol-maleimide crosslinking chemistry. Prior to the coupling, the peptide was reacted with equimolar amounts of TCEP (tris(2-carboxyethyl)phosphine) to reduce any disulfide bridges between cysteine residues. Peptides

are then reacted with a 4-arm-PEG-maleimide in a 6.5 PBS buffer overnight. The mixture is then dialyzed against water for 24 hours using 6.5 kDa molecular weight cutoff dialysis bag from Spectrum labs, Rancho Dominguez, CA. The solution of PEG-peptide conjugate was then freeze dried and stored under nitrogen at -20 °C. Nuclear magnetic resonance spectroscopy was conducted to confirm successful functionalization (Fig. 5.8).

The synthesis of 4-Arm PEG-DOPA was conducted using a modified protocol based on the approach described by Huang et al. Under N_2, a solution was prepared by dissolving 1 g of 4-arm poly(ethylene glycol) succinimidyl carbonate (MW 40 KDa, 0.1 mmol of NHS groups) in 4 ml of anhydrous N, N-dimethylformamide (DMF). Simultaneously, 23 mg (0.15 mmol) of dopamine hydrochloride was dissolved in 4 ml of N,N-dimethylformamide (DMF) and afterwards neutralized with 16.5 µl of N-methylmorpholine. This neutralized solution was added to the PEG-SC solution after a duration of 15 minutes. The mixture was left to react overnight under an inert nitrogen atmosphere. Following that, the product was dialyzed against water buffered at ~3.5 with HCl for 36 hrs. This was done using a dialysis membrane with a molecular weight cutoff of 3.5 kDa, purchased from Spectrum in Rancho Dominguez, CA. Subsequently, the substance underwent an additional 2-hour dialysis process using MQ water. After that, the solution was freeze-dried and stored at -20 °C under nitrogen to prevent catechol oxidization. Finally, the confirmation of functionalization was carried out using ^{1}H nuclear magnetic resonance spectroscopy. The two singlet peaks around 8.7 correspond to the two hydroxyl hydrogens of the catechol group indicating successful coupling (Fig. 5.9).

5.6.4 Preparation of Peptide-Functionalized Microgels

The preparation of mfp1 functionalized microgels was achieved using a previously established protocol.[32, 34] In summary, 50 mg of PEG-diacrylamide (molecular weight=8Kda) was dissolved in 1 M saturated sodium sulfate solution and shaken vigorously. At this high salt concentration, the polymer phase separates into microdroplets (10-50 µm). Gelation of these microdroplets was initiated by adding 0.1 wt% irgacure 2959 photoinitiator and UV curing for 90 seconds using Heraeus HiLite Power UV-curing unit (Heraeus Kulzer, Germany). The excess salt was removed by subjecting the resulting microgels to repeated washing and centrifugation with milli-Q water. To render the surface of the microgels reactive, their surfaces were carboxylated by reacting them with 250 mg benzophenone and 1.5 g crotonic acid in ethanol under UV light for 15 minutes, a step repeated 5 times for optimal carboxylation.[36] Successful grafting was confirmed by the emergence of a distinct carbonyl peak around 1720 cm^{-1} in the IR spectrum (Fig. 5.10).Because the peptide contains lysine residues, employing EDC/NHS crosslinker chemistry for attachment to the microgels could result in numerous side reactions. To circumvent this issue, a cysteine residue was introduced at the N-terminus of the peptide sequence, enabling thiol-maleimide conjugation (Michael addition). Following carboxylation, the carboxylic acid moieties were activated using 45 mg of EDC (1-Ethyl-3-(3-dimethylaminopropyl) carbodiimide) and 40 mg of NHS (N-Hydroxysuccinimide) in DMF for 2 hrs. Subsequently, 10 mg of *N*-(2-Aminoethyl) maleimide trifluoroacetate salt was added to the microgels and allowed to react overnight. Successful grafting of maleimide moieties on the microgels was confirmed using infrared spectroscopy (Fig.5.10). The solvent was then exchanged to PBS at pH=7.5, and the peptide was attached to the microgels in the presence of 4 mg of TCEP (tris(2-carboxyethyl)phosphine)

reducing agent and allowed to react overnight. The final step involved washing the mfp1-functionalized microgels, followed by their characterization using infrared and Raman spectroscopy (Fig. 5.4C-D).

5.6.5 Infrared Spectroscopy

Infrared spectra of dried microgels were acquired using a Bruker α II system in attenuated total reflectance mode using a monolithic diamond ATR accessory. Spectra were recorded between a wavenumber range of 500–4000 cm^{-1}, conducting 24 scans with a resolution of 4 cm^{-1}. Following each step of the process, we used this technique to track the reaction progress. The spectral data were gathered and analyzed using OPUS software (version 7.5). Spectral averaging and background subtraction were done using Origin Pro software.

5.6.6 Confocal Raman Spectroscopy

Raman spectroscopic measurements were conducted to confirm the functionalization of the microgels and the peptide-metal coordination bonds in both the hydrogels and granular hydrogel systems. For this purpose, spectra were obtained from the hydrogels dried on glass slides, utilizing a confocal Raman microscope (α 300R, WITec). 532-nm and 785 nm lasers, with an intensity ranging from 10 to 30 mW, were employed, focusing through a 50× Zeiss objective (numerical aperture [NA] = 0.9). The detection was carried out using a thermoelectrically cooled CCD detector positioned behind a 600 g/mm grating. To acquire individual spectra, an integration time of 1 second was set 100 accumulations were averaged. All data was recorded using the WITec ControlFIVE 5.1 software and subsequently processed with WITec Plus software, which aided in cosmic ray removal and background signal subtraction.

5.6.7 Rheological Characterization

The rheological properties of the hydrogels were obtained using a stress-controlled rheometer (MCR 302, Anton Paar) fitted with a 15 mm cone plate measuring system measured at 1 mm gap. Oscillatory Frequency sweep measurements were conducted from 0.1 rad/s to 100 rad/s at a strain of 0.1 %. The temperature was maintained at 24 °C using a Peltier unit for all measurements. To prevent evaporation, a solvent trap was employed in all tests.

5.6.8 Preparation of Gels for Cell Culture

To prepare microgels for cell culture experiments, microgels were suspended in phosphate-buffered saline (PBS) (sigma). They were then centrifuged at 14000 rpm for 2 mins and the supernatant was replaced two times. Post the final rinse, the microgels were suspended in PBS containing 1% (v/v) antibiotic-antimycotic solution (ThermoFisher Scientific) and subjected to a 1 hr sterilization using UV light at 36 W. Subsequently, the supernatant was removed, and the sterilized microgels were ready for cell culture experiments. Following this, the microgels were processed in sterile conditions with biological safety cabinet (BSC).

5.6.9 T47D Cell Culture with Mfp1-Functionalized Microgels

100 µL of microgels were mixed with 150 µL of T47D-EGFP cell suspension prepared in Dulbecco's Modified Eagle Media (DMEM), enriched with 10% fetal bovine serum (FBS) and 1% antibiotic-antimycotic at the concentration of $3x10^6$ cell/ml. Cells were thoroughly mixed with the microgel via pipetting up and down. The mixture was then centrifuged at 21000 rpm for 2 minutes to precipitate the cell-microgel pellet. After discarding the supernatant, 50 µL of Fe-containing crosslinker was added and mixed with the pellet via pipetting. The mixture was

centrifuged again at 21000 rpm for 2 min and after discarding the supernatant, the gel was transferred to 96-well plate followed by addition of 200 µL of media and incubation at 37 °C and 5% CO_2 for 3 days. Brightfield images of the cells were captured on day 3 using EVOS m7000 Cell Imaging System (Thermo Fisher Scientific).

For cell viability assessment on day 3, we used Calcein AM (Life Technologies) for live cells and ethidium homodimer-1 (EthD-1) (Life Technologies) for dead cells. Calcein AM and EthD-1 in PBS were added to the wells at 2 µM, and at 4 µM concentrations, respectively and incubated at 37 °C for 10 minutes prior to imaging. As a positive control, a parallel cell culture was conducted following the same protocol but without incorporating microgels. Quantification of live and dead cells was performed using FIJI image analysis software (NIH).

5.7 Supplementary Information

Mfp1 Sequence:

Ac-Ala-Lys-Pro-Ser-**DOPA**-Pro-Pro-Thr-**DOPA**-Lys-Ala-Lys-Pro-Ser-**DOPA**-Pro-Pro-Thr-**DOPA**-Lys-Ala-Lys-Pro-Ser-**DOPA**-Pro-Pro-Thr-**DOPA**-Lys-Gly-Gly-Gly-Cys-NH_2

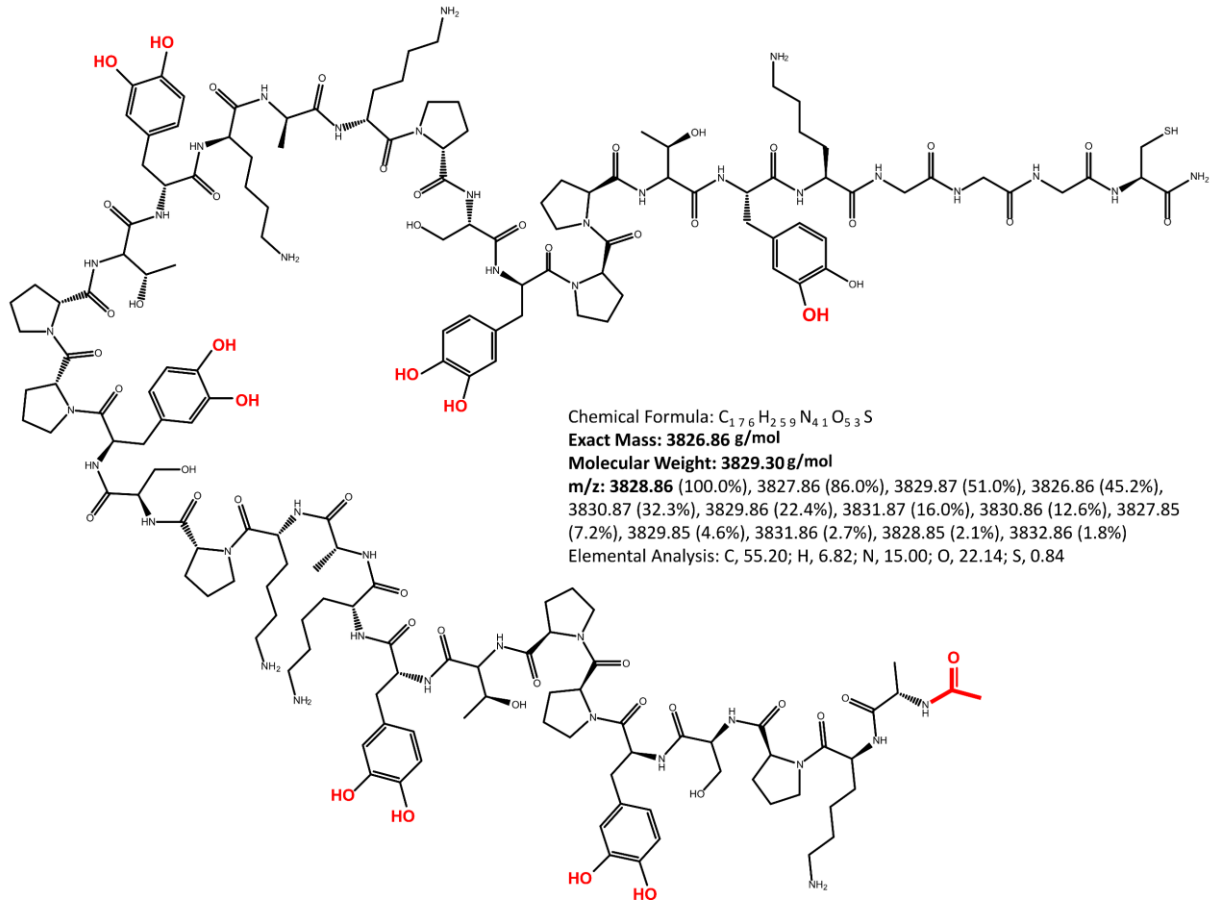

Chemical Formula: $C_{176}H_{259}N_{41}O_{53}S$
Exact Mass: 3826.86 g/mol
Molecular Weight: 3829.30 g/mol
m/z: 3828.86 (100.0%), 3827.86 (86.0%), 3829.87 (51.0%), 3826.86 (45.2%), 3830.87 (32.3%), 3829.86 (22.4%), 3831.87 (16.0%), 3830.86 (12.6%), 3827.85 (7.2%), 3829.85 (4.6%), 3831.86 (2.7%), 3828.85 (2.1%), 3832.86 (1.8%)
Elemental Analysis: C, 55.20; H, 6.82; N, 15.00; O, 22.14; S, 0.84

Figure 5.7: Mfp1 peptide sequence.

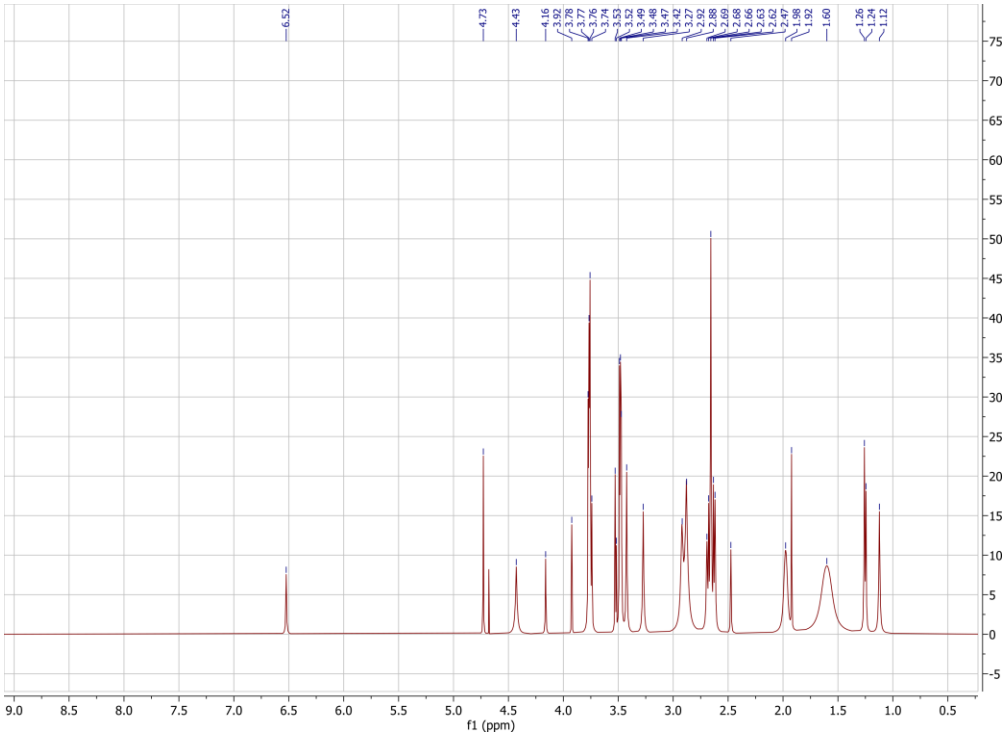

Figure 5.8: ^{1}H NMR of PEG-mfp1 conjugate.

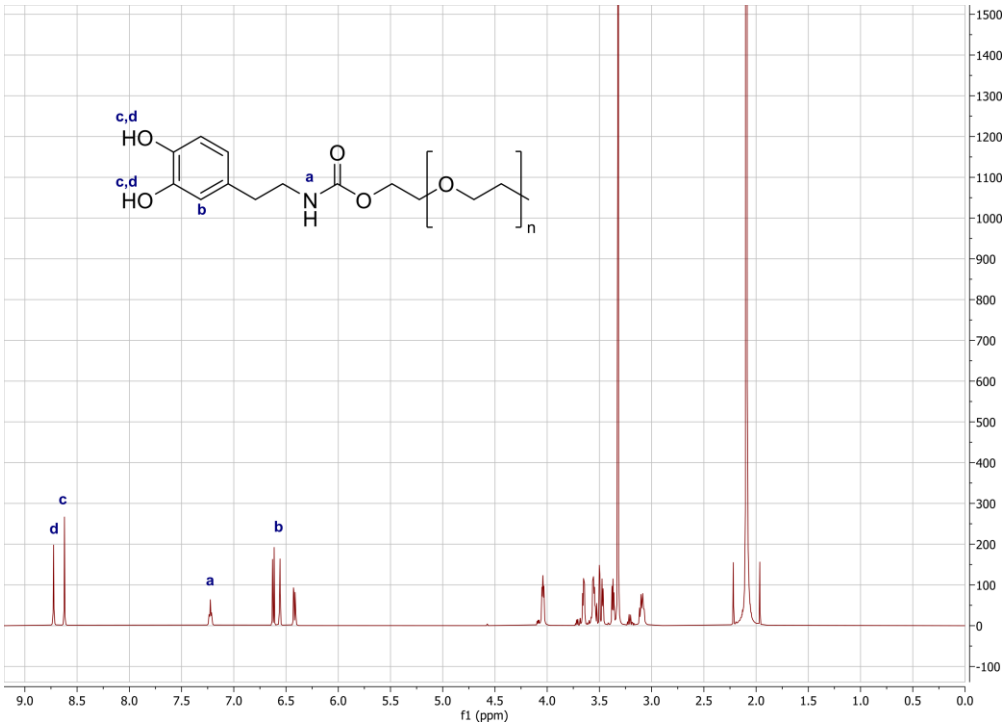

Figure 5.9: ^{1}H NMR of PEG-DOPA.

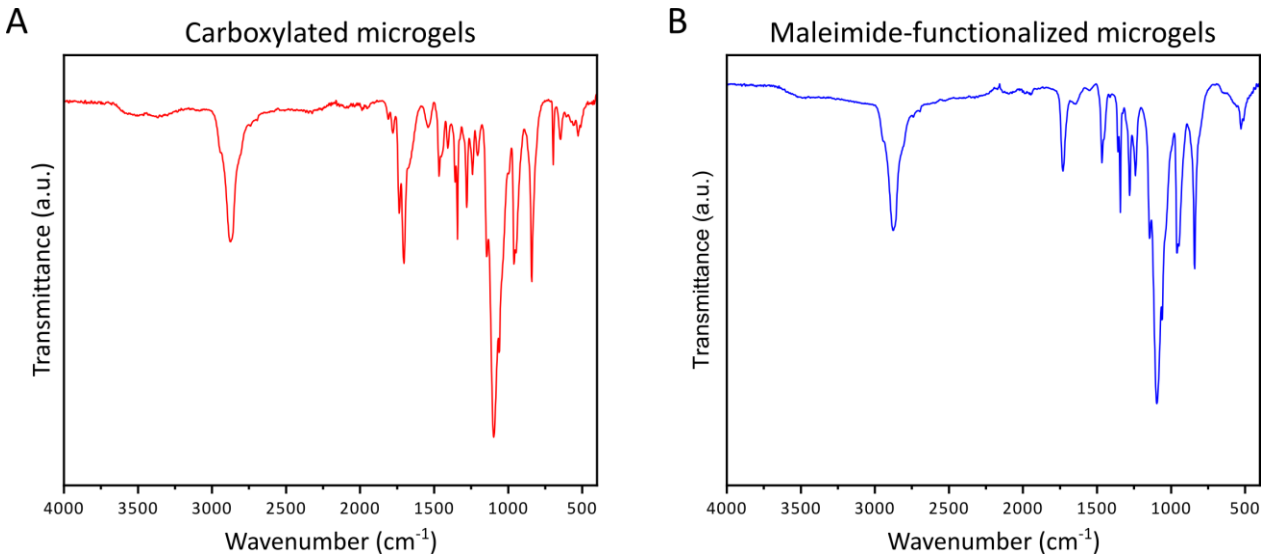

Figure 5.10: ATR-FTIR of carboxylated and maleimide-functionalized microgels.

5.8 References

1. Waite, J. H., Mussel adhesion – essential footwork. *Journal of Experimental Biology* **2017,** *220* (4), 517-530.

2. Waite, J. H., Mussel power. *Nature Materials* **2008,** *7* (1), 8-9.

3. Lee, B. P.; Messersmith, P. B.; Israelachvili, J. N.; Waite, J. H., Mussel-Inspired Adhesives and Coatings. *Annual Review of Materials Research* **2011,** *41* (1), 99-132.

4. Harrington, M. J.; Masic, A.; Holten-Andersen, N.; Waite, J. H.; Fratzl, P., Iron-Clad Fibers: A Metal-Based Biological Strategy for Hard Flexible Coatings. *Science* **2010,** *328* (5975), 216-220.

5. Holten-Andersen, N.; Mates, T. E.; Toprak, M. S.; Stucky, G. D.; Zok, F. W.; Waite, J. H., Metals and the Integrity of a Biological Coating: The Cuticle of Mussel Byssus. *Langmuir* **2009,** *25* (6), 3323-3326.

6. Vaccaro, E.; Waite, J. H., Yield and Post-Yield Behavior of Mussel Byssal Thread: A Self-Healing Biomolecular Material. *Biomacromolecules* **2001,** *2* (3), 906-911.

7. Hwang, D. S.; Zeng, H.; Masic, A.; Harrington, M. J.; Israelachvili, J. N.; Waite, J. H., Protein- and Metal-dependent Interactions of a Prominent Protein in Mussel Adhesive Plaques*. *Journal of Biological Chemistry* **2010,** *285* (33), 25850-25858.

8. Xu, Q.; Xu, M.; Lin, C.-Y.; Zhao, Q.; Zhang, R.; Dong, X.; Zhang, Y.; Tian, S.; Tian, Y.; Xia, Z., Metal Coordination-Mediated Functional Grading and Self-Healing in Mussel Byssus Cuticle. *Advanced Science* **2019,** *6* (23), 1902043.

9. Lee, B. P.; Dalsin, J. L.; Messersmith, P. B., Synthesis and Gelation of DOPA-Modified Poly(ethylene glycol) Hydrogels. *Biomacromolecules* **2002,** *3* (5), 1038-1047.

10. Wu, M.; Peng, Q.-Y.; Han, L.-B.; Zeng, H.-B., Self-healing Hydrogels and Underlying Reversible Intermolecular Interactions. *Chinese Journal of Polymer Science* **2021,** *39* (10), 1246-1261.

11. Ji, Y.-R.; Young, T.-H.; Tsai, T.-Y.; Chen, J.-S.; Chen, K.-C., Dopamine-Modified Alginate Hydrogel with Effectiveness and Safety for Preoperative Localization of Lung Nodules. *ACS Biomaterials Science & Engineering* **2021,** *7* (9), 4637-4644.

12. Dalsin, J. L.; Hu, B.-H.; Lee, B. P.; Messersmith, P. B., Mussel Adhesive Protein Mimetic Polymers for the Preparation of Nonfouling Surfaces. *Journal of the American Chemical Society* **2003,** *125* (14), 4253-4258.

13. Holten-Andersen, N.; Harrington, M. J.; Birkedal, H.; Lee, B. P.; Messersmith, P. B.; Lee, K. Y. C.; Waite, J. H., pH-induced metal-ligand cross-links inspired by mussel yield self-healing polymer networks with near-covalent elastic moduli. *Proceedings of the National Academy of Sciences* **2011,** *108* (7), 2651-2655.

14. Moulay, S., Dopa/Catechol-Tethered Polymers: Bioadhesives and Biomimetic Adhesive Materials. *Polymer Reviews* **2014,** *54* (3), 436-513.

15. Chan Choi, Y.; Choi, J. S.; Jung, Y. J.; Cho, Y. W., Human gelatin tissue-adhesive hydrogels prepared by enzyme-mediated biosynthesis of DOPA and Fe3+ ion crosslinking. *Journal of Materials Chemistry B* **2014,** *2* (2), 201-209.

16. Filippidi, E.; Cristiani, T. R.; Eisenbach, C. D.; Waite, J. H.; Israelachvili, J. N.; Ahn, B. K.; Valentine, M. T., Toughening elastomers using mussel-inspired iron-catechol complexes. *Science* **2017,** *358* (6362), 502-505.

17. Holten-Andersen, N.; Jaishankar, A.; Harrington, M. J.; Fullenkamp, D. E.; DiMarco, G.; He, L.; McKinley, G. H.; Messersmith, P. B.; Lee, K. Y. C., Metal-coordination: using one of nature's tricks to control soft material mechanics. *Journal of Materials Chemistry B* **2014,** *2* (17), 2467-2472.

18. Priemel, T.; Palia, G.; Förste, F.; Jehle, F.; Sviben, S.; Mantouvalou, I.; Zaslansky, P.; Bertinetti, L.; Harrington, M. J., Microfluidic-like fabrication of metal ion–cured bioadhesives by mussels. *Science* **2021,** *374* (6564), 206-211.

19. Jehle, F.; Macías-Sánchez, E.; Sviben, S.; Fratzl, P.; Bertinetti, L.; Harrington, M. J., Hierarchically-structured metalloprotein composite coatings biofabricated from co-existing condensed liquid phases. *Nature Communications* **2020,** *11* (1), 862.

20. Mesko, M.; Xiang, L.; Bohle, S.; Hwang, D. S.; Zeng, H.; Harrington, M. J., Catechol-Vanadium Binding Enhances Cross-Linking and Mechanics of a Mussel Byssus Coating Protein. *Chemistry of Materials* **2021,** *33* (16), 6530-6540.

21. Deacon, M. P.; Davis, S. S.; Waite, J. H.; Harding, S. E., Structure and Mucoadhesion of Mussel Glue Protein in Dilute Solution. *Biochemistry* **1998,** *37* (40), 14108-14112.

22. Waite, J. H.; Housley, T. J.; Tanzer, M. L., Peptide repeats in a mussel glue protein: theme and variations. *Biochemistry* **1985,** *24* (19), 5010-5014.

23. Mealy, J. E.; Chung, J. J.; Jeong, H.-H.; Issadore, D.; Lee, D.; Atluri, P.; Burdick, J. A., Injectable Granular Hydrogels with Multifunctional Properties for Biomedical Applications. *Advanced Materials* **2018,** *30* (20), 1705912.

24. Lee, H.; Dellatore, S. M.; Miller, W. M.; Messersmith, P. B., Mussel-Inspired Surface Chemistry for Multifunctional Coatings. *Science* **2007,** *318* (5849), 426-430.

25. Brubaker, C. E.; Kissler, H.; Wang, L.-J.; Kaufman, D. B.; Messersmith, P. B., Biological performance of mussel-inspired adhesive in extrahepatic islet transplantation. *Biomaterials* **2010,** *31* (3), 420-427.

26. Sever, M. J.; Wilker, J. J., Absorption spectroscopy and binding constants for first-row transition metal complexes of a DOPA-containing peptide. *Dalton Transactions* **2006,** (6), 813-822.

27. Liu, Y.; Meng, H.; Konst, S.; Sarmiento, R.; Rajachar, R.; Lee, B. P., Injectable Dopamine-Modified Poly(ethylene glycol) Nanocomposite Hydrogel with Enhanced Adhesive Property and Bioactivity. *ACS Applied Materials & Interfaces* **2014,** *6* (19), 16982-16992.

28. Bilic, G.; Brubaker, C.; Messersmith, P. B.; Mallik, A. S.; Quinn, T. M.; Haller, C.; Done, E.; Gucciardo, L.; Zeisberger, S. M.; Zimmermann, R.; Deprest, J.; Zisch, A. H., Injectable candidate sealants for fetal membrane repair: bonding and toxicity in vitro. *American Journal of Obstetrics and Gynecology* **2010,** *202* (1), 85.e1-85.e9.

29. Martinez Rodriguez, N. R.; Das, S.; Kaufman, Y.; Israelachvili, J. N.; Waite, J. H., Interfacial pH during mussel adhesive plaque formation. *Biofouling* **2015,** *31* (2), 221-227.

30. Priemel, T.; Palia, R.; Babych, M.; Thibodeaux, C. J.; Bourgault, S.; Harrington, M. J., Compartmentalized processing of catechols during mussel byssus fabrication determines the destiny of DOPA. *Proceedings of the National Academy of Sciences* **2020,** *117* (14), 7613-7621.

31. Michaud-Soret, I.; Andersson, K. K.; Que, L., Jr.; Haavik, J., Resonance Raman Studies of Catecholate and Phenolate Complexes of Recombinant Human Tyrosine Hydroxylase. *Biochemistry* **1995,** *34* (16), 5504-5510.

32. Pussak, D.; Behra, M.; Schmidt, S.; Hartmann, L., Synthesis and functionalization of poly(ethylene glycol) microparticles as soft colloidal probes for adhesion energy measurements. *Soft Matter* **2012,** *8* (5), 1664-1672.

33. Schmidt, S.; Reinecke, A.; Wojcik, F.; Pussak, D.; Hartmann, L.; Harrington, M. J., Metal-Mediated Molecular Self-Healing in Histidine-Rich Mussel Peptides. *Biomacromolecules* **2014,** *15* (5), 1644-1652.

34. Rammal, M.; Li, C.; Reeves, J.; Moraes, C.; Harrington, M. J., pH-Responsive Reversible Granular Hydrogels Based on Metal-Binding Mussel-Inspired Peptides. *ACS Applied Materials & Interfaces* **2023,** *15* (24), 29004-29011.

35. Sunda, W.; Huntsman, S., Effect of pH, light, and temperature on Fe–EDTA chelation and Fe hydrolysis in seawater. *Marine Chemistry* **2003,** *84* (1), 35-47.

36. Schmidt, S.; Wang, H.; Pussak, D.; Mosca, S.; Hartmann, L., Probing multivalency in ligand–receptor-mediated adhesion of soft, biomimetic interfaces. *Beilstein Journal of Organic Chemistry* **2015,** *11*, 720-729.

Chapter 6 : Discussion

Through billions of years of evolution, nature has arrived at efficient, economical, and sustainable means of materials fabrication. Various environmental pressures have led to evolution through natural selection of effective material solutions using a minimum of resources and energy. This has occurred across a wide diversity of species which have developed materials that are effectively tailored to their needs. Moreover, many of these materials possess properties like self-healing[1], wet adhesion[2], actuation[3], and structural color[4], that are unmatched by human-made materials. As a result, biological materials, ranging from lightweight yet stiff bird bones to the tough flexible spider silk fibers, have the potential to provide inspiration for development and sustainable manufacture of advanced materials. However, this requires a deep understanding of the structure-function relationships defining these materials and the materials fabrication mechanisms by which they are produced. Indeed, nature exhibits unparalleled efficiency in managing natural resources. Unlike human-made materials that usually require extreme conditions, rare or toxic resources, and high energy expenditure, biological materials are fabricated at ambient temperatures and pressures with minimal energy expenditure. For example, using only sunlight, water and carbon dioxide, trees can make wood – an incredibly tough and versatile material. This natural alchemy, free from the need for extreme synthesis conditions, provides a blueprint for a more environmentally responsible future in material science.

Attempts to mimic the complexities and intricacies of biological materials are an imposing task, especially considering that living organisms operate within a limited range of bio-friendly

conditions and utilize very basic material precursors (biomolecules and some inorganic components common in the environment). Yet, despite having access to only a fraction of the resources and energy that modern technology offers, nature through a profound mastery of chemistry and hierarchical assembly is able to fabricate materials that often surpass their human-made counterparts in functionality and efficiency. However, the complexity of these materials and their formation has not prevented numerous scientists to study these biological materials and to adapt certain aspects of the natural design principles to fabricate high-performance materials that can offer solutions to modern-day challenges. Scientists have utilized a diverse array of characterization techniques to study the composition and structure-function relationships within biological materials, aiming to translate these findings into the development of synthetic materials. However, rather than attempting to replicate every detail of the biological structure, there has been a focus on specific chemical tricks that nature uses that are easy to mimic at the lab bench. For instance, there has been growing evidence that suggests that different types of organisms including spiders, insects and mussels leverage metal coordination beyond mere cellular functions, instead using metal coordination as a means of cross-linking to create robust and responsive materials.[5] As a concrete example, numerous studies have shown that marine mussels utilize different types of transition-metal coordinate bonds to fabricate stiff yet tough and extensible fibers with self-healing capacity that allow them to attach firmly to rocks within challenging marine intertidal zones.[6, 7] Several investigations have highlighted the role of metal ions such as zinc in imparting toughness and self-healing by sacrificially rupturing under high stress, thereby preventing irreversible breakage of the covalent bonds, and then subsequently reforming to repair the damage done.[8, 9] In addition to acting as sacrificial bonds,

metals can play an important role in guiding the self-assembly through binding histidine groups in a pH-dependent manner.[10] On the other hand, DOPA-metal has been shown play a big role in the hardness/stiffness and remarkable flexibility of the mussel byssal thread cuticle.[11] These crosslinks exhibit a high bond strength comparable to a covalent bond and an extremely high stability constant for a metal crosslink (log K= 37–40, K is the equilibrium constant for the complex formation).[12] Despite this robustness, they maintain the reversible nature of metal crosslinks, making them good candidates for the developments of self-healing hydrogels and adhesives. This thesis has focused on investigating and leveraging these interactions to develop dynamic self-healing polymeric materials for applications that range from injectable scaffold for tissue repair applications to self-healing thermochromic elastomeric materials. In this discussion, I highlight some of the challenges we faced in each project and discuss future directions that can be taken to optimize the fabrication process or the material performance.

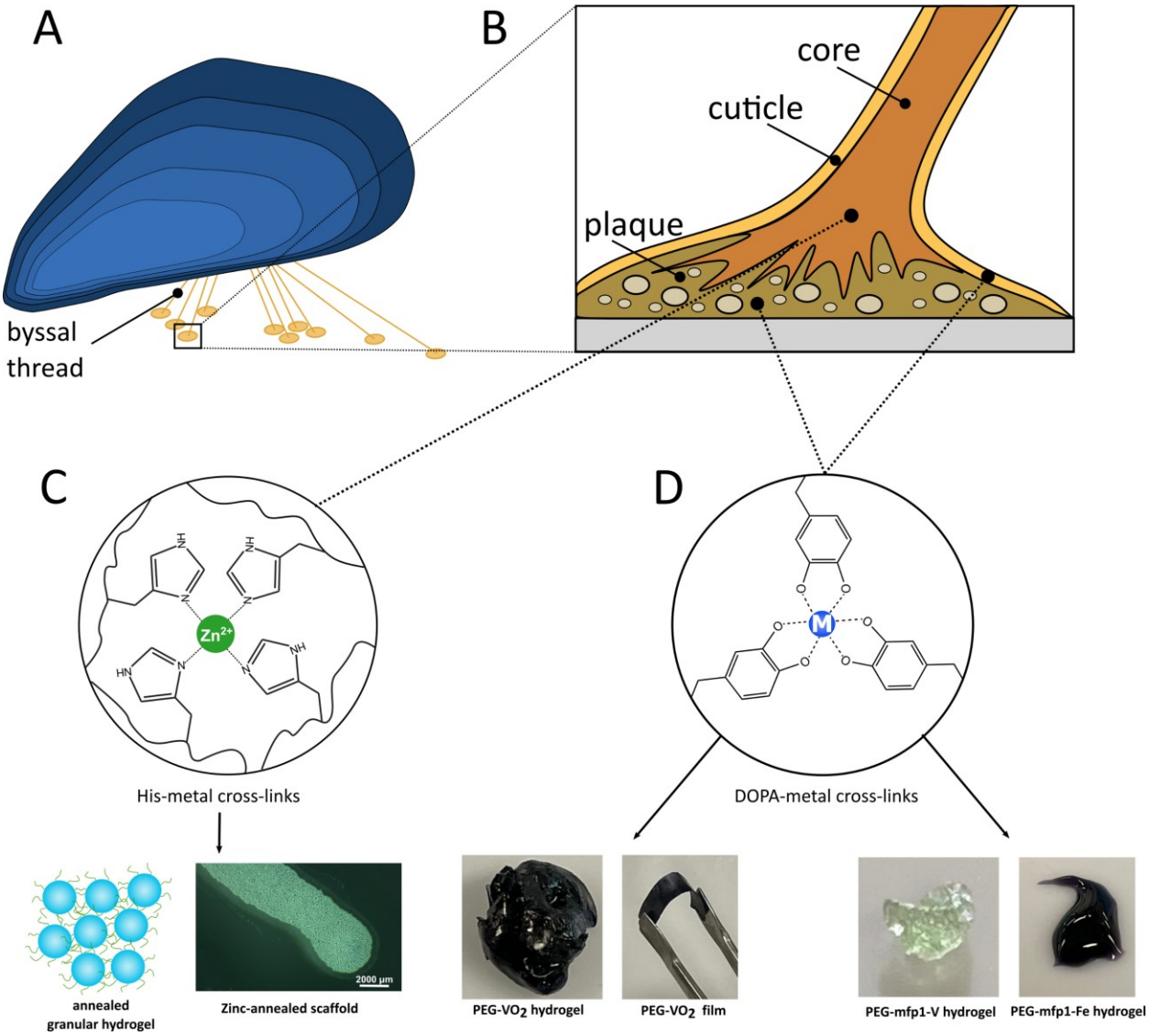

Figure 6.1: Mussel inspired metal-crosslinked materials. (A) Mussel byssus anchoring to a surface using the byssus. (B) Schematic representation of the byssus parts composed of an inner tough core, hard cuticle, and foamy plaque. (C) Zinc-annealed microporous scaffold inspired by zinc-histidine coordination in the byssus core. (D) Thermochromic self-healing hydrogels/films and peptide hydrogels inspired by the DOPA-metal coordination in the cuticle and plaque of the byssus.

Injectable scaffold based on mussel-inspired metal coordination

Supramolecular hydrogels, utilizing noncovalent or dynamic covalent interactions stand out as a promising class of self-healing biomaterials due to their dynamic and diffusive nature, distinguishing them from traditional polymers, ceramics, or cements.[13] Over time, hydrogels have gained recognition as a promising platform for biomaterials in various biomedical applications.[14] Their versatility allows for engineering their mechanical properties to mimic the viscoelastic behavior of the extracellular matrix (ECM) in different tissues. In the past few years, much attention has been directed toward injectable self-healing hydrogel systems due to their potential in minimally invasive administration through a narrow syringe. Injectable granular hydrogels , made from spherical microgels, have attracted a lot of attention in the field of regenerative medicine, such as wound healing and cardiac repair owing to their porosity and thixotropic properties.[15] The figure below (Fig. 6.2) shows the workflow used in many research groups to develop granular hydrogel systems for the desired application in mind. The main challenge for these injectable materials is dynamic tissue environments.[16] For example, attempting to provide mechanical support or deliver therapeutics to the myocardium using granular hydrogels is challenging due to the dynamic nature of the heart tissue. To overcome this, scientists developed microgels that can be crosslinked together after injection. However, these systems either depended on covalent interactions which yielded stiff by brittle scaffolds, or host guest interactions which yielded weakly crosslinked scaffold.[17]

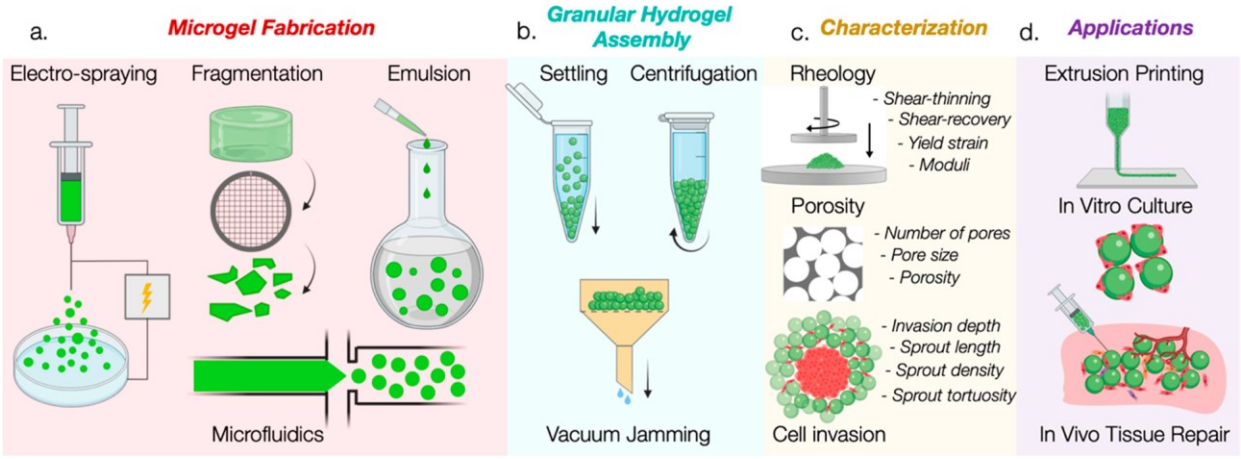

Figure 6.2: Granular hydrogels workflow for biomedical applications. (a) different fabrication methods of hydrogel microparticles. (b) Granular hydrogel assembly triggered by jamming. (c) Structural and rheological characterization to suit the application in mind. (d) application of granular hydrogels in bioprinting, in vitro cell culture, and in vivo tissue repair applications. Adapted with permission from ref.[18]

To address these challenges, we harnessed the robust metal-based annealing chemistries utilized by marine mussels to self-assemble long sequences of proteins into tough and self-healing fibers. In our first study, instead of taking histidine out of its natural sequence to crosslink the microgels together, we used a short peptide sequence derived from the N-terminal histidine-rich domain of the preCol-NG. This choice was based on two main reasons. Firstly, this sequence has evolved for millions of years to bind zinc efficiently in order to produce tough byssal threads. Attempts to make hydrogels using histidine-terminated polymers with metal ions has resulted in weakly crosslinked networks.[19] Secondly, incorporating a peptide sequence onto the microgels facilitates interactions between particles, enhancing their ability to interact with one another. We were successful in making a self-healing injectable hydrogel taking advantage of this strong

yet reversible zinc-histidine coordination. However, we still have some obstacles to translate this system into tissue engineering applications. Firstly, although peptides grant stronger interactions, producing them in large quantities using solid-state synthesis is costly and challenging. This issue is common among biopolymers used for materials production. For instance, while DNA-based hydrogels have shown tremendous potential in various applications, their poor scalability and high cost limits their wider utilization in clinical applications. However, the advancement in high-throughput production methods can take peptide production from small-scale to kilogram quantities.[20] Secondly, zinc-histidine coordination, like most supramolecular interactions, is sensitive to local pH changes which make it challenging to maintain the structural integrity of the network for a prolonged period of time. Finally, it took several steps to produce peptide-functionalized microgels. For future studies, it would be very helpful to make a polymer-peptide conjugate that can be crosslinked into microgels using different crosslinking chemistries. This would accelerate the production process and reduce the loss of microgels at each step. To optimize our scaffold, we attempted to eliminate the need for a metal crosslinker. The section below provides a brief overview of the project, emphasizing both the challenges encountered and potential future directions.

To create an injectable system that self-assembles into a scaffold under physiological conditions without the need metal-based crosslinker, I attempted annealing based on pH-triggered beta sheet formation.[21] The ability to form structures without the need for a crosslinker simplifies the injection process, enhancing its suitability for medical use. To achieve this, I developed a technique to functionalize PEG microgels with a histidine-rich sequence derived from the N-terminal domain of preCol-D protein (AVAHAHAHAHASAGANGRARAHARAGGGC), a

sequence known for its conservation across various mussel species. This project was inspired by Trapaidze et al. who demonstrated that functionalizing a 4-arm polyethylene glycol polymer with this peptide enables gel formation simply by adjusting the pH to physiological levels.[21] Remarkably, this gelation process is reversible; lowering the pH causes the gel to dissolve. This is triggered by the formation of a beta-crystalline secondary structure by the peptide which enables it to crosslink the polymer, resulting in the creation of a hydrogel network. Briefly, microgels were first carboxylated using the same method discussed in Chapters 3 and 5, followed by coupling a thiol-reactive maleimide group using EDC/NHS coupling. Finally, the pH-responsive sequence was attached to the microgels. Although I was successful in grafting the peptide on the surface of the microgels, our efforts to crosslink the microgels upon raising the pH were not fruitful. This challenge may arise from the peptide's binding to the microgels potentially obstructing the formation of beta sheets with neighboring particles. Alternatively, it could be due to the binding strength not being large enough to hold the microgels together. For future research, longer peptide sequences able to form more robust beta-sheet interactions could potentially overcome this challenge. Alternatively, microgels could be possibly functionalized with complementary DNA strands which allow binding with high specificity. Moreover, the strength of the binding could be easily tuned by changing the length of the DNA chains.

Mussel-inspired flexible thermochromic films

Advancements in polymer science, semiconductor technologies, and manufacturing have resulted in the development of resilient and adaptable displays, sensors, and wearable devices.[22] These products once considered implausible just a few years ago are now expected to dominate

the market in the near future. Due to its metal-insulator transition, VO_2 has attracted significant attention and found applications in a great number of applications such as thermochromic windows, sensors, and field-effect transistors. [23-25] Despite these benefits, the multivalent state of vanadium and the intricate thermodynamics of vanadium oxides make it difficult to fabricate VO2 with the desired phase transition features.[26] Expensive equipment and harsh conditions, such as high temperatures and precisely regulated atmospheres, are always necessary. However, most polymers can't endure such elevated temperatures , making the fabrication of crystalline VO_2 films on flexible polymer substrates unfeasible.[27] Solution-based methods where the nanoparticles are embedded in a polymer matrix is a key strategy to prepare flexible thermochromic coating with improved uniformity and stability of VO_2 nanoparticles. However, weak polymer nanoparticles interactions often lead to aggregation which impacts the performance of the material. Drawing inspiration from the chemical strategies employed by marine mussels involving catechol-vanadium interactions, our goal was to employ a polymeric system capable of robustly binding VO_2 nanoparticles. This binding not only prevents aggregation but also produces a film possessing both elastomeric properties. Hydrogels prepared using this method exhibited solid-like mechanics while maintaining their self-healing and thermochromic properties. In the pursuit of making films that exhibit a reversible insulator-to-metal (IMT) at room temperature values, we used tungsten-doped VO_2 nanoparticles to crosslink PEG-$dopa_4$ into a thermochromic films.[28] For this we bought commercially available W-VO_2 nanoparticles with a transition temperature of ~ 26 °C; however, sintering the nanoparticles lead to a size increase up to 5 µm. Despite successfully fabricating hydrogels and films using these particles, they exhibited weak mechanics and poor distribution of the particles in the network. To address

this challenge, a future objective could be to devise a methodology for producing W-VO_2 nanoparticles while ensuring their size remains small and controlled. Lowering the phase transition temperature is crucial for thermochromic smart windows. Moreover, we think that the binding of VO_2 nanoparticles to the polymer can protect them from oxidation which prolongs the lifetime of the film. To test this hypothesis, X-ray photoelectron spectroscopy (XPS) can be a powerful tool that enables us to monitor the surface oxidation of the nanoparticles, both in the presence and absence of bound catechol groups.

DOPA-Metal coordination: A Comparative Analysis in Natural and Synthetic Environment

Although mussel inspired materials have shown tremendous potential as wet adhesives and self- healing soft materials, they still lag far behind the natural byssus fibers. While closing this gap might seem like an ambitious objective given the intricate complexity and hierarchical nature of the natural system, it remains pivotal to revisit the natural system to gain more insight about the chemistries employed by the mussels. The third project was inspired by the work of Mesko and coworkers that showed that rmfp1 protein exhibits a strikingly different metal chelation behavior than catechol groups, highlighting the role of the protein sequence.[29] This study highlighted that cross-linking facilitated by DOPA-V significantly enhances the cohesion of the protein network, nearly doubling its strength compared to DOPA-Fe.[29] In the third study, I attempted to replicate the same behavior with a shorter peptide sequence, and try to harness it to prepare hydrogels at conditions not attainable with the traditional DOPA-functionalized polymers, using three repeats of (AKPSYPPTYK) derived from the mfp1 protein sequence.[30] Initially, the approach involved enzymatically converting the tyrosine residue into catechol

groups using mushroom tyrosinase. Unfortunately, we encountered challenges in controlling the kinetics of the reaction, as the formed catechol groups underwent immediate oxidation. As an alternative, we were successful in manually synthesizing the peptide sequence, substituting tyrosine residues with DOPA. As discussed in Chapter 5, mfp1 could bind vanadium in a tris coordination at extremely low pH values and form multiple bis coordination interactions with iron at acidic conditions replicating the behavior of rmfp1. This further supports the mussel's apparent preference to bind vanadium over iron in the byssus as shown by recent STEM-EDS compositional analysis on the cuticle.[6, 31] In an attempt to understand the mechanism behind this behavior of DOPA with the natural sequence, we replaced the lysine residues that neighbors DOPA by norleucine eliminating the terminal amine group on the side chain. Given the highlighted synergy between Lysine and DOPA in promoting adhesion in various studies, we aimed to explore whether Lysine might also influence DOPA's behavior in metal chelation.[32, 33] However, titration studies did not show any clear differences between norleucine-substituted peptide mfp1 control with both iron and vanadium. This hints to other factors such as the peptide's flexibility, cooperativity, or role of specific amino acids in the sequence.

6.1 References

1. Koga, T.; Morishita, T.; Harumoto, Y.; Nishimura, S.-n.; Higashi, N., Spider silk-inspired peptide multiblock hybrid copolymers for self-healable thin film materials. *Materials Advances* **2021,** *2* (24), 7851-7860.

2. Ahn, B. K., Perspectives on Mussel-Inspired Wet Adhesion. *Journal of the American Chemical Society* **2017,** *139* (30), 10166-10171.

3. Kim, I. H.; Choi, S.; Lee, J.; Jung, J.; Yeo, J.; Kim, J. T.; Ryu, S.; Ahn, S.-k.; Kang, J.; Poulin, P.; Kim, S. O., Human-muscle-inspired single fibre actuator with reversible percolation. *Nature Nanotechnology* **2022,** *17* (11), 1198-1205.

4. Chen, F.; Huang, Y.; Li, R.; Zhang, S.; Wang, B.; Zhang, W.; Wu, X.; Jiang, Q.; Wang, F.; Zhang, R., Bio-inspired structural colors and their applications. *Chemical Communications* **2021,** *57* (99), 13448-13464.

5. Khare, E.; Holten-Andersen, N.; Buehler, M. J., Transition-metal coordinate bonds for bioinspired macromolecules with tunable mechanical properties. *Nature Reviews Materials* **2021,** *6* (5), 421-436.

6. Priemel, T.; Palia, G.; Förste, F.; Jehle, F.; Sviben, S.; Mantouvalou, I.; Zaslansky, P.; Bertinetti, L.; Harrington, M. J., Microfluidic-like fabrication of metal ion–cured bioadhesives by mussels. *Science* **2021,** *374* (6564), 206-211.

7. Harrington, M. J.; Masic, A.; Holten-Andersen, N.; Waite, J. H.; Fratzl, P., Iron-Clad Fibers: A Metal-Based Biological Strategy for Hard Flexible Coatings. *Science* **2010,** *328*, 216.

8. Reinecke, A.; Bertinetti, L.; Fratzl, P.; Harrington, M. J., Cooperative behavior of a sacrificial bond network and elastic framework in providing self-healing capacity in mussel byssal threads. *Journal of Structural Biology* **2016,** *196* (3), 329-339.

9. Schmitt, C. N. Z.; Politi, Y.; Reinecke, A.; Harrington, M. J., Role of Sacrificial Protein–Metal Bond Exchange in Mussel Byssal Thread Self-Healing. *Biomacromolecules* **2015,** *16* (9), 2852-2861.

10. Reinecke, A.; Brezesinski, G.; Harrington, M. J., pH-Responsive Self-Organization of Metal-Binding Protein Motifs from Biomolecular Junctions in Mussel Byssus. *Advanced Materials Interfaces* **2017,** *4* (1), 1600416.

11. Harrington, M. J.; Masic, A.; Holten-Andersen, N.; Waite, J. H.; Fratzl, P., Iron-Clad Fibers: A Metal-Based Biological Strategy for Hard Flexible Coatings. *Science* **2010,** *328* (5975), 216-220.

12. Holten-Andersen, N.; Harrington, M. J.; Birkedal, H.; Lee, B. P.; Messersmith, P. B.; Lee, K. Y. C.; Waite, J. H., pH-induced metal-ligand cross-links inspired by mussel yield self-healing polymer networks with near-covalent elastic moduli. *Proceedings of the National Academy of Sciences* **2011,** *108* (7), 2651-2655.

13. Omar, J.; Ponsford, D.; Dreiss, C. A.; Lee, T.-C.; Loh, X. J., Supramolecular Hydrogels: Design Strategies and Contemporary Biomedical Applications. *Chemistry – An Asian Journal* **2022,** *17* (9), e202200081.

14. Chai, Q.; Jiao, Y.; Yu, X., Hydrogels for Biomedical Applications: Their Characteristics and the Mechanisms behind Them. *Gels* **2017,** *3* (1), 6.

15. Daly, A. C.; Riley, L.; Segura, T.; Burdick, J. A., Hydrogel microparticles for biomedical applications. *Nature Reviews Materials* **2020,** *5* (1), 20-43.

16. Mealy, J. E.; Chung, J. J.; Jeong, H.-H.; Issadore, D.; Lee, D.; Atluri, P.; Burdick, J. A., Injectable Granular Hydrogels with Multifunctional Properties for Biomedical Applications. *Advanced Materials* **2018,** *30* (20), 1705912.

17. Daly, A. C.; Riley, L.; Segura, T.; Burdick, J. A., Hydrogel Microparticles for Biomedical Applications. *Nat. Rev. Mater.* **2020,** *5*, 20.

18. Qazi, T. H.; Muir, V. G.; Burdick, J. A., Methods to Characterize Granular Hydrogel Rheological Properties, Porosity, and Cell Invasion. *ACS Biomaterials Science & Engineering* **2022,** *8* (4), 1427-1442.

19. Fullenkamp, D. E.; He, L.; Barrett, D. G.; Burghardt, W. R.; Messersmith, P. B., Mussel-Inspired Histidine-Based Transient Network Metal Coordination Hydrogels. *Macromolecules* **2013,** *46* (3), 1167-1174.

20. Andersson, L.; Blomberg, L.; Flegel, M.; Lepsa, L.; Nilsson, B.; Verlander, M., Large-scale synthesis of peptides. *Peptide Science* **2000,** *55* (3), 227-250.

21. Trapaidze, A.; D'Antuono, M.; Fratzl, P.; Harrington, M. J., Exploring mussel byssus fabrication with peptide-polymer hybrids: Role of pH and metal coordination in self-assembly and mechanics of histidine-rich domains. *European Polymer Journal* **2018,** *109*, 229-236.

22. Liu, Y.; Pharr, M.; Salvatore, G. A., Lab-on-Skin: A Review of Flexible and Stretchable Electronics for Wearable Health Monitoring. *ACS Nano* **2017,** *11* (10), 9614-9635.

23. Chang, T.; Cao, X.; Dedon, L. R.; Long, S.; Huang, A.; Shao, Z.; Li, N.; Luo, H.; Jin, P., Optical design and stability study for ultrahigh-performance and long-lived vanadium dioxide-based thermochromic coatings. *Nano Energy* **2018,** *44*, 256-264.

24. Hu, B.; Ding, Y.; Chen, W.; Kulkarni, D.; Shen, Y.; Tsukruk, V. V.; Wang, Z. L., External-Strain Induced Insulating Phase Transition in VO2 Nanobeam and Its Application as Flexible Strain Sensor. *Advanced Materials* **2010,** *22* (45), 5134-5139.

25. Yamamoto, M.; Nouchi, R.; Kanki, T.; Hattori, A. N.; Watanabe, K.; Taniguchi, T.; Ueno, K.; Tanaka, H., Gate-Tunable Thermal Metal–Insulator Transition in VO2 Monolithically Integrated into a WSe2 Field-Effect Transistor. *ACS Applied Materials & Interfaces* **2019,** *11* (3), 3224-3230.

26. Kabir, S.; Yang, D.; Ahmad Kayani, A. B.; Zhang, H.; Nirantar, S.; Sriram, S.; Walia, S.; Bhaskaran, M., Solution-Processed VO2 Nanoparticle/Polymer Composite Films for Thermochromic Applications. *ACS Applied Nano Materials* **2022,** *5* (8), 10280-10291.

27. Chang, T.; Zhu, Y.; Cao, C.; Yang, C.; Luo, H.; Jin, P.; Cao, X., Multifunctional Flexible Vanadium Dioxide Films. *Accounts of Materials Research* **2021,** *2* (9), 714-725.

28. Zou, J.; Chen, X.; Xiao, L., Phase transition performance recovery of W-doped VO2 by annealing treatment. *Materials Research Express* **2018,** *5* (6), 065055.

29. Mesko, M.; Xiang, L.; Bohle, S.; Hwang, D. S.; Zeng, H.; Harrington, M. J., Catechol-Vanadium Binding Enhances Cross-Linking and Mechanics of a Mussel Byssus Coating Protein. *Chemistry of Materials* **2021,** *33* (16), 6530-6540.

30. Lin, Q.; Gourdon, D.; Sun, C.; Holten-Andersen, N.; Anderson, T. H.; Waite, J. H.; Israelachvili, J. N., Adhesion mechanisms of the mussel foot proteins mfp-1 and mfp-3. *Proceedings of the National Academy of Sciences* **2007,** *104* (10), 3782-3786.

31. Jehle, F.; Macías-Sánchez, E.; Sviben, S.; Fratzl, P.; Bertinetti, L.; Harrington, M. J., Hierarchically-structured metalloprotein composite coatings biofabricated from co-existing condensed liquid phases. *Nature Communications* **2020,** *11* (1), 862.

32. Li, Y.; Cheng, J.; Delparastan, P.; Wang, H.; Sigg, S. J.; DeFrates, K. G.; Cao, Y.; Messersmith, P. B., Molecular design principles of Lysine-DOPA wet adhesion. *Nature Communications* **2020,** *11* (1), 3895.

33. Maier, G. P.; Rapp, M. V.; Waite, J. H.; Israelachvili, J. N.; Butler, A., Adaptive synergy between catechol and lysine promotes wet adhesion by surface salt displacement. *Science* **2015,** *349* (6248), 628-632.

Chapter 7 : Conclusion

Nature offers remarkable examples of utilizing metal coordination to create high-performance materials that possess desirable properties surpassing those of manmade materials. Comprehending and emulating these strategies can serve as a pathway to develop advanced materials capable of addressing diverse challenges in materials science. This thesis showcased three examples where adopting metal chelation strategies utilized by the mussels lead to the creation of soft materials with unique properties. In the first study, we developed a pH-responsive injectable hydrogel scaffold, utilizing histidine-zinc coordination as an annealing strategy. Analogous to how preCol proteins self-assemble into tough fibers in seawater, peptide-functionalized microgels assemble into a mechanically robust and porous scaffold. Cytocompatibility studies on the scaffold showed no sign of cytotoxicity, suggesting its viability for potential minimally invasive tissue repair applications. In the second study, we engineered a self-healing nanoparticle-hydrogel composite that can be processed into an elastomeric thermochromic film. This was achieved through the strong yet reversible vanadium-catechol coordination bonds. Interestingly, hydrogels crosslinked with the VO_2 exhibit slower relaxation compared to those crosslinked with metal ions, attributed to the higher density of crosslinks. This straightforward approach preserves thermochromic qualities of VO_2, making it a practical choice for flexible, high-performance thermochromic materials for various applications, like smart windows, e-skin, and wearable devices. In the third study, we highlighted how the protein sequence significantly influences the metal chelation behavior of DOPA. In its natural sequence, DOPA demonstrates a heightened ability to establish robust bonds with both vanadium and iron

under low pH conditions, mirroring the acidic environment in metal storage particles found in mussel tissues. Capitalizing on the enhanced binding between catechol and iron under physiological conditions, we engineered an injectable granular system through the surface modification of microgels with mfp1 peptides. These modified microgels are capable of crosslinking into a porous self-healing scaffold in the presence of iron at physiological pH. This scaffold was shown to be biocompatible with cells, which highlights its exciting potential as an injectable platform for tissue engineering applications. These three studies serve as a testament to how bioinspiration can advance materials design and fabrication and emphasize that “there is plenty of room at the bottom” as famously stated by Richard Feynman to the then burgeoning field of nanoscience.